LIÈGE université
Ing. David Leleu

PEPs CHEMICAL ENGINEERING
Department of Chemical Engineering - Products, Environment, and Processes (PEPs)

Drop Behavior During Settling of Liquid-Liquid Dispersions for Equipment Design

David Leleu

Liège, June 2025

LIÈGE université
Ing. David Leleu

PEPs CHEMICAL ENGINEERING
Department of Chemical Engineering - Products, Environment, and Processes (PEPs)

Drop Behavior During Settling of Liquid-Liquid Dispersions for Equipment Design

David Leleu

Liège, June 2025

Members of the Jury

The jury for this thesis is composed of experts from both academia and industry, whose diverse backgrounds and extensive experience have greatly contributed to the quality and relevance of this work.

Prof. Dominique Toye, serving as President of the jury, is a full professor in the Department of Chemical Engineering at the University of Liège. She is renowned for her work in chemical reactor engineering, particularly in the application of advanced imaging techniques for process analysis.

Prof. Stoyan Gaydardzhiev, affiliated with the Faculty of Applied Science, Department ArGenCo at the University of Liège, brings a strong background in mineral processing, hydrometallurgy, and biohydrometallurgy.

Mr. Murat Kalem, representing the industrial sector, is currently working at Covestro in Germany. His participation ensures a valuable link between academic research and its practical applications in industry.

Prof. Andreas Jupke, from the Chair of Fluid Process Engineering at the Faculty of Mechanical Engineering at RWTH Aachen University, is an internationally recognized professor in the fields of separation technologies.

Prof. Andreas Pfennig, who serves both as the Secretary of the jury and the PhD supervisor, is affiliated with the Department of Chemical Engineering at the University of Liège. His guidance as thesis director has been central to the development of this work. With a strong expertise in separation processes, he has provided continuous academic support and played a key role in shaping the scientific direction and integrity of the research.

Abstract

Le but de la thèse est de fournir une compréhension approfondie du phénomène de séparation en batch de dispersions liquide-liquide, en développant et en validant un outil numérique basé sur le concept ReDrop (gouttes représentatives). La coalescence et la sédimentation doivent ainsi être décrites en détail. Un nouveau modèle de coalescence, pouvant être adapté à l'environnement des gouttes, a été développé. Le modèle de sédimentation, quant à lui, est étendu pour couvrir les faibles concentration en gouttes mais aussi les concentrations les plus élevées en y incluant la déformation des gouttes subissant la pression hydrostatique. Les différents modèles sont intégrés dans le programme ReDrop.

Le programme, et par conséquent les modèles, sont ensuite validés expérimentalement. Des expériences de sédimentation sont menées avec un équipement à l'échelle laboratoire qui a été conçu sur base de deux équipements décrits dans la littérature afin de fournir des résultats fiables et reproductibles. Les expériences de sédimentation sont réalisées avec un système diphasique iso-optique, où la coloration d'une phase permet des mesures continues et à haute résolution de la concentration des gouttes à tout moment et en tout point.

Les résultats des simulations ReDrop permettent de décrire les données expérimentales avec une bonne précision, validant ainsi les modèles et leurs hypothèses sous-jacentes. Les simulations ReDrop fournissent également des informations sur les phénomènes se produisant lors de la séparation des dispersions. Un temps de latence, souvent observé dans les systèmes techniques, est attribué à la présence initiale de très petites gouttes, qui ne commencent à sédimenter qu'après avoir atteint une taille critique, caractéristique du système et qui ne dépend que très peu de la distribution de taille initiale des gouttes et donc de l'intensité de l'agitation. Par ailleurs, une zone très compacte de gouttes, supposée s'étendre sur une grande hauteur, est rarement observée. À la place, une zone densément peuplée se forme, où les gouttes ne sont pas en contact permanent. Ces résultats mènent à une révision fondamentale de la vision classique de la séparation des dispersions liquide-liquide.

Pour aller plus loin dans la modélisation de la coalescence, l'effet des ions est étudié. Le potentiel électrostatique est mesuré par rapport à un système de référence, et son influence

sur le comportement de coalescence est évaluée. Cette étude constitue une première étape vers l'intégration de la théorie DLVO dans la modélisation de la coalescence entre gouttes.

Abstract

This thesis aims to provide a comprehensive understanding of batch settling in liquid–liquid dispersions by developing and validating a numerical tool based on the ReDrop (Representative Drops) concept. The coalescence and the sedimentation, thus, need to be described in detail. Particular attention is paid to coalescence, the principal challenge, through a new, adaptable model that accounts for droplet surroundings, from free settling to a close-packed environments. The sedimentation model is extended to cover the full range of holdup, including droplet deformation under hydrostatic pressure at high concentrations. The different models are included in the ReDrop program.

The program and, as a consequence, the models are then validated experimentally. Settling experiments are carried out in a laboratory-scale cell designed by comparing two equipment from the literature. This new cell consistently delivers robust and repeatable results. Settling experiments to validate the mathematical models are conducted with an iso-optical two-phase system, where dyeing one phase enables continuous, high-resolution holdup measurements at any point and any time.

The outcomes of the ReDrop simulations allow to describe the experimental data with good accuracy, thereby validating the models and their underlying hypotheses. The polydisperse ReDrop simulation also provide deeper insights into the detailed processes occurring during dispersion upon settling. A lag time, often observed in technical systems, is attributed to the presence of initially very small droplets that begin to settle only after reaching a certain size. This critical size is characteristic of the system and depends hardly on initial drop-size distribution. This leads to comparable slopes of the sedimentation curve independent of stirring intensity. Moreover, a widely assumed close-packed zone extending over a large height is rarely observed. Instead, a densely-packed zone forms, where drops are not in continuous contact. These findings lead to a fundamental revision of the underlying picture of settling

To further advance the coalescence modeling, the impact of ions is investigated. The electrostatic potential is measured relative to a reference system, and its influence on coalescence behaviour was evaluated. This study is a first step towards including DLVO theory in the modelling of coalescence between drops.

Ing. David Leleu

Drop Behavior During Settling of Liquid-Liquid Dispersions for Equipment Design

Dissertation

to obtain the academic degree of

Doctor

in

Chemical Engineering

submitted to

Université de Liège

supervisor:

Prof.-Dr.-Ing. Andreas Pfennig

Université de Liège

Liège, Juin 2025

DECLARATION SUR L'HONNEUR

Je déclare que j'ai rédigé cette thèse de manière indépendante, que je n'ai pas utilisé d'autres sources/ressources que celles qui ont été déclarées, et que j'ai indiqué explicitement tous les éléments qui ont été cités, soit littéralement, soit par leur contenu, dans les sources utilisées

Liège, …… ……

(date) (signature)

AFFIDAVIT

I declare that I have authored this thesis independently, that I have not used other than the declared sources/resources, and that I have explicitly indicated all material which has been quoted either literally or by content from the used sources.

Liège, …… ……

(date) (signature)

Preface

First and foremost, I would like to express my deepest gratitude to my thesis supervisor, Professor Andreas Pfennig. His guidance, support, and encouragement have been crucial during this journey. I appreciate everything he taught me, his drive, and the many opportunities he gave me to participate in academic conferences

I would also like to thank the members of my thesis committee, Professor Dominique Toye, Professor Stoyan Gaydardzhiev and Murat Kalem, for their constructive feedback and insightful discussions. The direction of this research was refocused and refined with their input during our various meetings.

I would like to express my sincere thanks to Andreas Jupke, an external member of the thesis jury, for agreeing to evaluate the work presented in this dissertation. His time and expertise are highly valued.

This research would not have been possible without the financial support provided by the funding organizations involved, which are the FNRS, the EU-funded Phoenix project, and the German Federal Ministry for Economic Affairs and Energy. Their contributions made it possible for me to fully engage with the topic of this thesis.

I want to express my deep appreciation to the Chemical Engineering Department members for their presence and support, and especially to Thierry Salmon and Nicolas Graindorge for their constant assistance and patience. Their willingness to listen to my thoughts and questions about models and simulations has been a great help and motivation.

Lastly, I want to thank my family for being a source of strength and balance. I am especially grateful to my wife, Azury Diaz De La Barrera, for her support and motivation throughout the entire project. Her encouragement and belief in me have made all the difference.

Once again, I would like to thank everyone who has contributed to the success of this work. I hope that this thesis will make a significant contribution in the understanding the phenomena occurring during the settling of liquid-liquid dispersions. Yours sincerely".

Table of Content

1 Introduction

Liquid-liquid dispersions are systems formed by e.g. mixing two immiscible liquid phases. In such systems, one phase is dispersed as droplets in the other, which serves as the continuous phase. These dispersions are widely used in chemical processes, such as in solvent extraction, where the objective is to transfer a target component from one liquid phase to another. After the extraction step, the resulting dispersion is typically allowed to settle, separating into enriched and depleted phases. These phases can then be collected and further processed, depending on the specific requirements of the chemical process.

Industrial-scale decanters can be used to separate and collect the two clear liquid phases from a liquid-liquid dispersion. During liquid-liquid dispersion separation, two main phenomena act on the droplets: sedimentation and coalescence. Sedimentation is induced by the gravity caused by the difference in density between the two phases. Coalescence is the phenomenon that causes two drops in contact to merge. These two phenomena cause the droplets to sediment, come into contact with each other and grow larger and larger over time, resulting, after some time, in two completely separated phases. This settling time, which is the time required for the system to separate into two distinct phases, must be known and modeled for the dispersion under study in order to properly design industrial decanters.

There are several approaches to the design of decanters for liquid-liquid dispersions. One method is to design the settler based on the evaluation of the residence time of the liquid-liquid dispersion, e.g. based on Stokes' law or an empirical model [80, 81]. A second method focuses on controlling the overflow velocity of the continuous phase by setting a critical discharge rate that prevents re-entrainment of the dispersed phase and maintains a stable interface for separation [82, 83]. However, trace components, such as ions, can significantly influence coalescence, and their effects vary depending on their type and concentration [2]. This complexity poses a significant challenge in predicting settling behavior, thereby compromising the accuracy of these methods due to the omission of coalescence evaluation.

A third method consists to perform settling experiment to accurately assess coalescence and support the proper design of decanters [5, 29].

These settling experiments are usually performed at the laboratory scale, using a device known as a settling cell, which is designed to observe and characterize the coalescence behavior of liquid-liquid dispersions during settling [15]. Over the years, various settling cells have been developed for this purpose, in which dispersion is produced by stirring or shaking [5, 29].

The settling of the dispersion over time in a settling cell is shown schematically in Fig. 1-1, which is the picture given in the literature to date. Initially, the drops are homogenously dispersed in the continuous phase. Over time, the droplets of the dispersed phase sediment and form a sedimentation front below which no droplets are present. The evolution of this sedimentation front over time is characterized by the sedimentation curve. After some time, the droplets are also coalescing and form a clear phase establishing the main interface of the system. The evolution of this main interface over time is characterized by the coalescence curve. Between the sedimentation and the coalescence curves are the remaining drops that have not yet reached the main interface or coalesced with the main interface. These remaining droplets can either move freely, constituting the free sedimentation zone, or be in close contact, forming the close-packed zone. The coalescence and the sedimentation curves meet at a certain time when the system is completely separated, which is leading to the settling time of the system.

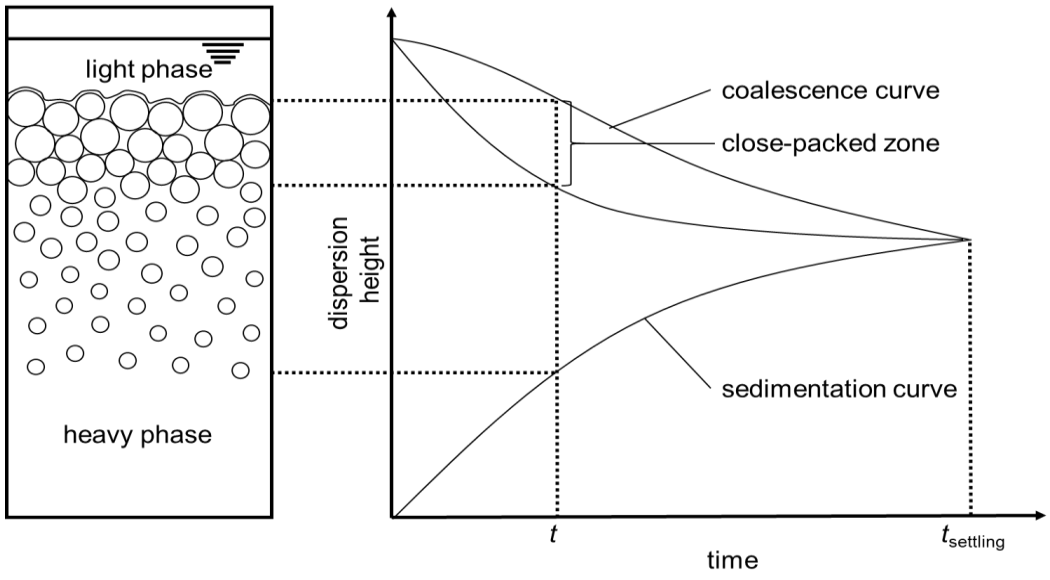

Fig. 1-1: evolution of the settling of a liquid-liquid dispersion after Henschke [16]

In order to validate the coalescence model developed in the thesis for the settling of liquid-liquid dispersions, a simulation tool has been developed to predict the settling of liquid-liquid

dispersions. The numerical tool is based on the ReDrop concept (Representative Drops) [1]. Sedimentation and coalescence are evaluated for a sufficiently large ensemble of representative individual drops at each time step. Both elementary processes are depicted by suitable models. The ReDrop concept is explained in details in chapter 2. As with the other chapters, the literature review is detailed in that chapter.

The ReDrop program integrates different models which each describe a phenomenon experienced by the drops. The following chapters, 3 to 5, focus on each phenomenon individually namely sedimentation and coalescence.

The results obtained from the ReDrop program are then compared with experimental data in order to validate the general approach and the coalescence model developed in this thesis. Chapter 6 describes the equipment used and Chapter 7 describes the experimental setup in detail. The model validation is described in chapter 8.

In chapter, 9, finally the effect of ions on the coalescence behavior of droplets is investigated.

2 Modeling Concept for Simulation of Settling of Liquid-Liquid Dispersions

A variety of methods are available to describe the settling of liquid-liquid dispersions, each balancing physical accuracy with computational efficiency. The simplest approach consists to evaluate the averaged dispersion–disintegration velocity, v_{dd}, based on the initial dispersion volume, V_{disp}, and settling time, t_s, in a cell of area A_{cell}:

$$v_{dd} = \frac{V_{disp}}{t_s A_{cell}} \quad . \tag{2-1}$$

The averaged dispersion–disintegration velocity can then be used to design a settler [92, 93]. However, this averaged velocity fails if the dispersed-phase holdup changes, since varying holdup changes the relative importance of sedimentation and coalescence during the settling. For instance, when coalescence at the interface is instantaneous but negligible in bulk, the sedimentation path will vary with the phase ratio. To bound this behavior, two limiting-case models are used: first, when droplets are sufficiently large and interfacial tension moderate, sedimentation model applied to a single characteristic drop diameter predicts settling velocities, and coalescence is ignored. Conversely, typically in system of fine droplets, coalescence model is applied while neglecting gravitational sedimentation. Although this framework enables quick estimates of settling time, it can deviate from pilot-plant data whenever sedimentation and coalescence both are relevant.

To introduce minimal size-distribution realism without excessive computational cost, authors proposed a height-resolved, mean-diameter model [15, 61, 86, 91]. In this framework, Henschke [15] developed a method where every droplet shares the same initial diameter and therefore settles at a uniform terminal velocity. Coalescence is only allowed within a close-packed zone, and even there, all coalescing droplets are assumed to remain monodisperse at each height. This simplification yields analytically tractable holdup profiles that require limited number of parameters: the initial droplet diameter, the fluid properties, and a single coalescence parameter. Its drawbacks include an inability to capture the development of polydispersity, a failure to predict the lag time often observed before coalescence begins in technical systems, and a neglect of counter-currents that can carry smaller droplets in the opposite direction to larger ones, which can lead to some deviations in the settling prediction.

Finally, this approach does not allow to determine the fraction of small drops remaining in the continuous phase after settling, which is variable very relevant in technical applications.

A more detailed alternative integrates computational fluid dynamics (CFD) with population balance equations (PBEs) to resolve both macroscopic flow patterns and droplet-size dynamics [84, 85, 88-90]. PBEs are integro-differential equations that describe how the local drop-size distribution evolves in space and time, accounting for processes such as coalescence. In CFD–PBE frameworks, the velocity and turbulence fields are first calculated by solving the Navier–Stokes equations. These local flow properties then feed into the PBE kernels that govern droplet coalescence. This multi-scale approach can reproduce complex features such as dead zones, vortices, separation fronts, and the evolution of the drop-size distribution. However, it is mesh-sensitive and prone to convergence difficulties, and the coupled software environments often require days or even weeks of computation on high-performance clusters. As a result, CFD–PBE remains primarily a research tool and is rarely used for routine industrial design.

An elegant compromise between oversimplified correlations and computationally prohibitive multi-scale models is offered by the Representative Drops (ReDrop) algorithm. ReDrop tracks an ensemble of “representative” droplets to predict how an entire dispersion settles and coalesces over time [1, 2, 3]. By following only these few drops, ReDrop captures drops inter-action physics keeping runtimes relatively fast. This balance of droplet-scale accuracy and low computational cost makes ReDrop a practical choice where both fidelity and speed matter.

In summary, dominant-phenomenon correlations are invaluable for quick feasibility screens; Henschke’s mean-diameter approach provides rapid insights when droplet spectra are narrow; CFD–PBE offers the most detailed mechanistic view but at prohibitive cost and complexity. By contrast, ReDrop offers a good balance between accuracy and efficiency, capturing multi-scale physics including sedimentation and coalescence with manageable runtimes and minimal experimental trials, making it the preferred method for simulating the settling of liquid–liquid dispersions.

2.1 ReDrop Concept

The ReDrop approach simulates settling by tracking just a handful of “representative drops” inside a characteristic slice of the full dispersion, i.e. a vertical section of cross-sectional area A_{repr}. Each representative drop carries the same diameter, position, and velocity that an ensemble of real droplets would have, and together they reproduce the overall dispersed-phase holdup in the system. Rather than resolving every droplet or coupling to a full CFD mesh, ReDrop applies sedimentation and coalescence model to these representative drops to predict the time-evolution of mean drop size, holdup, pressure drop, and other key variables. The characteristic slice is further divided into height layers, within which local quantities, such as Sauter mean diameter, continuous-phase flow rate, hydrostatic pressure, or the holdup, are updated at each time step [1, 2, 3].

The variables influencing the drops behavior, and integrated in the ReDrop simulation tool, are discussed in details in chapters 3, 4 and 5.

2.2 ReDrop Algorithm

The ReDrop algorithm is summarized in Fig. 2-1. The ReDrop algorithm begins by reading user-provided input files specifying system properties, e.g. densities, viscosities and interfacial tension, initial dispersed-phase holdup, drop-size distribution parameters, time step etc. At the start of the simulation, a small set of “Representative Drops” is created, each drop has the same initial diameter and is randomly placed within the slice’s height.

The slice is divided into horizontal layers, and the local holdup is computed from the current drop positions and sizes. A mass balance in each layer yields the required continuous-phase upward flow profile, which is then linearly interpolated between layers. Using sedimentation models, vertical sedimentation velocity of each drop relative to the continuous phase is calculated, and its absolute vertical velocity updates its height. Sedimentation models are discussed in chapter 4.

The algorithm continuously monitors local holdup to distinguish between the free-sedimentation zone and the close-packed zone. Drops in the close-packed zone are assumed to remain in contact, regardless of any bulk motion of that zone induced by interface rise, significantly affecting their coalescence behavior.

The coalescence evaluation loops over every pair of ReDrops whose centers lie within their average diameter vertically and computes a collision probability based on their relative sedimentation velocity and the local holdup. Since horizontal positions are not tracked, e.g. drops are assumed uniformly mixed, special care has to be taken to properly evaluate the contact probability of two drops as a basis to quantify correctly the probability of a coalescence event. An identical procedure applies for coalescence with the interface. All drops in the nearest vicinity of the interface are considered the cross-sectional area of which add up to the local holdup at the interface multiplied with A_{repr}. Finally, each potential collision is tested against a random number to decide if coalescence occurs, yielding a stochastic but statistically accurate representation of coalescence [1]. Coalescence model is explained in chapters 3 and 5.

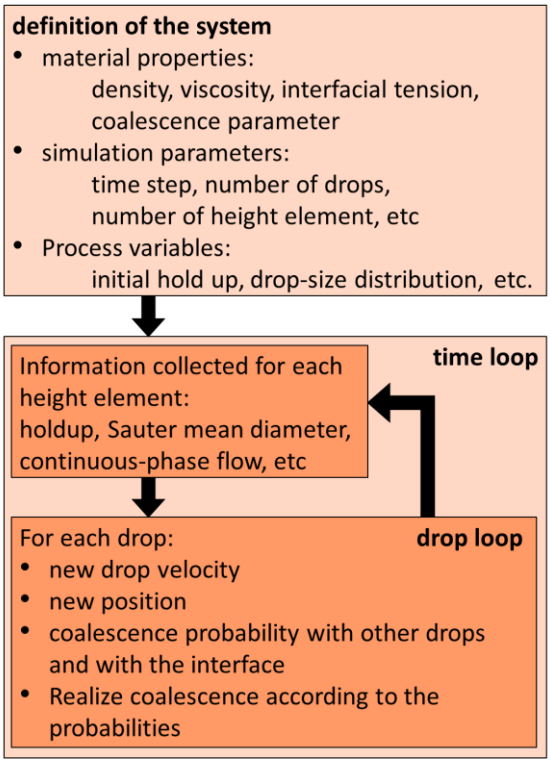

Fig. 2-1: ReDrop algorithm to simulate the batch-settling of liquid-liquid dispersion

After coalescence checks, the simulation advances by one time step and repeats the loop. At each step, the ReDrop program records the major interface height, drop positions and sizes, and derives macroscopic sedimentation and coalescence curves and the limit between close-packed and free-sedimentation zone, directly from the tracked drops.

In the following chapters, the different models used to simulate the settling of liquid-liquid dispersion, are developed in details.

3 Coalescence Model

A variety of models have been proposed to describe coalescence, for which recent comprehensive reviews are available [2, 7, 8, 9]. Coalescence is a stochastic event that can be quantified by a probability, $p_{\text{coalescence}}$, which describes the probability that two drops will coalesce per contact between drops. Different modelling approaches have been proposed to characterize $p_{\text{coalescence}}$: the energy model, the critical velocity model, and the film-drainage model. All models assume that the main coalescence event occurs during the collision.

In the energy model, it is assumed that the kinetic energy of the drops, E_K, must overcome an energy barrier characterized by the surface tension, E_σ, [10, 11], resulting in an overall description similar to a Boltzmann probability:

$$p_{\text{coalescence}} \propto \exp(-\frac{E_\sigma}{E_K}) \quad . \tag{3-1}$$

This approach has been proposed to describe the drops coalescence for turbulent systems such as a stirred tank. According to the energy model, coalescence is enhanced by a high collision energy.

In the critical-velocity model, the relative velocity of the drops, v_{relative}, is compared to a critical velocity, v_{critical}, independent of the drop diameter, above which coalescence is assumed not to occur [7, 12]:

$$p_{\text{coalescence}} = \max(\frac{v_{\text{critical}}}{v_{\text{relative}}}, 1) \quad . \tag{3-2}$$

This model is based on experiments performed on bubble coalescence in turbulent flow [12]. In contrast to the energy model, coalescence is enhanced at low collision velocities because the drops remain in contact for longer.

A third approach assumes that a film forms between two approaching drops that meet. The drainage of the film determines the probability of coalescence. In this case, if the drops remain in contact long enough, the film thickness has time to decrease below a critical limit, i.e. the critical film thickness, and thus to induce the film rupture and the coalescence of the drops [7, 9, 13, 14, 15]. Two time scales are compared to evaluate the probability of coalescence, the

coalescence time, $t_{coalescence}$, which refers to a characteristic that is a measure of the time required for the drops to approach until the thin film to break, and the contact time, $t_{contact}$, which describes how long the drops remain in contact under the specific fluid-dynamic conditions of the equipment being considered. Coulaloglou and Tavlarides [14] expressed the probability of coalescence once the drops are in contact with:

$$p_{coalescence} \propto \exp(-\frac{t_{coalescence}}{t_{contact}}) \quad . \tag{3-3}$$

To investigate, which model is better suited to describe coalescence, Kamp performed collision experiments between a fixed drop and a sedimenting drop and found that at high relative velocities the coalescence probability is close to zero [8]. This cannot be described by the energy model in principle, which is therefore not applicable to liquid dispersions. On the other hand, Henschke has shown that detailed modelling of phase separation is possible, when coalescence is modelled with the drainage model, which does not depend solely on the relative drop velocity [5, 15, 16]. This suggests that the drainage model is a good starting point for detailed investigation. This is supported by a number of studies showing the influence of film drainage on coalescence [7, 9, 13, 14, 15] and demonstrating a good correlation between experimental results and the film-drainage model [2, 15]. Therefore, the film-drainage model is chosen as the basis for further investigation of the coalescence in this study.

3.1 Coalescence Model Adapted for Technical Equipment

Coalescence models have been described in detail by Kopriwa [5, 27]. In order to model coalescence in a simulation, it is necessary to quantitatively describe the coalescence frequency, $f_{coalescence}$, for a drop or a drop class, which represents the number of coalescence events per unit time between two drops. To characterize $f_{coalescence}$, the individual steps that occur during the coalescence event must be considered, as shown schematically in Fig. 3-1. The figure is an extention of the diagram proposed by Kopriwa [5], where it is also indicated on which influences the individual contributions depend, which was also proven by Kopriwa. In order for two drops to coalesce, they must first collide. The collision between two representative drops can be characterized by a frequency, $f_{collision}$, which indicates how often these drops meet per unit of time.

Once the drops collide, they can either bounce off each other or remain in contact, which is characterized by the probability of bouncing, p_{bouncing}. It is assumed that coalescence can only take place if the drops remain in contact long enough, and thus do not bounce. The coalescence probability, $p_{\text{coalescence}}$, in the considered film-drainage model depends on the time the drops remain in contact, i.e. the contact time, and on the time it takes the drop to coalesce, i.e. the coalescence time.

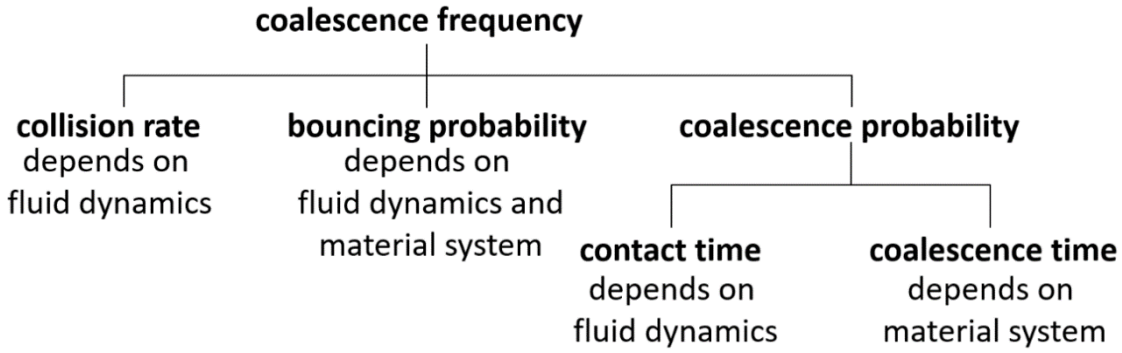

Fig. 3-1: Schematic representation of steps in the coalescence process.

The coalescence frequency can thus be described as the product of the collision frequency, the non-bouncing probability and the coalescence probability:

$$f_{\text{coalescence}} = f_{\text{collision}}(1 - p_{\text{bouncing}})p_{\text{coalescence}} \quad , \tag{3-4}$$

which is the general equation for the coalescence frequency.

As shown by Kopriwa [27] (cf. Fig. 3-1), the collision frequency and contact time depend on the fluid-dynamics surrounding the drops and therefore on the type of equipment. For example, turbulence is more pronounced in extraction columns than in continuous settlers, which affects the corresponding terms. The coalescence time, on the other hand, depends solely on the material properties and the details of the interfacial interactions, including the effects of trace components [27].

The different variables that affect the frequency of coalescence are detailed in the following sections.

3.2 Collision Frequency

Different phenomena induce drop collisions in liquid-liquid dispersions, depending on the type of equipment [7]. First, there must be an opportunity for the drops to meet geometrically. If the drops experience essentially random motion, e.g. induced by turbulence in extraction columns, the collision frequency, $f_{\text{turbulence}}$, can be described by analogy with kinetic gas theory, assuming that the drops behave like spheres [17]:

$$f_{\text{turbulence}} = C_{\text{coll,turbulence}} (d_1 + d_2)^2 \Psi^{1/3} \sqrt{d_1^{2/3} + d_2^{2/3}} \frac{1}{(1+\varepsilon)} \quad , \tag{3-5}$$

where d_i is the diameter of each drop and Ψ is the energy dissipation, which must be properly described for each type of extraction column. $C_{\text{coll,turbulence}}$ is a parameter characterizing the fluid-dynamics of a specific column type. This equation also takes into account the dependence of the geometric probability of two drops meeting on the hold-up, ε .

In contrast, in continuous settlers, the droplets move mainly due to vertical sedimentation induced by their buoyancy, leading to drop collision [13, 18]. In large settlers, large-scale flow structures may also occur [29]. Droplet velocities are of the order of the total flow velocity of the phases, typically around 1 cm/s and equipment dimensions are large as compared to the drops diameter. The effect of large-scale flow structures, such as circulation loops or dead zone, on the relative motion of the droplets on the mm scale is thus negligible. It is assumed here that these large-scale flow structure do not contribute to the droplet approach velocity. In addition, Brownian motion can in principle introduce a random contribution to the trajectories of the drops, which is negligible for drops larger than 10 µm in diameter [19]. Since typical drop diameters in an initial dispersion in industrial settlers are above 50 µm, Brownian motion can also be neglected.

Thus, for batch settlers, the motion of the drops is assumed to be essentially vertical. To describe the collision frequency of vertically moving drops, two freely sedimenting drops can be considered as shown in Fig. 3-2. The drops move in the representative volume of the settler with a bottom area of A_{cell}. The vertical positions of the drops are *h*. The drops shown can collide if their centers lie within the collision cylinder indicated, giving a geometric probability of the drops colliding:

$$p_{\text{coll,average}} \propto \frac{\pi(d_1 + d_2)^2}{4A_{\text{cell}}} \quad . \tag{3-6}$$

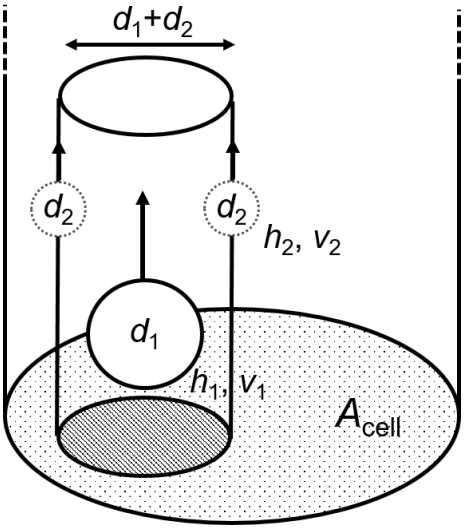

Fig. 3-2: Schematic representation of the collision diameter between two drops in a batch settling experiment.

Eq. 3-6 corresponds to the case where the averaged collision probability between two drops along their entire sedimentation path is considered. If the vertical position of the drops is accessible in the modelling, e.g. when a time-resolved simulation is realized, the collision probability also depends on the height difference between the drops at a given point in time, as shown in Fig. 3-3. The collision probability is derived from the Pythagorean theorem, detailed in appendix 11.1, which leads to:

$$p_{\text{coll,intantanenous}} = \frac{\pi\left((d_1 + d_2)^2 - 4\left(h_1 - h_2\right)^2\right)}{4A_{\text{cell}}} \quad . \tag{3-7}$$

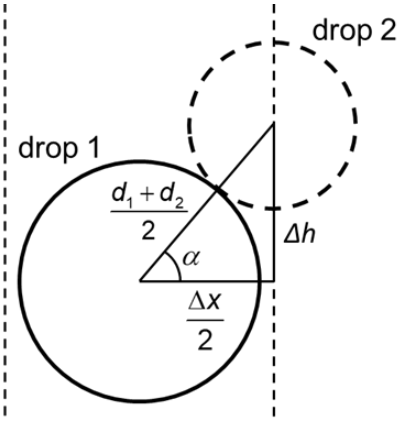

Fig. 3-3: Cross-section of two drops colliding

In the case of simulations where an average probability is necessary, i.e. if height of the drops is not known exactly, Eq. 3-6 should be used. However, Eq. 3-6 shows a proportional relationship that must be precisely evaluated to quantitatively determine the proportionality factor. In order to determine the proportionality factor, Eq. 3-7 can be averaged over the possible contact geometries, ranging from drops meeting along their central axis to two drops just touching in passing. The resulting overall collision probability is then obtained by integration of Eq. 3-7. The full derivation is available in appendix 11.1. The averaged collision probability results in:

$$p_{\text{coll,average}} = \frac{\pi(d_1 + d_2)^2}{6A_{\text{cell}}} \quad . \tag{3-8}$$

These considerations show that the geometric probabilities of two drops hitting each other depend on the specifics of how the equipment and drops are represented in the simulation.

The collision probability must also take into account whether the drops are considered individually or as a class in a drop-size distribution and must be adjusted accordingly. For example, if drop classes are considered, the local hold-up must be included in the definition of the collision probability, since the probability of a drop of one class hitting a drop of another class also depends on the product of the hold-up of both drop-size classes. This is not necessary here, where each individual drop is considered within A_{cell}.

The geometric probability must then be corrected for the so-called free-volume effect, which expresses that in the vicinity of a drop the free volume is reduced, which tends to increase the probability for collision [2]. Assuming that the drops behave like an ensemble of spheres, this effect can be quantified using the radial distribution function at contact. While this effect has already been considered for monodispersed drop-size distributions [2, 7], polydispersity is the typical case in engineering systems [10, 20]. Therefore, the hard-sphere model of Boublik [21] and Mansoori, Carnahan, Starling and Leland [22] was considered here:

$$\gamma = 1 + C_{\text{BMCSL}} \left(\frac{1}{1-\varepsilon} + \frac{3\xi d_1 d_2}{(1-\varepsilon)^2 (d_1 + d_2)} + \frac{2\xi^2 d_1^2 d_2^2}{(1-\varepsilon)^3 (d_1 + d_2)^2} - 1 \right) \quad , \tag{3-9}$$

with

$$\xi = \sum_i \frac{\pi x_i d_i^2}{6V_{\text{drop}}} \quad , \tag{3-10}$$

where x_i is the number fraction of drops of diameter d_i. Here, C_{BMCSL} is an adjustable parameter that scales this factor. While it has been shown that for extraction columns the full effect must be taken into account, i.e. $C_{\mathrm{BMCSL}} = 1$ [27], for settlers a reduced influence is expected, since a random influence on the drop motion is not predominant and is only slightly induced by the drop swarm which affects the sedimentation of individual drops.

In ReDrop simulation, since representative drops height is known exactly at each time step, collision frequency for drops moving by buoyancy, f_{buoyancy}, is thus:

$$f_{\mathrm{buoyancy}} = C_{\mathrm{coll,buoyancy}} \gamma p_{\mathrm{coll,instantaneous}} \quad . \tag{3-11}$$

The adjustable parameter $C_{\mathrm{coll,buoyancy}}$ collects all the geometric and other proportionality factors mentioned above.

Finally, in the general case, buoyancy and turbulence both contribute to the total collision frequency [1]:

$$f_{\mathrm{collision}} = f_{\mathrm{buoyancy}} + f_{\mathrm{turbulence}} \quad . \tag{3-12}$$

On the other hand, drops in a close-packed layer or at the interface are always in contact. In these cases, only geometric considerations need to be taken into account to characterize the probability of drops of a given diameter being in contact. All other contributions are equal, leading to:

$$C_{\mathrm{coll,buoyancy}} = 1 \quad . \tag{3-13}$$

The total collision frequency for drops in the close-packed zone is thus:

$$f_{\mathrm{collision}} = p_{\mathrm{coll,instantaneous}} \quad . \tag{3-14}$$

3.3 Bouncing Probability

After two drops have collided, their bouncing probability must be taken into account. The experimental data of Kamp [8], who analyzed the interaction of a drop hanging at the tip of a capillary in the continuous phase, which is hit by a drop produced by a syringe at a different relative position with respect to the first drop, are shown in Fig. 3-4. These data and the study of bubble coalescence by Lehr and Mewes [12] show that at high relative velocities the probability of coalescence is close to zero. Thus, if the relative velocities of the drops exceed a

critical value, the drops are likely to bounce when they meet. If their relative velocity is low, the drops remain in contact, following their mutual curvature, and during this time the coalescence process can take place.

Their experimental data suggest that the bouncing probability can be approximated by a step function:

$$p_{\text{bouncing}} = \begin{cases} 1 \text{ if } v_{\text{relative}} \geq v_{\text{critical}} \\ 0 \text{ otherwise} \end{cases} \quad . \tag{3-15}$$

The critical velocity is calculated here under the conditions of the Kamp experiment, e.g. one fixed and one moving drop. The critical velocity in this particular configuration, which characterizes the step function, results from the balance of forces acting on the drops:

$$F_{\text{inertial}} = F_{\text{buoyancy}} + F_{\text{drag}} + F_{\text{Young-Laplace}} \quad . \tag{3-16}$$

As derived in the Appendix 11.2, the equation is solved numerically to give:

$$v_{\text{critical,experiment}} \approx 0.014 \left(\frac{\Delta\rho g d^6 \mu^3}{\sigma^4} \right)^{0.2} \quad . \tag{3-17}$$

as an empirical relationship for the critical velocity fitted to the experimental data of Kamp. Eq. 3-17 is a first step to evaluate the critical velocity between two moving drops, but would need further experimental validation.

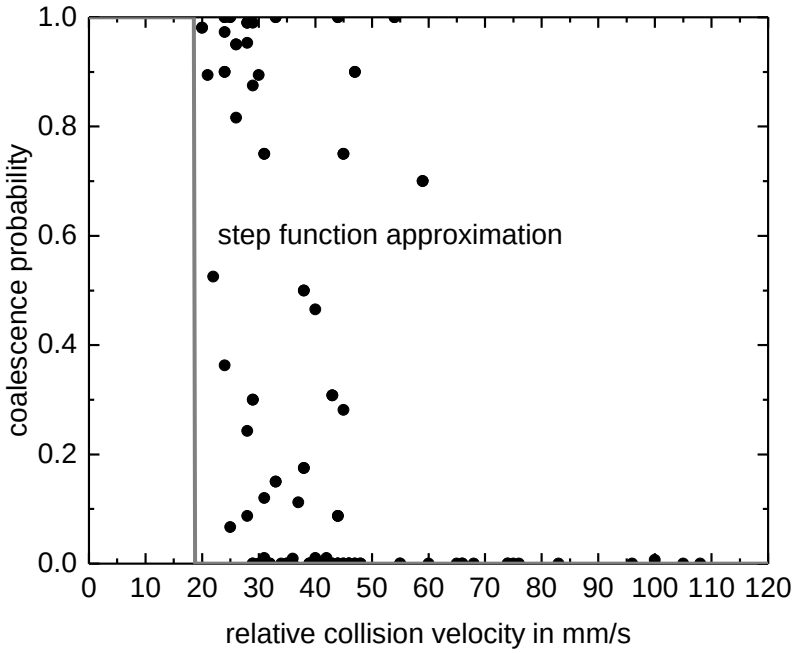

Fig. 3-4: Data from Kamp [8] showing the influence of the collision velocity on the coalescence probability.

In a gravity settler, due to the small size of the droplets and their resulting small velocity difference between sedimenting droplets, the critical velocity leading to rebound is hardly reached. This phenomenon is particularly pronounced at high holdup, where the droplets exhibit an even lower sedimentation velocity and are consequently further from the critical value. It can be thus assumed that the collision velocities of drops in batch-settling of liquid-liquid dispersions are low enough to neglect the bouncing probability:

$$p_{\text{bouncing}} = 0 \quad . \tag{3-18}$$

The coalescence frequency can now be simplified for the case of batch-settling of liquid-liquid dispersions [2, 8].

$$f_{\text{coalescence}} = f_{\text{collision}} p_{\text{coalescence}} \quad . \tag{3-19}$$

For extraction columns, however, this variable must be taken into account, as local velocities and shear rates of the continuous phase, including turbulence, can be significant [2], as for example in stirred columns [23].

3.4 Coalescence Probability

If the drops remain in contact after the collision, the next step to be characterized is the probability of coalescence. As concluded in chapter 3.1, the coalescence probability between two representative drops is best expressed by the film-drainage model. Typically, the contact time is related to the coalescence time by a Boltzmann-like probability function. The equation most commonly used to describe coalescence probability in extraction equipment is the model of Coulaloglou and Tavlarides [14], already introduced as Eq. 3-3.

To understand how the coalescence time and the contact time are related in the expression of the coalescence probability, the coalescence phenomenon can be represented in more detail. Conceptually, the total contact time t_{contact} can be divided into n time steps, Δt, as shown in Fig. 3-5.

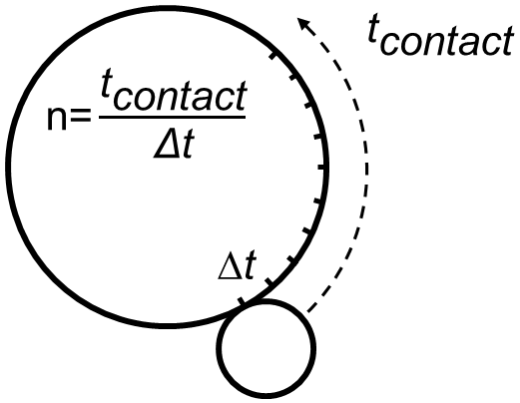

Fig. 3-5 : Conceptual visualization of the division of contact time into time steps

For each time step, the probability of non-coalescence can then be characterized as $p_{\text{non-coalescence},\Delta t}$ Assuming that the coalescence probability and thus the coalescence time, are independent of the specific Δt regarded, for $n\Delta t$ the following must hold:

$$p_{\text{non-coalescence},n\Delta t} = \left(p_{\text{non-coalescence},\Delta t}\right)^n \quad . \tag{3-20}$$

Only an exponential function fulfils this boundary condition, which requires the total non-coalescence probability to be written as:

$$p_{\text{non-coalescence}} = \exp\left(-\sum_i^n \frac{\Delta t}{t_{\text{coalescence}}}\right) \quad , \tag{3-21}$$

where, $t_{\text{coalescence}}$ is assumed to be identical for all the time step and equal to the overall coalescence time. This leads to:

$$p_{\text{non-coalescence}} = \exp\left(-\frac{1}{t_{\text{coalescence}}} \sum_{i}^{n} \Delta t \right) \quad , \tag{3-22}$$

from which the coalescence probability results:

$$p_{coalescence} = 1 - \exp\left(-\frac{t_{contact}}{t_{coalescence}} \right) \quad . \tag{3-23}$$

Eq. 3-23 differs significantly from various film drainage models [24, 25, 26] and in particular from the equation of Coulaloglou and Tavlarides, Eq. 3-3 [14]. The new expression, Eq. 3-23, is particularly consistent in simulations where time is divided into time steps, giving consistent results. If instead the expression of Coulaloglou and Tavlarides, Eq. 3-3, is used in a time-resolving simulation, then the probability of droplet survival behaves in fact as Eq. 3-20 and, as a consequence, the time step chosen will have an influence on the result. This leads to a different result also if the integral collision is considered via t_{contact}. Therefore, a consistent description can only be achieved with Eq. 3-23 regardless of whether the total collision is considered or whether it is divided into time steps. This consistent evaluation even allows to vary the time step during simulation, which is e.g. relevant if very long settling processes induced by very fine dispersions are to be described.

3.4.1 Contact Time

A model used by several authors [2, 8, 14] to describe the total contact time between two droplets depends on the droplet diameters and the isotropic Kolmogorov turbulence accounted for by the energy dissipation, Ψ:

$$t_{contact} = \frac{(d_1 + d_2)^{2/3}}{\Psi^{1/3}} \quad . \tag{3-24}$$

Eq. 3-24 is adapted for systems where the droplets are subjected to turbulence, such as in an extraction column. The energy dissipation has to be evaluated appropriately for each type of column [27].

The energy dissipation can also be related to the relative velocity of the drops by [8, 14]:

$$v_{relative} = \sqrt{2}\left(\Psi\left(d_1 + d_2\right)\right)^{1/3} \quad , \tag{3-25}$$

which, when combined with Eq. 3-24 gives:

$$t_{\text{contact}} = \sqrt{2}\frac{d_1 + d_2}{v_{\text{relative}}} \quad . \tag{3-26}$$

Eq. 3-26 is adapted for droplets in settlers, where the contact time is directly related to the relative velocity of the droplets instead of the energy dissipation, which is not a common variable for settlers.

The contact time given by Eq. 3-26 is proportional to the time taken for the drops to travel a distance equal to their average diameter. As described in appendix 11.3, simulation of the relative motion of the drops, e.g. drops moving vertically in a gravity settler, validates the proportionality given by Eq. 3-26. However, the proportionality factor in front of Eq. 3-26, initially equal to $\sqrt{2}$, should be chosen as follows:

$$t_{\text{contact}} = 1.52\frac{d_1 + d_2}{v_{\text{relative}}} \quad . \tag{3-27}$$

3.4.2 Coalescence Time

When two drops are close enough, they can coalesce under the effect of the driving force, F_{driving} , that pushes them towards each other. Under the effect of this driving force, the film of continuous phase forming between the drops decreases in thickness with time, the driving force thus squeezes out the film. The fluid dynamic force, $F_{\text{fluid-dynamic}}$, induced by this flow of continuous phase, is balanced by the driving force acting between the drops. The coalescence time is the time required to reduce this film thickness until a critical value is reached, below which the attractive van der Waals forces become sufficiently large to induce coalescence between the two drops.

When modelling this process, drop deformation and interfacial mobility must be taken into account [5, 27, 7].

The mobility of the interface influences the flow of the continuous phase between two approaching drops and thus the time required for the film to be squeezed out, as shown in Fig. 3-6.The mobility of the interface may be hindered by the presence of surfactants or by the high

viscosity of the dispersed phase [2, 9]. For other situations, e.g. dispersions prepared with pure solvents or a sufficiently low viscosity of the dispersed phase, the interface can be assumed to be partially or fully mobile, the corresponding expressions have been collected by Kopriwa [27]. A fully mobile interface will induce a faster flow of the continuous phase and thus a shorter coalescence time compared to immobile or partially mobile interfaces. However, in technical systems the interface can be assumed to be immobile in a typical case due to the impurities usually present.

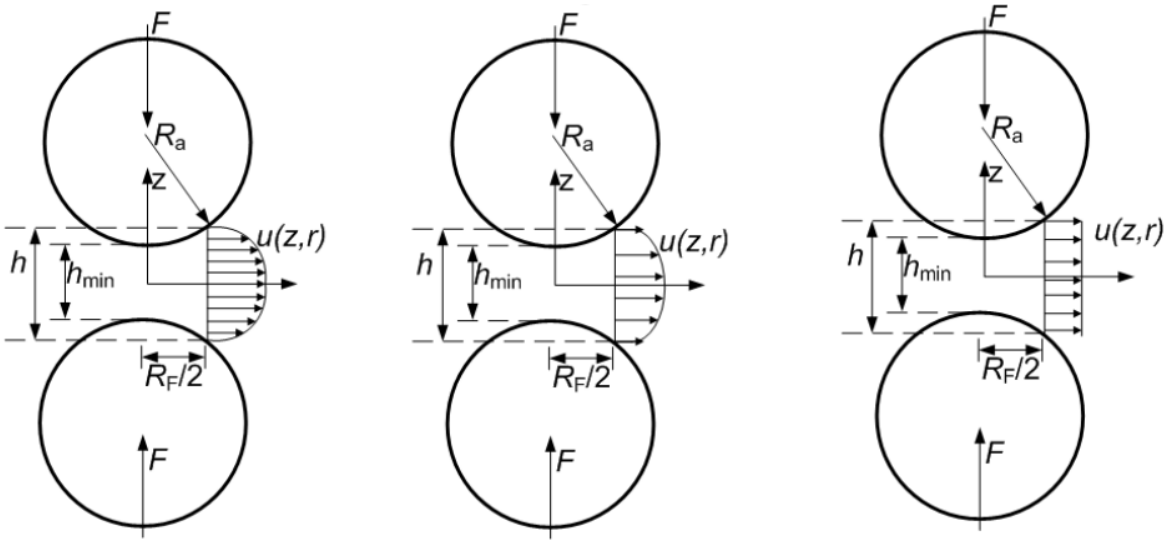

Fig. 3-6: Velocity profile of the continuous phase between two approaching drops for an immobile (left), partially mobile (centre) and fully mobile (right) interface [27].

Regarding the deformation of the droplets, in the simplest case it can be assumed that the droplets remain rigid during film drainage leading to the rigid sphere model (cf. case b in Fig. 3-7). Liao and Lucas [7] argued that this approach is only reasonable for small drops, below 1 mm. Below this diameter, the Young-Laplace pressure is strong enough to maintain the spherical shape of the drops. This approach is therefore not compatible with batch settling experiments, where larger drops are often present. The deformation of the drops must therefore be taken into account.

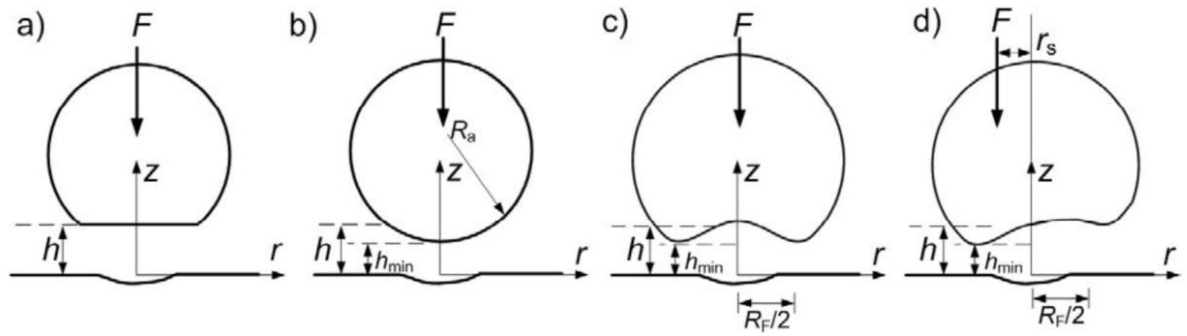

Fig. 3-7 : Model for drop deformation: disk model (a), rigid sphere model (b), symmetrical dimple model (c) and assymetrical dimple model (d). [27].

An alternative to rigid droplets is to consider that the film between two relatively close drops is assumed to be a shape like disc leading to the disk model (cf. case a in Fig. 3-7). Coulaloglou and Tavlarides used the disc model to evaluate the coalescence time between two given drops [14]. The disc model induces a coalescence time proportional to the driving force, which may be counterintuitive. In addition, Henschke has shown that models assuming rigid spherical drops [7] or a film of constant thickness, the disc model, are not able to correctly describe the reality in an extraction system [5].

It has been shown experimentally that a dimple is formed during film drainage when the drops are close enough represented in the dimple model (cf. case c and d in Fig. 3-7) [9, 15, 28]. A dimple is characterized by the thickness of the film between the drops not being constant. It has a maximum thickness along the central axis between the drops and has a thinner edge.

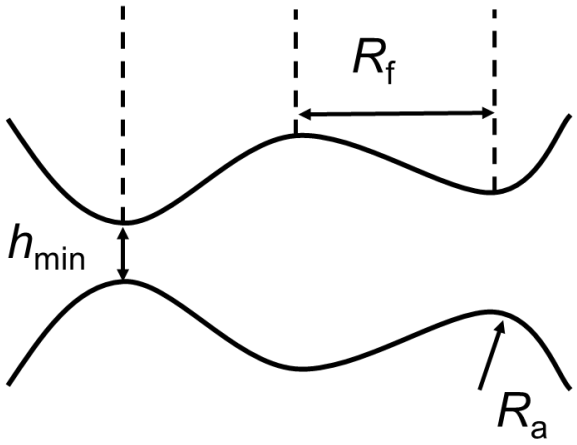

Fig. 3-8: Cross-sectional view of an asymmetric dimple

In fact, experiments [38, 56, 57] show that this dimple is not radially symmetric, which affects the drainage (cf. case d in Fig. 3-7). Henschke has therefore proposed a model that includes this asymmetry, leading to faster drainage than in the symmetrical case, by superimposing the model for symmetrical dimple drainage with an asymmetric driving force [15]. As shown in Fig. 3-8, the asymmetric dimple is characterized by its area, defined by a radius, R_F. The dimple has a variable thickness with a maximum at its center. Unlike the symmetrical dimple, the thickness of the asymmetrical dimple is also variable around its edge and reaches a minimum thickness, h_{min}, on one side of the dimple. The periphery is also characterized by a radius of curvature, R_a.

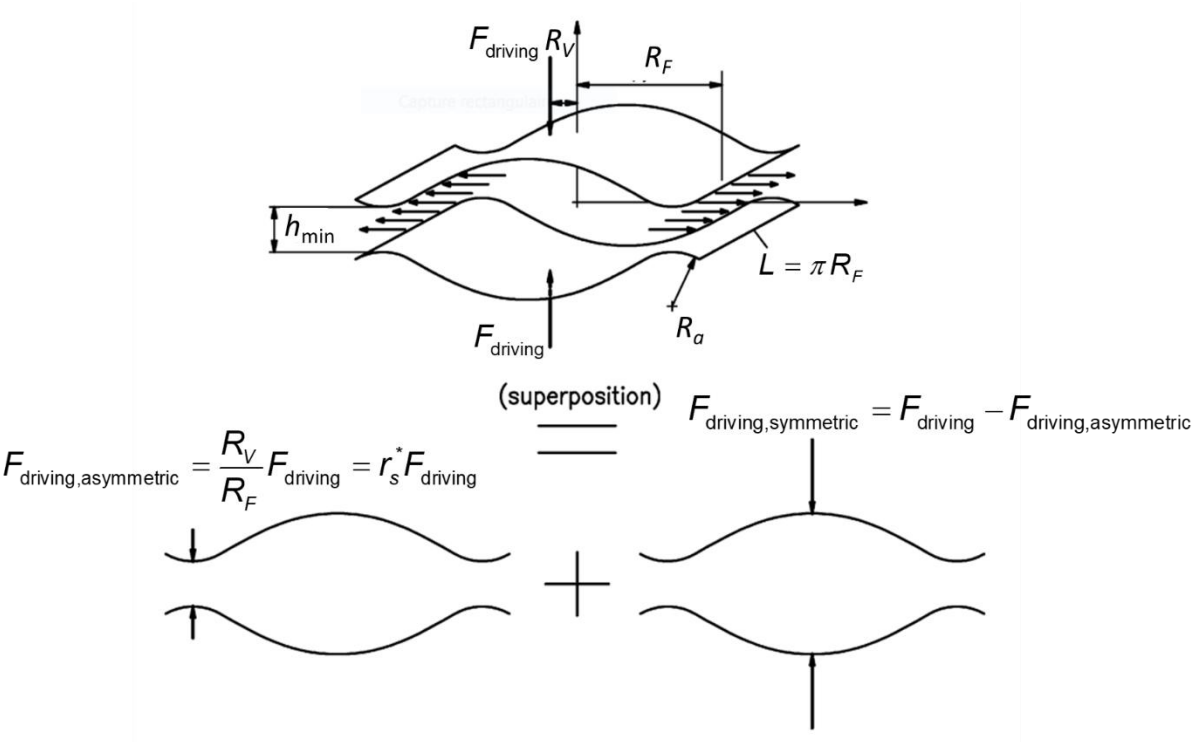

Fig. 3-9: Asymmetry in the dimple formation between two contacting drops [5]

The asymmetric dimple is also shown differently in Fig. 3-9, which is a different representation used for modelling purposes. As illustrated, the figure displays the dimple in linear form, with the perimeter of the dimple being defined by the two lengths L.

Henschke assumed that the asymmetry is induced by a decentering of the driving force relative to the center of the dimple. The driving force can be split into two contributions, as shown in the lower part of Fig. 3-9.

The decentering of the driving force is characterized by the dimensionless parameter r_s^*, which is the ratio between the driving force offset with respect to the dimple's symmetry axis, R_V, and R_F:

$$r_s^* = \frac{R_V}{R_F} \quad . \tag{3-28}$$

r_s^* can thus vary between 0, i.e. completely symmetrical, and 1, i.e. completely asymmetrical. The parameter must be fitted to experimental data of each real material system, e.g. using a standardized settling cell as proposed by Henschke [15] and refined here in chapter 6.

Due to the dimple geometry, film drainage is mainly limited by the flow through the minimum thickness of the dimple, which is also the location where drops coalesce when the minimum thickness falls below a critical value.

The model of Henschke evaluating the coalescence time was rederived in order to include the driving force explicitly in the expression, which is not the case in the original version of Henschke [5]. The derivation of the Eq.3-29 is shown in the appendix 11.4, leading to:

$$t_{\text{coalescence}} = \frac{6\pi^2 \mu R_F R_a^{3/2}}{F_{\text{driving}} r_s^* \sqrt{h_{\text{critical}}}} \quad . \tag{3-29}$$

Here, h_{critical} is the minimum film thickness below which the film of the dimple film breaks and the drops coalesce. Henschke avoided this parameter by an elegant but not straightforward elimination. This parameter appears explicitly in the model developed here.

Eq. 3-29 is the general expression for the coalescence time. The dimple radii, R_a and R_F, and the driving force depend on the equipment and on the drop environment. These variables have yet to be defined. R_a and R_F and F_{driving} have yet to be defined. However, these variables can only be evaluated once the fluid dynamics and drop geometry have been developed in chapter 4. Therefore, chapter 5 will be dedicated to determining these variables.

4 Drop Sedimentation Velocity

Sedimentation velocities of drops strongly influence the separation of liquid-liquid dispersions in several ways. For example, the drop velocity affects the drop collision and thus the coalescence probability, as explained in Chapter 3.2. In addition, looking at the overall picture of liquid-liquid dispersion separation, as shown in Fig. 1-1, at the lower end of the dispersion, the drop velocities define the slope of the sedimentation curve and thus affect the time required for phase separation. Finally, the separation of liquid-liquid dispersions is characterized, in most cases, by drop sedimentation that is faster than coalescence. This induces a gradient of hold-up along the height of the dispersion with an accumulation of droplets near the interface where hold-up can reach relatively high values in some cases leading to droplets being in a close-packed contact. In this case, the continuous phase flows through the remaining interstitial space between the droplets, due to gravity and buoyancy, still inducing a sedimentation of the droplets relative to the continuous phase.

Therefore, using the correct droplet sedimentation model is critical to accurately simulate and physically understand the separation of dispersions.

The sedimentation models found in the literature typically begin by describing the velocity of an individual drop in an infinite medium, as described in Chapter 4.1. An additional layer of complexity is added for the evaluation of the sedimentation velocity of drops in a swarm. Indeed, interactions can occur between neighboring drops, such as collisions. The greater the hold-up, i.e. concentration of drops, the more interactions there will be between the drops, and the more the drops will be slowed down. In addition, a swarm of drops has an influence on the overall viscosity of the surrounding volume, which tends to increase with the hold-up. Swarm of drops changes also the average density of the surrounding volume. The changes in viscosity and in density cause the droplets to slow down during their sedimentation in a swarm. The hold-up therefore has an impact on the sedimentation velocity of the drops. The influence of the hold-up is referred to as the swarm effect, which is described in detail in Chapter 4.2 with several cases depending on the drop environment.

Drops can settle freely if the hold-up is relatively small, which is the first case discussed in chapter 4.2.1. The drops can also be in contact with each other in the close-packed zone, which is the second case discussed in chapter 4.2.2.

4.1 Single-Drop Velocity

In order to model the sedimentation velocity of droplets in liquid-liquid dispersion, the first step is to evaluate their single-drop velocity, v_∞, which is the velocity of a drop in an infinite medium.

The single-drop velocity is determined by the balance of the major forces acting on the drop, i.e. the gravity force, F_{gravity}, the buoyancy force, F_{buoyancy}, and the drag force, F_{drag}:

$$F_{\text{gravity}} = \frac{\rho_{\text{d}} g \pi d_{\text{drop}}^3}{6} \quad , \tag{4-1}$$

$$F_{\text{buoyancy}} = \frac{\rho_{\text{c}} g \pi d_{\text{drop}}^3}{6} \quad , \tag{4-2}$$

$$F_{\text{drag}} = \frac{\rho_c v_\infty^2 C_D \pi d_{\text{drop}}^2}{8} \quad , \tag{4-3}$$

where, ρ_{d} is the density of the dispersed phase, ρ_c the density of the continuous phase, g the gravitational acceleration and C_D the drag coefficient. The gravity-buoyancy force, $F_{\text{gravity-buoyancy}}$, is given by the combination of Eqs. 4-1 and 4-2:

$$F_{\text{gravity-buoyancy}} = \frac{\Delta\rho g \pi d_{\text{drop}}^3}{6} \quad , \tag{4-4}$$

where,

$$\Delta\rho = \left|\rho_{\text{d}} - \rho_{\text{c}}\right| \quad . \tag{4-5}$$

The gravity-buoyancy force is countered by the drag force in absolute values:

$$F_{\text{gravity-buoyancy}} = F_{\text{drag}} \quad . \tag{4-6}$$

The resulting single-drop velocity is:

$$v_\infty = \sqrt{\frac{8\Delta\rho g d_{\text{drop}}}{6\rho_c C_D}} \quad . \tag{4-7}$$

The drag coefficient is described using a suitable model, where various models have been proposed over the years, most of them based on certain assumptions, if not empirical.

The drag coefficient accounts for the fluid-dynamic behavior through the Reynolds number, Re_∞, and the Archimedes number, Ar:

$$\mathrm{Re}_\infty = \frac{\rho_c d_{\mathrm{drop}} v_\infty}{\mu_c} \quad , \tag{4-8}$$

$$\mathrm{Ar} = \frac{\rho_c \Delta\rho g d_{\mathrm{drop}}^3}{\mu_c^2} \quad , \tag{4-9}$$

where, μ_c is the dynamic viscosity of the continuous phase.

Various drag coefficient models have been developed over the years to describe the drag coefficient. The first relevant model was established by Stokes [63] and many other models have been developed since [4]. Many models define the drag coefficient as a function of the Reynolds number [64-67]. Reynolds number dependent models require iterations to solve for the sedimentation velocity as function of drop diameter and therefore long computation times to evaluate the drag coefficient. This is detrimental in the case of numerical evaluations such as those produced in this study. For exactly this reason, Henschke developed his own model to evaluate the drag coefficient of an isolated drop based on the Archimedes number, which does not require iteration to evaluate the drag coefficient. This model is based on experimental evaluation of the sedimentation rate of isolated droplets in a continuous liquid phase [16]. In addition, the model can be used over a wide range of Reynolds number ($\mathrm{Re}_\infty < 3\ 10^5$). Based on these arguments, the Henschke model has been selected as the single drop velocity model used in the ReDrop program:

$$C_D = \frac{432}{\mathrm{Ar}} + \frac{20}{\mathrm{Ar}^{1/3}} + 0.51\frac{\mathrm{Ar}^{1/3}}{\mathrm{Ar}^{1/3} + 140} \quad , \tag{4-10}$$

4.2 Swarm Velocity

4.2.1 Below Close-Packed Limit

In liquid-liquid dispersion, for relatively low hold-up, the sedimentation of droplets is disturbed due to the interactions with the neighboring droplets and the change of the viscosity and

density of the surrounding environment. The absolute sedimentation velocity of drops in a swarm, v_s, is thus reduced compared to the velocity of an isolated drop, v_∞.

For most authors [68-71], the swarm velocity is proportional to the single-drop velocity, where the proportionality factor depends on the hold-up, ε:

$$v_s = v_\infty (1-\varepsilon)^n \quad , \tag{4-11}$$

here, *n*, is the swarm exponent. The swarm velocity, v_s, is the absolute velocity of the drops. The relative velocity, v_r, between the drops and the continuous phase is given by:

$$v_s = v_r (1-\varepsilon) \quad , \tag{4-12}$$

which results from an overall balance of volumes fluxes in a settling experiment. Inserting Eq. 4-12 into Eq. 4-11 results in:

$$v_r = v_\infty (1-\varepsilon)^{n-1} \quad , \tag{4-13}$$

Different models characterizing the swarm exponent have been proposed, some of which are listed in Tab. 4-1.

Richardson and Zaki, similar to the Stokes model for the single-drop velocity, is the first relevant model developed to describe the swarm velocity, which is frequently applied in the literature [4,61]. As shown in Tab. 4-1, the swarm exponent in the Richardson and Zaki model is evaluated differently for Reynolds-number ranges. Eq. 4-14 is the adjusted version of the Richardson and Zaki model. In the original model, the parameters of the model generated jump at the change of equation.

Most of the later developed models evaluate the swarm exponent with a single equation covering the whole range of the Reynolds number such as to the model of Garside and Al Dibouni. Garside and Al-Dibouni developed their model to describe the velocity of rigid spheres during sedimentation and fluidization. The authors showed that their model is more accurate than the model of Richardson and Zaki especially for hold-up above 10%. This model is therefore worth analyzing in relation to Richardson & Zaki's reference model.

The model of Garside and Al Dibouni and the model of Richardson and Zaki describe the swarm exponent based on the Reynolds number of the single-drop velocity. In contrast, Richardson and Khan developed a model where the swarm exponent instead depends on the Archimede number.

authors	models	
Richardson and Zaki [69]	$n=\begin{cases} 4.65 & \text{for } \mathrm{Re}_\infty < 0.2 \\ 4.4\mathrm{Re}_\infty^{-0.03} & \text{for } 0.2 < \mathrm{Re}_\infty < 1 \\ 4.4\mathrm{Re}_\infty^{-0.1} & \text{for } 1 < \mathrm{Re}_\infty < 500 \\ 2.4 & \text{for } \mathrm{Re}_\infty > 500 \end{cases}$	(4-14)
Richardson and Khan [68]	$\frac{4.8-n}{n-2.4} = 0.043\mathrm{Ar}^{0.57}$	(4-15)
Garside and Al-Dibouni [70]	$\frac{5.1-n}{n-2.7} = 0.1\mathrm{Re}_\infty^{0.9}$	(4-16)

Tab. 4-1: Different models expressing the swarm exponent

In addition, Garthe [43] has developed his own model based on an innovative new approach that includes a virtual drop in the equation. The corresponding virtual-drop diameter, d_v , is based on the real-drop diameter and the local hold-up:

$$d_v = d_{\text{drop}}\left(1-\varepsilon\right)^{4.65/3} \quad . \tag{4-17}$$

The single-drop velocity of the virtual drop, $v_{\infty,v}$ is then evaluated. The relative swarm velocity is then taken to be proportional to the virtual -drop velocity:

$$v_r = v_{\infty,v}\left(1-\varepsilon\right)^{1.65/3} \quad . \tag{4-18}$$

4.2.2 Above Close-Packed Limit

If the droplets settle freely, they will eventually reach the main interface of the system. In most cases, coalescence with the main interface is so slow that the drops sedimenting are slowed down near the interface. In the extreme case, the continuous phase will be squeezed out from the dispersion next to the main interface until the drops continuously touch to form what is known as close-packed zone. This region is characterized by the arrangement of droplets touching each other being squeezed together forming a network of channels between them

filled with the continuous phase. When coalescence with the main interface occurs, the continuous phase initially present around the drop that has just coalesced with the interface is released. This newly released volume of continuous phase has to then flow through the channels in the close-packed zone resulting in a relative sedimentation velocity of the drops. The relative sedimentation velocity is described in detail for a variety of cases in this sub-chapter.

Similar to the case of hold-up below the close-packed limit, the sedimentation velocity can be evaluated from a force balance.

First, the gravity-buoyancy force still applies in the close-packed zone. However, as the drops touch each other, the gravity-buoyancy force of one drop is transmitted to the next drop through the contact area between the drops. This creates a hydrostatic pressure along the height of the close-packed zone:

$$\Delta P_{i,\mathrm{hstat}} = \Delta\rho g\,\varepsilon\Delta h \quad , \tag{4-19}$$

where, $\Delta P_{i,\mathrm{hstat}}$ is the hydrostatic pressure and Δh is the height of the close-packed zone.

Secondly, the flow of the continuous phase through the interstitial space between the drops induces a pressure drop acting in the opposite direction to the hydrostatic pressure. This pressure drop, $\Delta P_{i,\mathrm{hydr}}$, describes the pressure loss along the channels that tends to slow the flow of continuous phase via drag. $\Delta P_{i,\mathrm{hydr}}$ depends on the pore size and is expressed here by the Carman-Kozeny equation [4]:

$$\frac{\Delta P_{i,\mathrm{hydr}}}{\Delta h} = -\frac{\mathrm{K}'\mu_c v_{\mathrm{r}}}{d_{\mathrm{pore}}^2} \quad , \tag{4-20}$$

where, K' is a constant characteristic of the porous medium, v_{r} the liquid velocity in the pore channels and d_{pore} is the pores equivalent diameter. Based on several experimental data, K' is usually set to 5 for system of compacted rigid spheres [4]. The pores equivalent diameter quantifies the pores size and depends on the drop deformation. Drop deformation leads to an increase in Young-Laplace pressure. This pressure is assumed not to influence the flow of the continuous phase in the pores of the close-packed zone.

As both pressures, $\Delta P_{i,\mathrm{hydr}}$ and $\Delta P_{i,\mathrm{hstat}}$, are applied on the contact surface between the drops, Eqs. 4-19 and 4-20 are balanced:

$$\Delta P_{i,\text{hydr}} = \Delta P_{i,\text{hstat}} \quad . \tag{4-21}$$

The balance can be solved for the relative velocity between the drops and continuous phase, v_r:

$$v_r = \frac{g\Delta\rho\varepsilon d_{\text{pore}}^2}{K'\mu_c} \quad . \tag{4-22}$$

The remaining unknown variable is the pore equivalent diameter that characterizes the pore dimension. The pore equivalent diameter is expressed by the ratio between the volume of the continuous phase in the dispersion, V_c, i.e. the pore volume, and the surface of the pores, A_{pores}:

$$d_{\text{pore}} = \frac{V_c}{A_{\text{pores}}} \quad . \tag{4-23}$$

The relation between the volume of continuous phase and the volume of the corresponding dispersed phase, V_d, is given with the hold-up:

$$V_c = \frac{(1-\varepsilon)V_d}{\varepsilon} \quad . \tag{4-24}$$

The pores diameter at high hold-up is evaluated based on the deformed drop geometry, which is quite challenging due to the polydispersity as differences in the drop diameter change the degree of deformation between neighboring drops. Large drops are more susceptible to deformation than small ones. To overcome these challenges, mono-sized drops is assumed as a first approximation. Henschke has modelled the deformation of mono-sized drops in the close-packed zone assuming that the droplet diameter is equal to the Sauter mean diameter, d_{Sauter} [5]. His model is used here as the reference model.

The drops in the close-packed zone are arranged to form a regular network of drops in contact with each other. As the drops are assumed to be the same size, each of them is surrounded by 12 other neighboring drops. As shown in the Fig. 4-1, Henschke thus assumed that the surrounding of each drop can geometrically be represented like a dodecahedron with regular edge length of *a*. Due to the pressure applied to the drops, they deform so that the drops have flat surfaces, A_F, on each face of the dodecahedron, A_{penta}, defined by its characteristic height,

b. These flat surfaces are shown by the dotted surfaces of the dodecahedron shown in the Fig. 4-1. The polydispersity of the drops will induce the formation of irregular polyhedra.

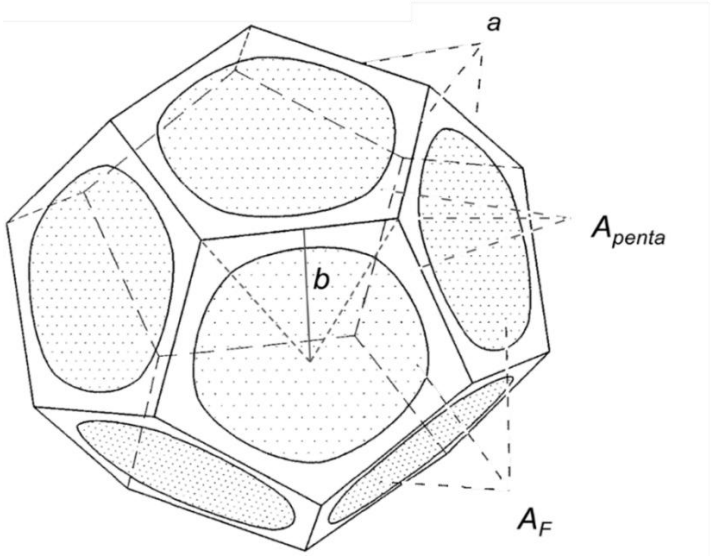

Fig. 4-1: Drop squeezed in a regular dodecahedron [5].

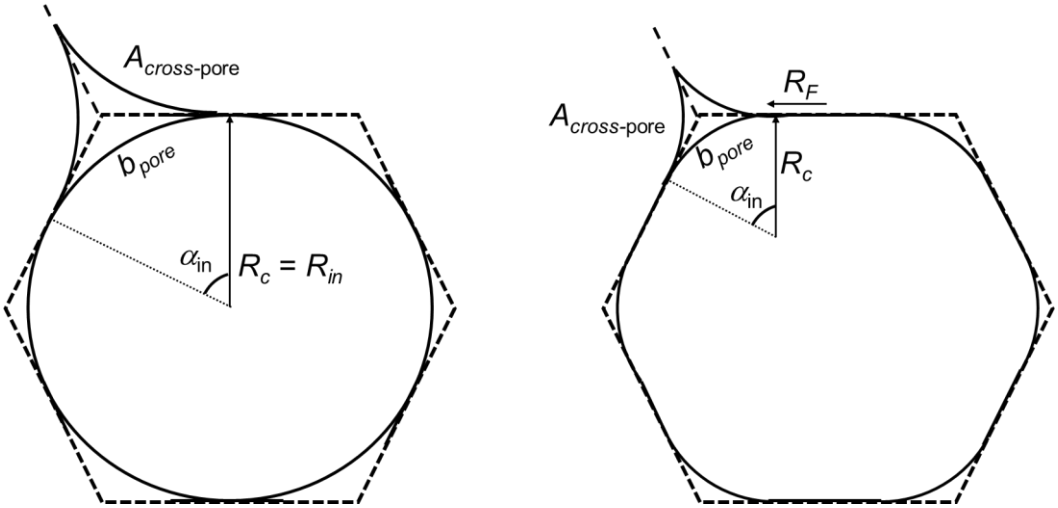

Fig. 4-2: Cut of the dedocahedron-like shape of a drop (right) and of the corresponding inscribed sphere.

The Fig. 4-2 shows a cross-section of a strongly deformed drop on the right and an undeformed drop on the left. On the left side, the drop remains spherical and is inscribed in the dodecahedron. The drops are shown as solid lines and the boundaries of the dodecahedron as dashed lines. On each corner of the dodecahedron, the curve segment of the drop shown in both cases has a length equal to b_{pore}, a curvature of radius R_c, and an angle α_{in}. The contact surface

between the drop and the dodecahedron in the picture on the right, i.e. the surface A_F of Fig. 4-1 is characterized by its radius R_F.

In order to describe the flow of the continuous phase through the interstitial space between the drops, two limiting cases can be considered. The first case, illustrated on the left side of Fig. 4-2 depicts a scenario where the drops are in contact only in a single point, and the entire interface of each drop is in direct contact with the continuous phase. This configuration is encountered by the drops as they just reach the close-packed zone. The second case is characterized by $\varepsilon \to 1$, where only small channels of continuous phase with a cross-sectional area $A_{\text{cross-pore}}$ and a length approaching the edge of the dodecahedron.

The dimension of these pores must necessarily be evaluated via their characteristic diameter for the calculation of the drop sedimentation velocity as shown in Eq. 4-22.

Before evaluating the pores size in term of hold-up and drop diameter, the geometry of the dodecahedron, shown in Fig. 4-1, shall be characterized. The volume of the dodecahedron, V_{dode}, and the radius of the inscribed sphere, R_{in}, can be expressed as:

$$V_{\text{dode}} = \frac{4+7\varphi}{2} a^3 \quad , \tag{4-25}$$

$$R_{\text{in}} = \frac{a\varphi^2}{2\sqrt{3-\varphi}} \quad , \tag{4-26}$$

where φ is the gold number:

$$\varphi = \frac{1+\sqrt{5}}{2} \quad , \tag{4-27}$$

and *a* is the edge length of the dodecahedron. The hold-up of the drop phase is then:

$$\varepsilon = \frac{V_{\text{Sauter}}}{V_{dode}} = \frac{\pi d_{\text{Sauter}}^3}{3(4+7\varphi)a^3} \quad . \tag{4-28}$$

This allows to determine *a* from d_{Sauter} and the local hold-up:

$$a = \sqrt[3]{\frac{\pi}{3(4+7\varphi)\varepsilon}} d_{\text{Sauter}} \quad . \tag{4-29}$$

On one face of a dodecahedron, i.e. a pentagon, further variables are shown in Fig. 4-1:

$$b = \frac{\tan^{-1}(54°)}{2} \quad , \tag{4-30}$$

$$A_{penta} = \frac{5a^2 \tan(54°)}{4} \quad . \tag{4-31}$$

The angle, α_{in}, shown in Fig. 4-2, is given by:

$$\tan\alpha_{\text{in}} = \frac{b}{R_{in}} \quad , \tag{4-32}$$

$$\alpha_{\text{in}} = \tan^{-1}\left(\frac{\tan(54°)}{\varphi^2}\sqrt{3-\varphi}\right) \approx \frac{\pi}{3} \tag{4-33}$$

The pore equivalent diameter is evaluated using the Eq. 4-23 with the pore volume, V_c, and surface area, A_{pore}. It has to be noted that at the junction of three dodecahedrons, the channels of the pore are larger as compared the channels along the edges of the dodecahedron. This effect is due to the rounded shape at the corners and is stronger at low hold-up. Here, the two limiting cases need to be analyzed, the first consists to evaluate the pore diameter for drops remaining spherical, cf. the left side of the Fig. 4-2. The second consists of considering the highly deformed drops, cf. the right side of the Fig. 4-2.

In the limiting case of a highly deformed drop, the pore volume is given by the product of the pore cross-sectional area and the length of all the edges. The cross-sectional area of the pore, $A_{\text{cross\_pore}}$, is given geometrically as shown in Fig. 4-2 :

$$A_{cross-pore} = R_c^2\left(\sqrt{3} - \frac{\pi}{2}\right) \quad . \tag{4-34}$$

The cross-sectional area of the pore, belonging to one single drop, is then multiplied by the length of all edges of the dodecahedron to give the pore volume per drop:

$$V_{\text{c}} = \frac{R_c^2}{3}\left(\sqrt{3} - \frac{\pi}{2}\right)\text{K}_{\text{dode}}a \quad , \tag{4-35}$$

in the limit of $\varepsilon \to 1$. K_{dode} is the number of edges of the dodecahedron, i.e. 30, but at lower hold up has to be corrected for the roundness at the corners.

The pore volume can be expressed as the difference between the dodecahedron volume, V_{dode}, given by the Eq. 4-25 and the drop volume:

$$\frac{R_c^2}{3}\left(\sqrt{3}-\frac{\pi}{2}\right)\mathrm{K}_{\mathrm{dode}}a=\frac{(4+7\varphi)}{2}a^3-V_{\mathrm{Sauter}} \quad , \tag{4-36}$$

which allows to determine $\mathrm{K}_{\mathrm{dode}}$. Eq. 4-36 is solved for the limiting case of an inscribed sphere:

$$\mathrm{K}_{\mathrm{dode}}=\frac{12\varphi^2}{\sqrt{3-\varphi}}\left(\frac{(4+7\varphi)\left(\sqrt{3-\varphi}\right)^3}{\varphi^6}-\frac{\pi}{6}\right)\approx 28.2 \quad . \tag{4-37}$$

In order to express R_c and thus to evaluate the pore volume, Eq. 4-35 is inserted into Eq. 4-24 to give:

$$R_{\mathrm{c}}^2=\frac{3V_{\mathrm{Sauter}}\left(\frac{1}{\varepsilon}-1\right)}{K_{\mathrm{dode}}\left(\sqrt{3}-\frac{\pi}{2}\right)a} \quad . \tag{4-38}$$

Eqs. 4-29, 4-35 and 4-38 allow the pore volume to be determined in terms of hold-up and drop diameter. The second variable needed to evaluate the pore diameter is the pore surface. As shown in Fig. 4-2, the pore surface is characterized by $\mathrm{b}_{\mathrm{pore}}$:

$$b_{\mathrm{pore}}=\frac{\pi R_c}{3} \quad . \tag{4-39}$$

This segment must be considered on all the edges of the polyhedron to evaluate the total surface area of the pore per drop:

$$A_{\mathrm{pore}}=\frac{\pi R_{\mathrm{c}} K_{\mathrm{dode}}a}{3} \quad . \tag{4-40}$$

The corresponding equivalent pore diameter of the deformed dodecahedron, $d_{\mathrm{pore,dode}}$, is then given by substituting the Eqs. 4-35 and 4-40 obtained for V_{c} and A_{pore} per drop into the definition of the equivalent pore diameter, Eq. 4-23, yields:

$$d_{\mathrm{pore,dode}}=\frac{R_c}{\pi}\left(\sqrt{3}-\frac{\pi}{2}\right) \quad . \tag{4-41}$$

Eq. 4-41 describes the pore diameter for high hold-up, which is the first case discussed.

The second case consists of evaluating the pore diameter for low hold-up where the drops are spherical and just touch. The volume of the pore per drop is given by Eq. 4-24:

$$V_c = \frac{(1-\varepsilon)\pi d_{\text{Sauter}}^3}{6\varepsilon} \quad . \tag{4-42}$$

As the droplets touch each other at points, the pore surface is actually the droplet surface:

$$A_{\text{pores}} = \pi d_{\text{Sauter}}^2 \quad . \tag{4-43}$$

Substitution of the Eqs 4-42 and 4-45 into 4-23 gives the pore diameter for spherical drops, $d_{\text{pores,sph}}$:

$$d_{\text{pores,sph}} = \frac{d_{Sauter}\left(1-\varepsilon\right)}{6\varepsilon} \quad . \tag{4-44}$$

Eqs. 4-41 and 4-44 describe the pores diameter for two limiting cases of hold-up. To obtain a realistic approximation of the equivalent pore diameter for any hold-up, a linear interpolation is applied between these two limiting cases:

$$d_{\text{pores}} = \frac{d_{\text{pores,sph}}\left(1-\varepsilon\right) + d_{\text{pores,dode}}\left(\varepsilon_{\text{limit}}-\varepsilon\right)}{\left(1-\varepsilon_{\text{limit}}\right)} \quad , \tag{4-45}$$

where, $\varepsilon_{\text{limit}}$, is the hold-up at the entry of the close-packed zone.

Eq. 4-28 can be evaluated for the specific case of a drop with a radius equal to the inscribed sphere to evaluate $\varepsilon_{\text{limit}}$:

$$\varepsilon_{\text{limit}} = \frac{V_{\text{inscribed\_sphere}}}{V_{dode}} = \frac{8\pi}{3\left(4+7\varphi\right)}\left(\frac{\varphi^2}{2\sqrt{3-\varphi}}\right)^3 \approx 0.755 \quad . \tag{4-46}$$

This value of $\varepsilon_{\text{limit}}$ deviates only slightly from the theoretical value for FCC packing of equal spheres and is used here to be consistent with the picture of dodecahedra characterizing the drops in contact:

$$\varepsilon_{\text{limit,spheres}} = 0.741 \quad . \tag{4-47}$$

Eq. 4-45 combined with the general equation for drop velocity Eq. 4-22 gives the complete expression for the relative sedimentation velocity of droplets above the close-packed limit.

On the other hand, the drop velocity below the close-packed limit is described by Eqs. 4-7, 4-9 and 4-13:

$$v_r = \frac{\mu_c}{\rho_c d_{\text{sauter}}} \sqrt{\frac{4\text{Ar}}{3C_D}} (1-\varepsilon)^{n-1} \quad , \tag{4-48}$$

Relative sedimentation velocities below and above the close-packed limit must be consistent and should give the same velocity for $\varepsilon_{\text{limit}}$. If this is not the case, jumps in sedimentation velocity occur, which has undesirable effect in the simulations.

Eq. 4-22 can be evaluated for $\varepsilon_{\text{limit}}$. At the entry to the close-packed zone, the drops are spherical. The equivalent pores diameter is therefore given by the Eq. 4-44. The corresponding velocity is:

$$v_r = \frac{g\Delta\rho(1-\varepsilon_{\text{limit}})^2 d_{\text{Sauter}}^2}{36K'\mu\varepsilon_{\text{limit}}} \quad . \tag{4-49}$$

Equating Eqs. 4-22 and 4-49 at $\varepsilon_{\text{limit}}$ results in:

$$\frac{36K'\mu_c^2\varepsilon_{\text{limit}}}{\rho_c g\Delta\rho d_{\text{sauter}}^3} \sqrt{\frac{4\text{Ar}}{3C_D}} = \frac{1}{(1-\varepsilon_{\text{limit}})^{n-3}} \quad . \tag{4-50}$$

From which, the swarm exponent

$$n = 3 + \frac{\ln\left[\frac{1}{24K'\varepsilon_{\text{limit}}} \sqrt{\frac{\text{Ar}C_D}{3}}\right]}{\ln(1-\varepsilon_{\text{limit}})} \quad , \tag{4-51}$$

is obtained. This swarm exponent depends only on physical properties and drop diameter via Ar. It can then be assumed that this value of *n* also applies for $\varepsilon < \varepsilon_{\text{limit}}$

Fig. 4-3 shows the comparison between the swarm exponent determined in this way as a function of drop size and the models summarized in Tab. 4-1. For sedimentation, only values up to at most 1mm are relevant, because beyond this value, the diameter of the drops is too large for the case of drops present in the free sedimentation zone observed during settling of dispersion. Note that large drops can form in the close-packed zone by coalescence, but this implies that the drops do not settle freely. Fig. 4-3, shows that the curves are quite close to each other. On the other hand, as Eq.4-51 has been developed in such a way that the behavior of the drops is continuous between the sedimentation zone and the close-packed zone, it is to be preferred for the description of the principal behavior and is used in this work.

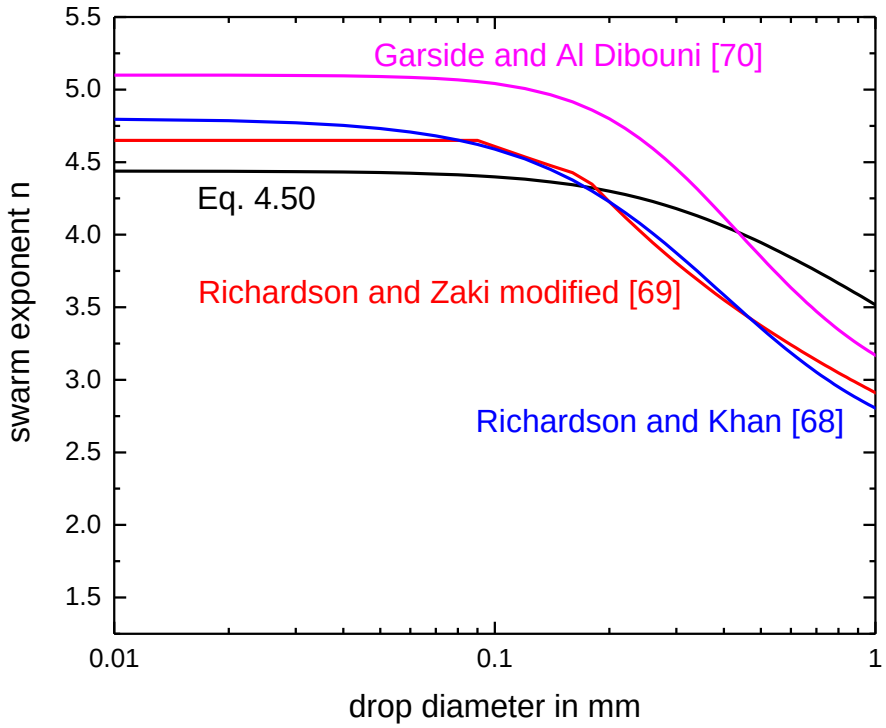

Fig. 4-3: Comparison of swarm exponent between the swarm models of Tab. 4-1 and the Eq. 4-51

The question may arise as to the relevance of the initial hypothesis of considering drops of identical size. A sensitivity analysis has been performed to evaluate the effect of polydispersity on packing. Corwin et al. model the "*random packing of polydisperse frictionless spheres*" [6]. Frictionless spheres have a chance to rearrange by passing like drops, they find that in the simplified case of monosized drops, the holdup at random packing would be 64%. This value differs from Hesnchke's proposal. However, the authors have shown that for a polydisperse mixture of hard sphere with a distribution characterized by a standard deviation of 23% around the mean diameter of the hard spheres leads to a packing limit of 66.4% [72]. This shows that polydispersity does not have a significant effect on the local hold-up for randomly-packed hard spheres. Therefore, it can be concluded that this is also the case for the dodecahedron packing, so that the hold-up of 0.755 at the lower boundary of the close-packed zone is a reasonable approximation.

5 Interactions Between Drops in Contact

As detailed in chapter 4, the dodecahedron model was developed in detail, allowing for a closer look at fluid dynamics and drop interactions, which were temporarily suspended at the conclusion of chapter 3. In this chapter, the definition of R_a, R_F and $F_{driving}$.is examined in the context of the dodecahedron model with the objective of establishing a more straightforward expression for the coalescence time.

As explained in chapter 3.4.2, when two drops come into contact, a force may act between them due to buoyancy, which pushes them together and causes the layer of continuous phase between the drops to gradually decrease until it reaches a critical thickness at which coalescence occurs: $F_{driving}$. As the two drops come together, a dimple forms. This dimple, as shown in Fig. 3-8, is characterized by two radii R_a and R_F. The characterization of these three variables depends on the configuration in which the drops are found. For example, if two drops are considered in the close-packed zone, the dimple geometry is related to the deformation of the drops, as shown in Fig. 4-2. Obviously, the situation is different for two drops in contact and moving freely in the sedimentation zone and for a single drop resting at the interface.

The aim of this chapter is to characterize the two radii and the driving force for the different configurations to develop a clear understanding of their influence on coalescence according to Eq. 3-29.

As general case, two drops in contact are subject to a Young-Laplace pressure across the contact surface, A_F :

$$F_{driving} = \Delta P_{Young\text{-}Laplace} A_F \quad , \tag{5-1}$$

which is induced by the drop curvature. As shown in Fig. 4-1 and Fig. 4-2, the area of the dimple, e.g. the contact area between the drops, is characterized by the radius R_F :

$$A_F = \pi R_F^2 \quad . \tag{5-2}$$

The formation of the dimple causes a change in the pressure difference between the inside and outside of the drop, $\Delta P_{Young\text{-}Laplace}$, described by the Young-Laplace equation, written generally as:

$$\Delta P_{\text{Young-Laplace}} = \sigma\left(\frac{1}{R_1}+\frac{1}{R_2}\right) \quad , \tag{5-3}$$

where, R_1 and R_2 are the radii of curvature perpendicular to each other. This equation can be applied to the specific case relevant here. As can be seen in Fig. 3-9 for the dimple on the line of closest approach of the drop, one radius is R_a and the second radius of curvature being much larger than R_a, for an almost flat dimple approaching infinity. This leads to

$$\Delta P_{\text{Young-Laplace}} = \sigma\left(\frac{1}{R_a}+\frac{1}{\infty}\right)=\frac{\sigma}{R_a} \quad . \tag{5-4}$$

The dimple radius is thus given by:

$$R_F = \left(\frac{F_{\text{driving}} R_a}{\pi\sigma}\right)^{1/2} \quad . \tag{5-5}$$

The Eqs. 5-5 and 3-29 can be combined to give:

$$t_{\text{coalescence}} = \frac{6\pi^{3/2}\mu R_a^2}{r_s^* \sqrt{\sigma F_{\text{driving}} h_{\text{critical}}}} \quad . \tag{5-6}$$

The Eq. 5-6 holds for all drop configuration, since Eq. 5-4 applies to all situations with R_a being one curvature and for a flat dimple the other approaching ∞ irrespective of the drop being in contact with another drop or the major interface.

The Young-Laplace pressure can also be evaluated by considering the overall geometry of the drop. 3 cases can be identified. In the first case, the drops are deformed by dodecahedra in the close-packed zone, two limiting cases can be investigated in order to evaluate the dimple curvature of drops, which are here treated as case 1a and 1b. The second consists of considering 2 drops in contact moving in the sedimentation zone. The third case consists of observing 1 drop remaining at the interface.

5.1 Case 1a - Drops in Close-Packed Zone at $\varepsilon \to 1$

The first case consists in considering the hold-up very close to 1, where the drops are dodecahedra with rather sharp edges. The channels through which the continuous phase flows are very narrow and are located at the edges of the polyhedra, shown in Fig. 4-2.

Eq. 5-3 is therefore adapted to the curvature of the channels, where one radius is given by R_c and the other radius approaches infinity since the channels in the limit are linear. The pressure difference therefore is:

$$\Delta P_{\text{Young-Laplace}} = \sigma\left(\frac{1}{R_c} + \frac{1}{\infty}\right) = \frac{\sigma}{R_c} \quad . \tag{5-7}$$

In this case, Eq.5-4 and Eq. 5-7 gives:

$$R_a = R_c \quad , \tag{5-8}$$

5.2 Case 1b - Drops in Close-Packed Zone at $\varepsilon_{\text{limit}}$

As a second case, the hold-up at the entry of the close-packed zone can be considered, where it is assumed that the drops are spherical and inscribed in the imaginary dodecahedron, as shown in Fig. 4-2. This means that:

$$R_c = R_{in} \quad , \tag{5-9}$$

where, R_{in} is the radius of the sphere inscribed in the dodecahedron, given by the Eq. 4-26. The two radii of Eq. 5-3 are thus equal to the radius of the inscribed sphere:

$$\Delta P_{\text{Young-Laplace}} = \sigma\left(\frac{1}{R_{in}} + \frac{1}{R_{in}}\right) = \frac{2\sigma}{R_{in}} \quad . \tag{5-10}$$

Equating Eq. 5-4 to Eq. 5-10 results in:

$$R_a = \frac{R_{in}}{2} \quad , \tag{5-11}$$

for this case.

Eqs. 5-8 and 5-11 represent two limit cases in the close-packed zone. Henschke interpolates both to express the radius of curvature of the dimple in the close-packed zone [5]:

$$R_a = \frac{R_c}{2}\left(2 - \frac{R_c}{R_{in}}\right) \quad . \tag{5-12}$$

5.3 Case 2 - Two Sedimenting Drops in Contact

Two freely-sedimenting drops are similar to the case of drops at the entrance to the close-packed zone, they are assumed to remain spherical. Deformation of the drops at the contact surface is negligible and does not affect the sphericity of the drops as a whole.

In contrast to the situation in the close-packed zone, where drops are assumed to be of homogeneous size equal to the Sauter mean diameter, freely settling drops can have different diameters but the same contact area, as shown in Fig. 5-1, assuming an identical dimple curvature.

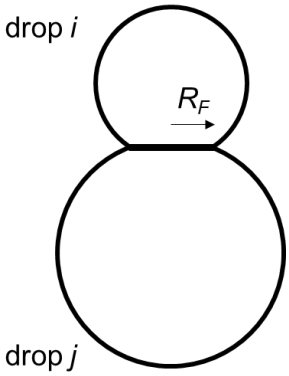

Fig. 5-1: Schematic view of the contact between two freely-sedimenting drops

It is thus appropriate to express the Young-Laplace pressure difference in terms of the equivalent radius, R_{eq} of the 2 drops, i and j:

$$\frac{2}{R_{eq}} = \frac{1}{R_i} + \frac{1}{R_j} \tag{5-13}$$

Solving for R_{eq} yields:

$$R_{eq} = \frac{d_i d_j}{d_i + d_j} \quad . \tag{5-14}$$

The Young-Laplace pressure difference for undeformed drops is evaluated from the Eq. 5-3. The two perpendicular radii, R_1 and R_2, correspond to the drop radius. The Young-Laplace pressure is thus given by:

$$\Delta P_{\text{Young-Laplace}} = \frac{2\sigma}{R_{eq}} \quad . \tag{5-15}$$

5.4 Case 3 - Drop at Interface

For the special case of a drop being in contact with the interface, the equivalent radius is equal to:

$$R_{eq} = d_i \quad , \tag{5-16}$$

since the interface is considered as a drop with an infinite diameter. The Young-Laplace pressure results again from Eq. 5-15

Eqs. 5-4 and 5-15 express the Young-Laplace pressure difference by considering two different scales, the first concentrating on the peripheral zone of the dimple while the second considers the overall geometry of the drops. Eqs. 5-4 and 5-15 thus allow to determine the radius of curvature of the dimple for two freely sedimenting drops:

$$R_a = \frac{R_{eq}}{2} \quad . \tag{5-17}$$

5.5 Driving Force Evaluation

The driving force forcing the drop to approach depends on the drop environment. Regarding an isolated drop in contact with the interface, the force is given by the difference between gravity and buoyancy of the drop:

$$F_{driving} = \frac{4\pi}{3} \Delta\rho g R_{drop}^3 \quad . \tag{5-18}$$

If two freely settling drops are visualized, they are equally subject to the difference between gravity and buoyancy compensated by the drops. If the drops come into contact and move jointly, it can be assumed that the force acting between them scales as the difference between their individual gravity – buoyancy:

$$F_{driving} = \frac{\pi \Delta\rho g \left| d_i^3 - d_j^3 \right|}{6} \quad . \tag{5-19}$$

The situation is different for drops in the close-packed zone, where the deformed drops experience at their contact areas the force induced by deformation resulting in an excess of Young-Laplace pressure which is transmitted between the drops via the contact surface of the dimple.

Note that this additional force is negligible in the case of freely sedimenting drops due to the low deformation of the drops in this specific case.

In addition, as the drops form a network of contacting drops deformed by the envisaged do-decahedra, the hydrostatic pressure is transmitted from drop to drop. This hydrostatic pressure is counterbalanced by the pressure generated by the flow of the continuous phase in the pores formed between the deformed drops in the close-packed zone. It can be assumed that, on average, these pressures cancel each other out. Therefore, for a given individual drop, the driving force is only proportional to its own gravity - buoyancy. The image is therefore that of each individual drop wobbling in a cage formed by its nearest neighbors, with the forces for the whole ensemble of drops compensating and only the individual wobbling contributing to the driving force.

The driving force acting on a drop in the close-packed zone is thus given by:

$$F_{\text{driving}} = \frac{4\pi}{3}\Delta\rho g R_{\text{Sauter}}^3 + \Delta P_{\text{Young-Laplace}} A_{\text{F}} \quad . \tag{5-20}$$

The results of this chapter are collected to give an overview in Tab. 5-1.

Drop configuration	R_{a}	F_{driving}
Freely sedimenting	$R_{\text{a}} = \frac{R_{\text{eq}}}{2}$	$F_{\text{driving}} = \frac{\pi\Delta\rho g \left\lvert d_i^3 - d_j^3 \right\rvert}{6}$
Resting at the interface	$R_{\text{a}} = R_{\text{drop}}$	$F_{\text{driving}} = \frac{4\pi}{3}\Delta\rho g R_{\text{drop}}^3$
In close-packed zone	$R_{\text{a}} = \frac{R_{\text{c}}}{2}\left(2 - \frac{R_{\text{c}}}{R_{\text{in}}}\right)$	$F_{\text{driving}} = \frac{4\pi}{3}\Delta\rho g R_{\text{Sauter}}^3 + \Delta P_{\text{Young-Laplace}} A_{\text{F}}$

Tab. 5-1: Summary of the dimple curvature and driving force expression depending on the drops configuration.

6 Settling Cell

The drop-coalescence behavior is influenced by numerous parameters such as the material properties, the drop size and the presence of trace components, e.g. ions [1]. These parameters can have significant effects on the behavior of liquid-liquid dispersions. Currently, these effects cannot be accurately predicted. Instead these effects need to be quantified with experiments. In general, these experiments are preferably carried out on a laboratory scale and are used to study the settling of liquid-liquid dispersions in batch mode.

For the chemical industry, this experimental characterization allows the design of technical equipment such as settlers or extraction columns [5, 27]. On the other hand, the purpose of these experiments in this thesis is to validate the modeling approach presented above. In both cases, however, the equipment used for these settling experiments should be standardized. This means that the results must be independent of the operating conditions, such as the user's methodology, the energy input or the volume investigated. This makes the experiments repeatable over time, and thus provides reliable results.

However, over the years, different settling devices have been developed. They lead to different characterization procedures and different results. Two of them have been selected here for comparison based on their differences, the stirring cell proposed by Henschke [5] and the shaking cell developed by Willvock, Gebauer, Kamp, Bart, and Kraume [29]. Both setups are different in many aspects, such as dispersion generation, dispersion volume, and even the settling characterization method. The aim of the following chapter is to compare both apparatuses based on their advantages and disadvantages in order to design a standard apparatus that can be used in industry for the design of technical equipment or for model validation in this dissertation.

6.1 Existing Settling Equipment

6.1.1 Stirring Cell

The stirring cell is available at the Department of Chemical Engineering of the University of Liège. The apparatus is shown in Fig. 6-1. It consists of a double-wall glass vessel with a capacity of 800 ml, a height of 18.5 cm and a diameter of 7.5 cm.

As shown in Fig. 6-1, two shafts, placed inside the vessel, are used for stirring and creating the dispersion. Each of them has four stirrers evenly distributed along the height and alternated between the shafts. Each impeller has four inclined blades. Each blade is 13 mm long and 7 mm high. The shafts are connected to a gearbox so that they rotate in opposite directions during stirring in order to reduce quickly the turbulences in the first seconds after the stirrers are switched off, without the need of baffles. The shafts are guided and aligned at the bottom of the cell by a Teflon part with two holes.

The gearbox, connected to the shafts, is driven by an agitator motor (IKA EURO-STAR, IKA WERKE, Germany). The double-walled vessel is connected to a thermostatic bath (AP15R-40-V12V ref: 462-0233, VWR, USA) and the temperature is usually set at 20°C. The cell is lit from the rear by an LED panel. The latter was built with LED strips (ref: BL339, Auralum, Germany) and with a plastic diffusion panel in front to uniform the light.

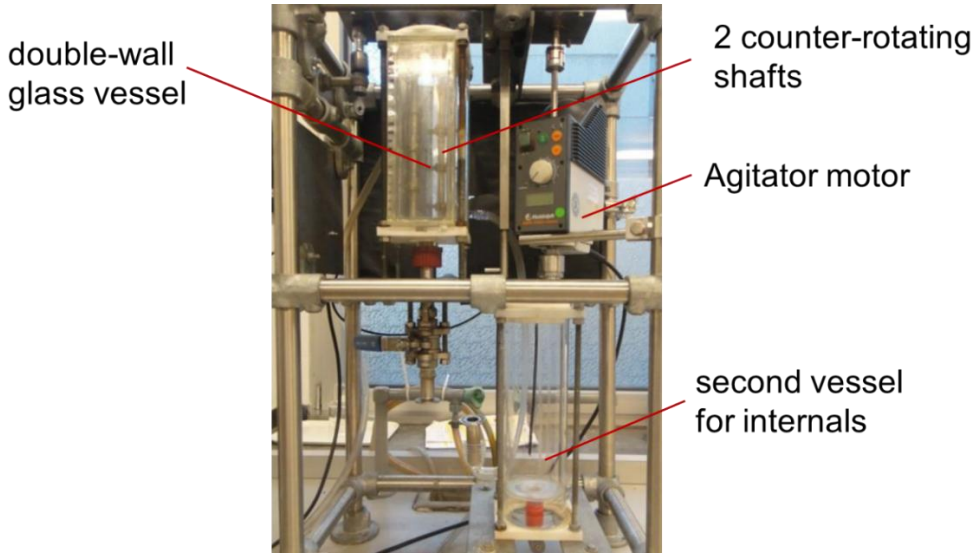

Fig. 6-1: Standardized stirring cell

Before starting the settling experiment, the vessel is filled from the top with the two phases one at the time using a funnel. The volumetric phase ratio is easily read from a scale on one side of the vessel. The cell should be filled to its maximum capacity of 800 ml to avoid the presence of air bubbles in the system or the formation of foam during mixing. A lower volume is still possible, but a minimum height of 15 cm should be maintained for reproducible results.

After the cell is filled, the motor is turned on. The speed was varied between 500 and 1000 min^{-1}. Below the lower value the dispersion is not well mixed and the upper limit is chosen for

safety reasons. Mixing was investigated between 5 seconds and several minutes to ensure a well-mixed dispersion.

It has to be noted that the cell is an open system due to the holes in the top cover. Air is therefore exchanged over time. Where relevant, introducing a nitrogen purge can be considered for safety reasons.

Once the dispersion is established, the motor is turned off and the separation can be studied in the same vessel. Henschke has demonstrated that the shafts present in the vessel have no effect on settling [5]. Alternatively, the dispersion can be transferred to a second vessel placed below the first by opening a large-bore ball valve to transfer the dispersion to the second vessel in a few seconds. Additionally, internals can be placed in this lower cell to evaluate their effect on the settling behavior for engineering-design purposes. This second vessel can also be connected to technical equipment to transfer a small volume of dispersion into it and observe the separation of the dispersion.

How phase separation proceeds is recorded with a video camera, which is placed in front of the equipment, as shown in Fig. 6-2. However, in some cases, a sideways position of the light can lead to a better visualization.

The easiest way to characterize phase separation of a dispersion is to evaluate, by visual inspection, its settling time, which is defined as the time required to separate the two-phase system. However, waiting until the last drop has coalesced would lead to large scatter due to the stochastic nature of individual coalescence events. To overcome this problem, Henschke proposed to define the settling time as the time until half of the interface remains covered by a monolayer of drops. This definition ensures reproducible results. This evaluation method will be referred to as the visual method. A top view of the interface is required to determine this settling time.

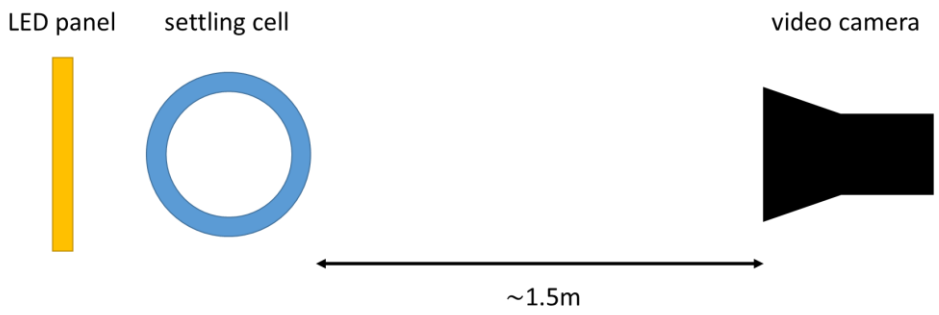

Fig. 6-2: Original setup for video recording (top view)

In addition, the video of the experiment can be analyzed. To better visualize the phase separation, from the frames of the videos at equal time intervals, a slice of the vessel can be chosen. When the individual slices are placed side by side, they provide a complete picture of the experiment, as shown in Fig. 6-3. This representation leads to a quantitative evaluation of sedimentation and coalescence curves. These data are typically used to design technical equipment.

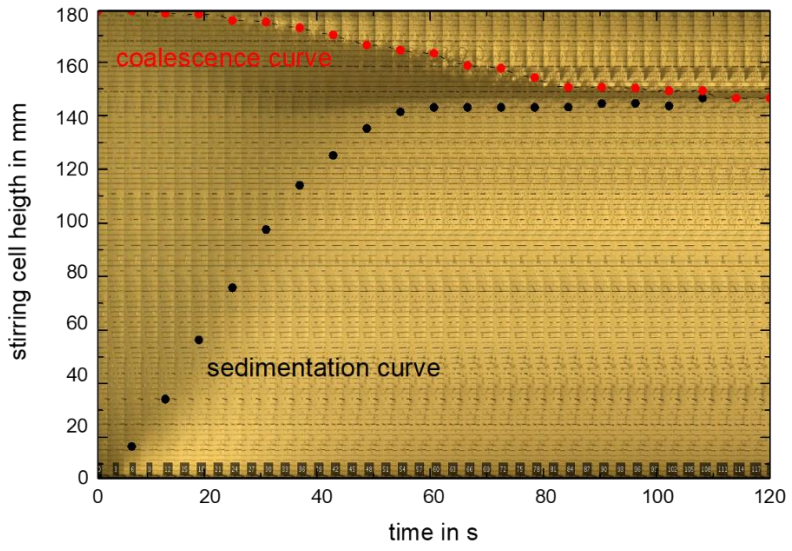

Fig. 6-3: Settling experiment representation at equal time step

6.1.2 Shaking Cell

The shaking cell was developed at the University of Berlin and was also used at the TU Kaiserslautern. An identical apparatus, shown in Fig. 6-4, was built in Liège for this study. The central part of the shaking cell consists of 2 glass square bottles of 100 ml (ref: SCTV501127, VWR, USA). 2 bottles are used for repeatability reasons or to compare two systems with each other. The bottles are placed between a stainless-steel plateau at the bottom and a stainless-

steel plate at the top. 4 M4 threaded rods are used to secure the bottles between these two stainless steel parts. The two bottles with the supporting part constitute the shaking table of the unit.

The plateau on which the bottles are placed has 4 linear ball bearings at each corner to allow a vertical movement guided by 4 rods of 1 cm diameter. The center of the table is connected to the motor (WEG IEC 60034-1, WEG, France) through a crank that allows the vertical movement of the shaking table with an amplitude of 2.7 cm.

The LED panel, also used for the stirring cell, is placed behind the shaking table for better visualization of the experiment.

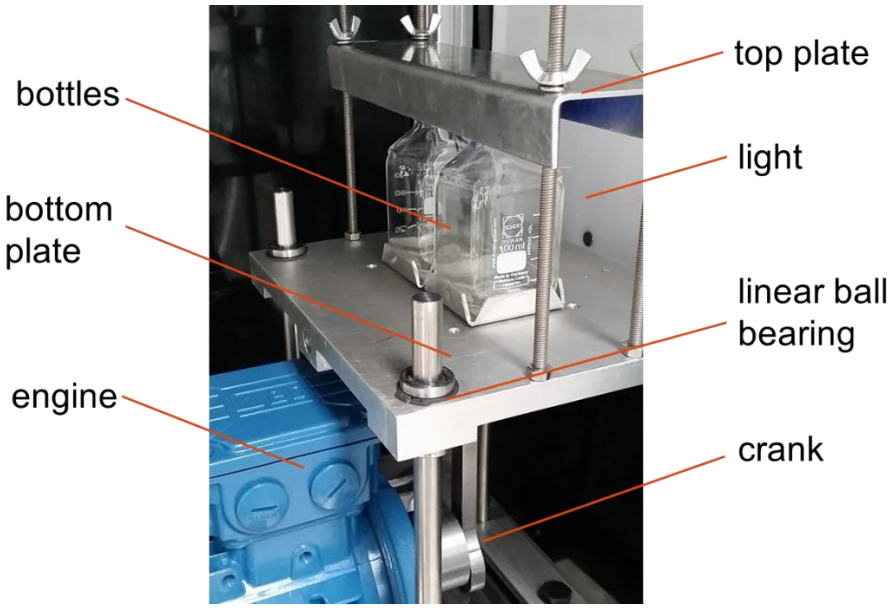

Fig. 6-4: Shaking cell

Before starting the shaking experiment, the bottles are filled with the solvents of the two-phase system with the same phase ratio in order to control the repeatability of the experiments. For practical reasons, the bottles are filled with 75 ml of the system, which is the volume needed to reach the neck of the bottle. If the filling volume exceeds this level, the reduction of the bottle diameter in the region of the neck would have to be taken into account when quantitatively evaluating the phase separation. In addition, the presence of an air fraction allows good mixing of the two-phase system. The two bottles are mounted firmly on the shaking table and the motor can then be switched on.

To produce a dispersion, the motor has been operated between 5 s and several minutes as for the stirring cell. However, the mixing intensity was varied between 400 and 650 min^{-1}. The lower limit corresponds to the minimum requirement to produce a homogeneous dispersion. The maximum mixing speed is chosen for safety reasons.

Since the bottles are closed by caps during mixing, the system is closed, so there is no air exchange during the shaking or settling.

After the dispersion has been created, the motor is turned off and the settling of the dispersion is recorded with a video camera. The setup for video recording is identical to that for the stirring cell, shown in Fig. 6-2.

The settling time is evaluated from the movie using a numerical routine. An efficient routine to facilitate this quantitative evaluation has been written in MATLAB, the code is available in Appendix 11.8. The program focuses solely on an area of interest (AOI) defined by the user as proposed by Willvock, Gebauer, Kamp, Bart, and Kraume [29]. The AOI is centered around the interface, as shown by several examples in Fig. 6-5. The width of the AOI is chosen to avoid the wall effect by the side walls and its height is a few mm up to 1 cm above and below the interface. The exact location of the interface is chosen manually by the operator. For each frame of the settling experiment video, the numerical routine evaluates the averaged gray levels of both phases within the AOI. The averaged grey levels of one frame are compared to those of the last frame within that AOI, resulting in a relative gray level that decreases with time. A threshold is set by the user for both phases, which defines when sufficiently clear phases are obtained and thus the settling time is reached. This evaluation method will be referred to as the numerical method.

6.2 Cell Comparison

Shaking and stirring cells differ in many ways. A summary of the obvious differences is listed in the Tab. 6-1.

Since it has been claimed that the settling time can be determined correctly and reproducibly by either equipment, the goal is here to obtain a quantitative understanding on which parameters the experimental settling times depend.

The two-phase system chosen for the settling experiments consists of paraffin oil and deionized water. The paraffin oil is chosen in the framework of the ERICAA project (Grant number: 03ET1391A-F, financed by the Federal Ministry for Economic Affairs and Energy) for safety reasons due to its low vapor pressure. To obtain repeatable results, NaCl is added to the aqueous phase at a concentration of 50 mmol/L. This eliminates the effect of trace components. The concentration is chosen according to Schwerin and Pfennig [34] and Soika and Pfennig [60] who studied the influence of ions on the settling behavior. For more information on the solvent, see Appendix 11.7.

parameter	stirring cell	shaking cell
settling time evaluation	visual	numerical
dispersion generation	stirring between 5 s and several minutes with an intensity between 500 and 1000 min^{-1}	shaking between 5 s and several minutes with an intensity between 400 and 650 min^{-1}
volume	600 to 800 ml	60 to 75 ml
air exchange	open system	closed system

Tab. 6-1: Summary of the differences between the shaking and stirring cells.

6.2.1 Settling-Time Evaluation Method

The visual and numerical methods for evaluating the settling experiments result in the same variable: the settling time. To compare the results of both methods, both methods are applied in parallel to both devices and for the identical material system in order to compare them on identical basis.

A sensitivity analysis is performed for each method. The visual method is used by the operator performing the settling experiment. Settling time can vary from operator to operator due to differences in perception. Regarding the numerical method, the different parameters that play a role in the evaluation are varied in order to evaluate their impact on the final evaluation. These parameters are the area of interest centered on the interface and the thresholds in greyscale below which the phases above and below the interface are considered. The different

areas of interest tested for both cells are shown in Fig. 6-5. Nine AOIs for the stirring cell are tested and located between two stirrers to exclude the influence of the stirrers on the evaluation. For the shaking cell, due to the presence of the meniscus, three AOI are tested. For both cells, the AOI are varied in height and width. The tested thresholds vary between 8 and 12% for the upper phase and 2 and 5% for the lower phase.

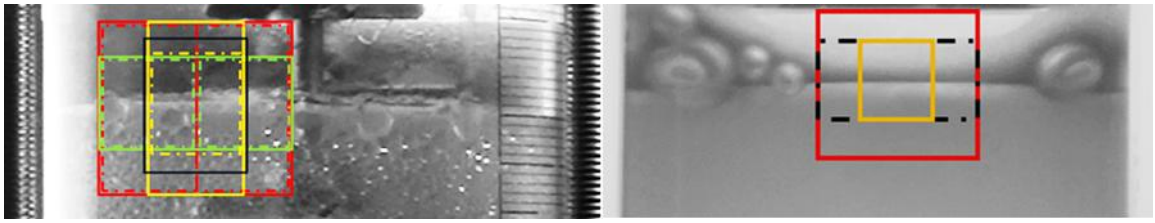

Fig. 6-5: Representation of the different areas of interest for the stirred cell (left) and the shaking cell (right)

The results for the stirring cell are summarized in Tab. 6-2. To characterize the statistical error for the evaluated settling time, each settling experiment has been performed three times. The choice of area and thresholds does not significantly affect the settling time. Also, the visual criterion gives similar results compared to the numerical method.

Fig. 6-6 shows the evolution of the average grey level evaluated for each frame of the video and for each zone located on either side of the interface. The average grey levels are relative to the average grey level of the last frame of the video of one settling experiments performed with the stirring cell. The orange area on the graph shows the variability of the numerical settling time for the variation in the thresholds. The evolution of the curves shows a slow but relatively steady decrease of the integrated grey level difference over time, where it is obvious that a change of the threshold defining the end of the settling automatically leads to a change of several seconds for the resulting settling time, as shown in Tab. 6-2 and by the orange area in Fig. 6-6. Both evaluation methods thus lead to settling times in a narrow range as long as the thresholds are set to reasonable values, i.e. less than 12% for the upper phase and less than 5% for the lower phase.

	settling time in s
different areas of interest	63 - 74
different threshold	64 - 71
visual criterion	70 - 77

Tab. 6-2: Influence of the parameters of the numerical methods in comparison with the visual criterion for the stirring cell

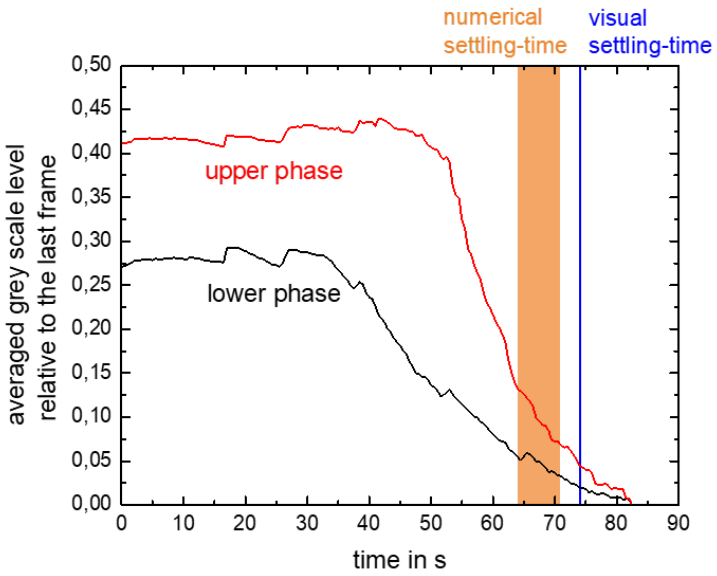

Fig. 6-6: Evolution of the relative averaged grey scale for the upper and lower phases for a settling experiment performed with the stirring cell.

The same sensitivity analysis was performed with the shaking cell by changing the AOI and the thresholds. The results are displayed in Tab. 6-3.

	settling time in s
different areas of interest	196 - 200
different threshold	196 - 207
visual criterion	120

Tab. 6-3: Influence of the parameters of the numerical methods in comparison with the visual criterion for the shaking cell

It turns out that the choice of area of interest is less important for the shaking cell than for the stirring cell. But even for the stirring cell, the variation is relatively small. Overall, a change in the thresholds leads to variations of 6 to 11 seconds for both devices. However, the visual criterion results in a significantly different settling time for the shaking cells due to the wall effects of the small size of the bottles. When the interface in the center of the bottles is already free of drops, leading to the visual criterion being reached, there are still drops at the walls of the bottles that strongly influence the numerical evaluation. Therefore, looking only at the front of the bottles gives a misleading indication of the settling time. The visual criterion also has the advantage of allowing the settling time to be measured directly "in situ", as opposed to the numerical evaluation, which requires the video to be uploaded and processed using the appropriate MATLAB software, making the visual method easiest to use. Also, because of its better performance, the visual criterion was used for all the subsequent experiments carried out in this study.

6.2.2 Dispersion Generation

Two parameters can be varied to generate dispersion with the two cells: mixing time and motor speed. Thus, a sensitivity study of these parameters has been performed. The purpose of this variation is to define the experimental parameters so that the system is well mixed but no stable emulsion is formed. The shaking speed is varied from 400 to 650 min^{-1} and the mixing time from 5 to 90 s. The stirring speed is varied from 500 to 1000 min^{-1} with a mixing time from 5 s to 1 min. For slow (less than 400-500 min^{-1}) and short (less than 5 seconds of mixing) stirring or shaking, the dispersion is not properly generated and the experimental settling times are too short.

The corresponding settling time results are shown in Fig. 6-7. For both cells, the settling time is represented based on the mixing parameters: mixing time and motor speed. As both parameters are increased, a plateau is reached within which the settling times remain relatively stable. The plateau of the stirring-cell data is illustrated by the blue area in the graph. Within this relatively large parameter range, the settling time is stable with respect to both mixing parameters. The situation is different for the shaking cell. The red triangle shows the data where the settling time does not vary, this region is much more restricted for the shaking cell. Beyond the triangle, the operating conditions lead to dispersions that take an extremely long time to

separate or where the settling time cannot be determined due to an excess of very fine droplets produced, making evaluation difficult. This infeasible region for the shaking cell is indicated by the red area at the top of the graph.

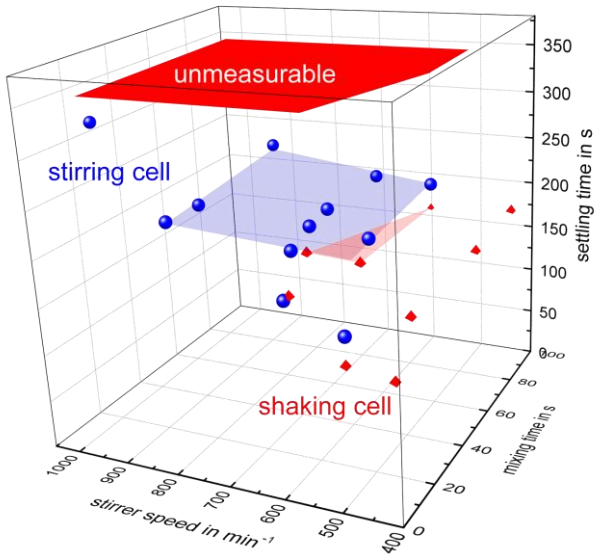

Fig. 6-7: Evolution of the settling time with the mixing time and the mixing speed. The system consisted of paraffin oil and water, phase ratio: 1/2 (o/a)

The sensitivity study showed that a variation in the mixing parameters does not affect the separation time for the stirring cell, unlike the shaking cell. This suggests that the results of the settling experiments are repeatable over a wide range of parameters for the stirring cell.

6.2.3 Air Exchange

To study the effect of air exchange on separation, both cells were tested. The settling experiments were repeated for both equipment at two-hour intervals. During this time, the two-phase system was left in the open air. The two bottles of the shaking cell were left open, whereas the stirring cell is an open system anyway. The results are shown in Tab. 6-4. Air exchange apparently has a strong influence on the settling behavior. This may be due to the evaporation of low boiling fractions of paraffin or to the dissolution of carbon dioxide leading to a shift in the ionic composition of the aqueous phase.

While the shaking cell shows different settling times between the two hours, the results obtained with the stirring cell don’t change significantly due to air contact.

	settling time in s	
	shaking cell	stirring cell
first experiment	170	242
second experiment after 2 hours allowing an exchange with the air	320	240

Tab. 6-4: Influence of the air exchange performed on both equipment

6.2.4 Volume of the Dispersion

The quantitative evaluation of the sedimentation and coalescence curves from the experimental video, as shown in Fig. 6-3 for the shaking cell, can in principle be performed with both devices. However, according to previous work, 8 cm diameter and at least 15 cm height are recommended to avoid to strong influence of wall effect on coalescence and to allow sufficient vertical resolution in quantifying settling behavior [5]. The evaluation of the curves for the shaking cell is thus questionable.

To test if larger bottles lead to more reliable data with the shaking cell, shaking experiments are then performed with 1L square bottles. These shaking tests were not successful: a liquid-liquid dispersion in a 1L bottle cannot be produced with the current shaking cell. Different mixing speeds and different filling volumes have been tried without success. The crank should be replaced to increase the amplitude of the vertical motion to induce better mixing.

The comparison is thus made between the devices in their current configuration: two 100 ml bottles for the shaking cell and the 800 ml vessel for the stirring cell. The dispersion volumes in these cells can still be varied to evaluate the influence of a change in volume and a change in the air fraction within the settling cells.

A different settling behavior is expected for variation of the studied dispersion volume, since it affects the mixing and also may induce air bubbles and foam in the system. Different dispersion volumes are tested to evaluate the effect of the air fraction on the settling behavior. The results are shown in Tab. 6-5. It has to be kept in mind that a different sedimentation height implies a different settling time. In order to compare two experiments with different dispersion volumes,

the sedimentation and coalescence models are fitted to the experimental sedimentation and coalescence curves of the first experiment [5, 15]. These model parameters are then used to predict the settling behavior for the second experiment.

	stirring cell (600 min^{-1}, 30 s)		shaking cell (420 min^{-1}, 15 s)	
	800 ml	600 ml	75 ml	60 ml
settling time evaluated visually in s	245	238	180	160
prediction of the settling time based on the experiment of larger volume in s		213		164

Tab. 6-5: Influence of the filling height on the settling time

The predicted settling time of the low height experiment is consistent with the settling time evaluated with the fitted models for both apparatus. This proves that no significant extra effect induced by filling height can be observed experimentally.

6.3 Optimal Settling Cell

The parameters investigated in this study show significant differences between the two settling cells. A brief summary of the comparison is given in Tab. 6-6. Each criterion presented in detail in the text is listed and placed on a scale from '-' to '++' for both cell.

First, the choice of method for evaluating the settling time is discussed. As demonstrated by tests conducted during this study, the numerically evaluated settling-time with the shaking cell, as initially proposed, can lead to biased results if wall effects are observed. This issue does not arise in the case of the stirring cell, as outlined in paragraph 6.2.1. Additionally, visual evaluation of settling time is a possibility with the shaking cell; however, the size of the bottles restricts the evaluation. While the numerical settling-time evaluation method can be applied to the stirring cell, it requires additional setup and data processing steps that can be avoided by directly applying the visual criterion.

Second, the stirring cell is stable with respect to air exchange, mixing time and mixing speed. This is not the case for the shaking cell. On the other hand, the air fraction in the cell does not

seem to affect the settling behavior for either cell. Finally, the configuration of the stirring cell offers some additional features such as temperature control and a precise evaluation of the settling and coalescence curves due to its sufficient height [5].

	cell	
	stirring	shaking
mixing time & stirrer speed	++	-
air exchange	++	-
filling-height influence	++	++
evaluation of settling curves	++	+
wall effect	+	-
temperature control	++	-

Tab. 6-6: Summary of the comparison between the stirring and the shaking cell

As a general observation, the dispersion studied in the stirring cell shows a settling behavior more independent of the operating conditions compared to the shaking cell. Thus, the stirring cell together with the visual evaluation of the settling time is clearly preferable to the shaking cell for reliable determination of the settling time. The larger height of the stirring cell allows for more accurate resolution of the sedimentation and coalescence curves facilitating more precise determination of the characteristic drop diameter and coalescence parameter for settler design. Based on the experiments performed here and the experiences gained, some modifications are proposed to add additional features to the final equipment for the optimal settling cell:

- The cell is placed in a black box to protect the cell from daylight to improve the optical evaluation of the experiments. The black box consists of a frame covered with black and opaque plastic sheets. A fan is attached to the bottom of one side of the apparatus to be used as a fume hood.
- The gearbox and top seal are assembled together to facilitate cell assembly.
- An additional hole is realized in the top cover to allow insertion of an optical probe for drop-size evaluation.

- An additional inlet is provided in the top of the stirring cell to allow for nitrogen purge, which is required if flammable solvents are used during the experiment.
- A lateral inlet is realized in the glass vessel to fill the cell with a dispersion directly coming from a technical equipment.
- The stirrers are thicker than in the previous version to ensure their straightness, and they are guided by ball bearings in the bottom of the cell. This avoids vibrations during the stirring process and reduces the risk of glass breakage when connected to a technical device.

The final equipment is shown in Fig. 6-5 without all the safety devices, i.e. the black box, the shield around the drive belt and the nitrogen flushing tubes, in order to have a clear view of the equipment. The drawings of all parts and the assembly procedure are explained in Appendices 11.5 and 11.6. If desired, a second vessel can be installed below and connected to the upper cell as shown in Fig. 6-1 to investigate the influence of internals with an identical dispersion.

Fig. 6-8: Optimized settling cell based on Henschke's standardized stirring-cell design

7 Iso-Optical System for Model Validation

The ReDrop tool provides a complete representation of settling by evaluating the hold-up profile versus time and along the height of the dispersion. In order to validate the ReDrop program and thus the models used for the description of drop behavior, it is ideally necessary to measure the settling profiles experimentally. The measurement of the hold-up generates a multitude of data about the drop behavior, for example the drop packing in the close-packed zone or the settling velocity or even information about the lag time. This data is useful for consistent validation of the different models.

However, conventional settling experiments provide only limited data, such as the settling and the coalescence curves, as well as the settling time. Efforts can be made to measure additionally the initial drop-size distribution, e.g. with a SOPAT probe. But collecting more information about the settling behavior is quite challenging. Some attempts have been made at the University Aachen RWTH and TU Graz using, respectively impedance measurement and ultrasonic measurement to evaluate the hold-up, with large scatter in the measured data [76-79]. Another solution is to measure, from the settling-experiment recording, the light intensity and use some correlation to determine the hold-up. For usual systems, such correlation can actually not be established since light intensity depends on the drop concentration but also on the drop size due to the difference in refractive index between the phases.

In order to measure the hold-up as a function of light intensity, one solution is to use an iso-optical system. This special solution consists of two liquid phases that have the same refractive index. In practice, this means that the drop interface is not visible. A dye is then added to one of the phases to allow determination of the hold-up of that phase. During the settling experiment, the intensity of the dye is directly proportional to the drop concentration and thus to the hold-up according to the Beer-Lambert law:

$$\varepsilon = B \log \frac{I_0}{I} \quad , \tag{7-1}$$

where, I_0 is the transmitted light intensity of the two-phase system without the dye, I is the light intensity when the dye is added to one of the phases and B is the proportionality factor.

7.1 Experimental Procedure and Materials

7.1.1 Experimental Setup

The settling experiments are performed in the settling cell described in chapter 6.3. The settling cell is illuminated from behind by an LED panel. A camera (Canon EOS 1300D) is placed in front of the settling cell to record a video of the settling process. The camera is mounted on a tripod and controlled by a computer using the "digicam control" program to prevent the camera from moving during recording. Computer control is also useful for adjusting the zoom and positioning of the camera.

During the recording of the settling, disturbances of the light intensity must be avoided as much as possible. Preliminary tests are performed without any liquids in the cell to evaluate the stability of the light intensity over time. The result of this study shows that the LED panel must be turned on 1 hour before recording to stabilize the light intensity. The recording must start a few minutes before the actual settling experiment to allow the camera sensor to heat up. As a final precaution, the settling cell is placed in a black box to prevent interference from external light sources.

7.1.2 Preparation of the Iso-Optical System

The iso-optical system used here consists of distilled water, hexane (VWR, lot: 18Z1660), and ethylene glycol (VWR, lot: 18H024016). The distilled water is produced with the GFL 2001/4 unit (GFL, Burgwedel, Germany). The dye added is methylene blue (Applichem, lot: 2K005003), which preferentially partitions into the aqueous phase. Since the cell does not have a double envelope, all liquids are kept in bottles immersed in a thermostatic bath (AP15R-40-V12V ref: 462-0233, VWR, USA) at 20°C for a few hours. After temperature equilibration of the solvents, the cell is first filled with dyed water (concentration of methylene blue is 2 mg/L approximately) and hexane in the correct amount for the phase ratio to be tested. Then the stirrer is turned on and the ethylene glycol is slowly added. The ethylene glycol is soluble in water but not in hexane. As the ethylene glycol is added, the refractive index of the aqueous phase slowly changes to match the refractive index of the organic phase. When the iso-optical point is reached, the drop interfaces are no longer visible and stirring is maintained for additional 30 minutes for equilibration.

After the settling experiment, sufficient amounts of each phase are collected to measure density, viscosity, and interfacial tension.

For each experiment, both equilibrium phases were analyzed for density and viscosity using the DSA 5000M densitometer in combination with a Lovis 2000ME viscosimeter from Anton Paar, Graz, Austria. The interfacial tension is measured with the tensiometer Lauda TD. The results are presented in the appendix in Tab. 11-4 for the different settling experiments.

7.1.3 Hold-up Measurement

Once the iso-optical system is prepared and in equilibrium in the settling cell, the settling experiment is performed and recorded with the video camera. The video is then analyzed with MATLAB, the evaluation program is shown in Appendix 11.9. On each frame, the grey level is averaged horizontally, resulting in a vertical pixel line with height-dependent grey levels from each frame of the video. These vertical lines are placed side by side to visualize the complete evolution of the separation. The grey level in the image varies between 0 and 255, corresponding to dark and white, respectively.

The two parameters of the Beer-Lambert law, B and I_0, are evaluated from this overall picture. The first vertical pixel line corresponds to the initial hold-up and the last vertical pixel line correspond to a hold-up equal to 0 above and 1 below the interface of the dispersion. As the greyscale intensity, I, and the hold-up, ε, for these two vertical lines are known, I_0 and B of Eq. 7-1 can be backed out for each vertical pixel individually.

Once the two parameters are evaluated, they are used to convert the light intensity picture to the hold-up values using the Eq. 7-1.

7.1.4 Drop-Size Measurement

The SOPAT probe (SOPAT-VR-Sc, SOPAT, Berlin) is used to measure the initial drop-size distribution. At the iso-optical point, however, the droplets are not visible to the probe. The drop size is therefore measured for a near iso-optical system. Near iso-optical systems are created by adding an excess of one of the phase-forming components, such as water or ethylene glycol. Then, the drops are easily visible. Two measurements are made, one with a small excess

of water and one with a small excess of ethylene glycol. Excesses of 5 ml for each chemical over a total volume of 1 L are used. Both drop sizes are shown in Fig. 7-1 for one example.

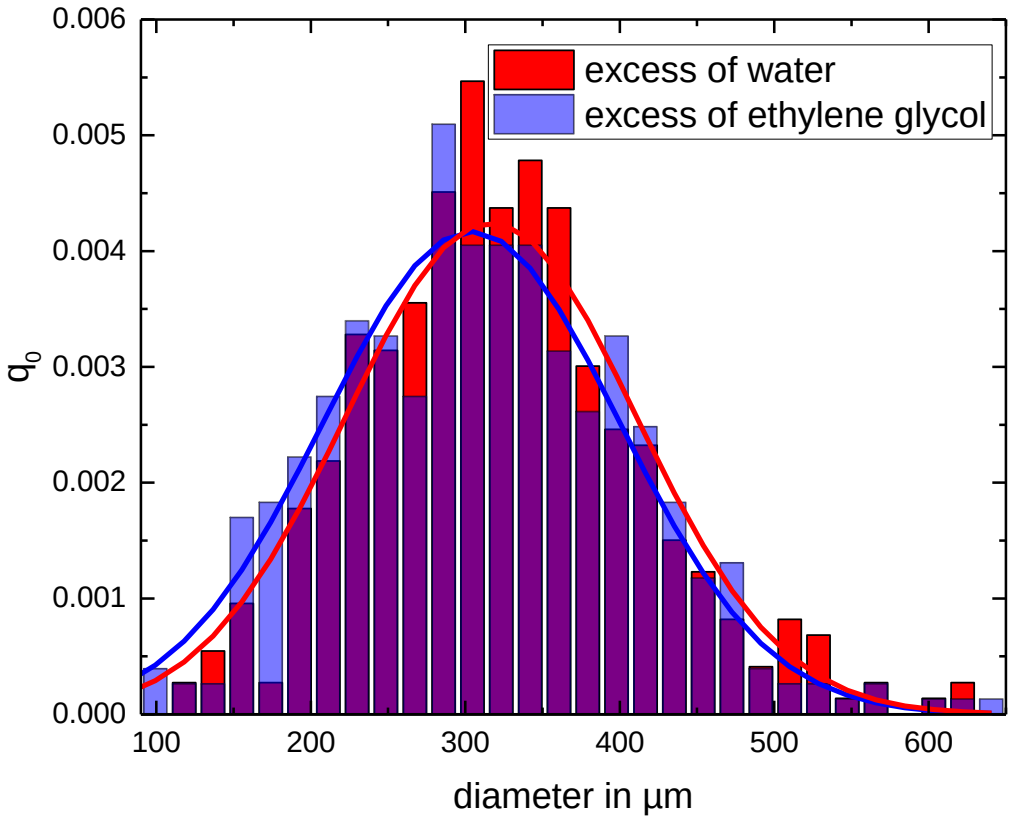

Fig. 7-1: Measurement of drop-size distribution for a near iso-optical system. Phase ratio (O/A): 37%

Since the drop sizes turn out to be very similar around the iso-optical point, it is sufficient to measure one of the two distributions according to Fig. 7-1. Thus, to characterize the drop size for the different settling experiments, a single drop-size distribution measurement was carried out for the system close to the iso-optic point with an excess of water only.

7.2 Experimental Results

Three different phase ratios have been analyzed. For each of them, two mixing speeds have been chosen: 650 and 800 min^{-1}. The results are shown in Fig. 7-2 and Fig. 11-19 to Fig. 11-23. The white stripes are the zones where the hold-up cannot be measured. In these regions, the light intensity is disturbed by the interface, the bottom, and the top of the cell.

The initial drop-size distribution is measured individually for each system, i.e. different phase ratio and different mixing speed with the SOPAT probe. The mean and the variance of each drop-size distribution are summarized in the appendix in Tab. 11-5 for the different settling experiments, and the detailed distributions are shown in Fig. 11-24 to Fig. 11-29. In the different figures, drop-size distributions are particularly well described by a lognormal distribution.

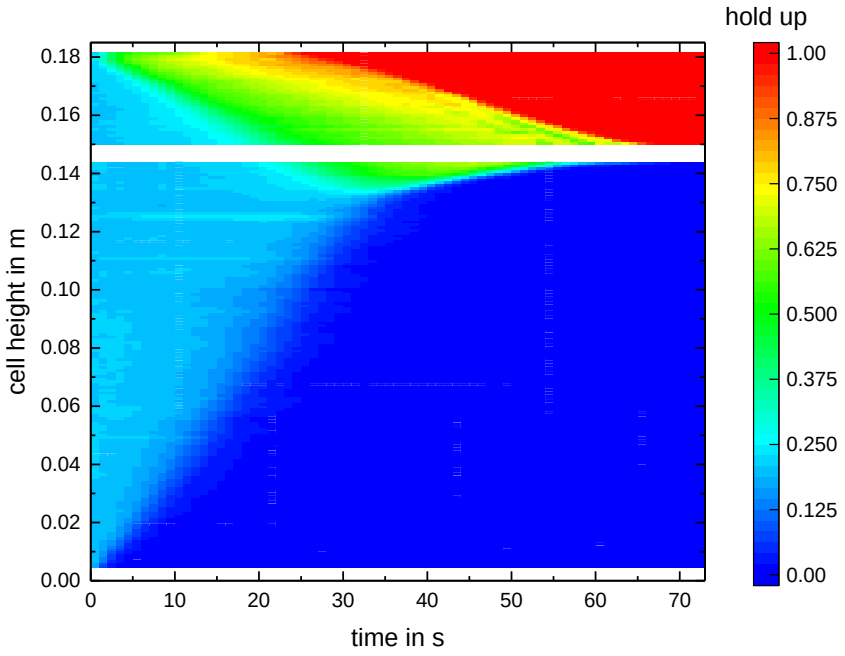

Fig. 7-2: Settling of the iso-optical system for an initial holdup of organic phase of 20.52%. Mixing speed to produce the dispersion set to 650 min^{-1}.

The different experimental results show the presence of a more or less pronounced lag-time at the beginning of the settling. As the sedimentation and coalescence curves gradually take shape, two distinct hold-up zones are observed. The first, the free sedimentation zone, shows a relatively constant hold-up close to the initial value. As the drops settle, they reach the second zone, which is characterized by a larger hold-up that increases with the height of the dispersion. However, the hold-up value above 0.755, which defines the beginning of the close-packed zone, is rarely reached in the different iso-optical experiments. The transition from one zone to the other shows a rather abrupt change in the hold-up.

8 ReDrop Simulations and Discussion

After the holdup profiles have been obtained by the settling experiments with the iso-optical system, the next step is to validate the mathematical models describing the behavior of droplets in a liquid-liquid dispersion undergoing separation. As explained above, the different models have been implemented in the ReDrop program. The experimental data obtained during the iso-optical experiments are used to validate the models by fitting their parameters.

However, the ReDrop program itself also has parameters that determine its performance. These intrinsic parameters must first be appropriately chosen to ensure robust and reproducible simulations before fitting the parameters of the mathematical models. Due to the stochastic nature of ReDrop, it is important to verify the reproducibility of the simulations.

Therefore, this chapter is divided into two parts. The first part focuses on the optimal choice of the ReDrop simulation parameters. The second part focuses on the fitting of model parameters to optimally represent experimental data.

8.1 Optimising Parameters Intrinsic to ReDrop

The ReDrop tool is a Fortran program that evaluates the settling of a liquid-liquid dispersion over time. At each incremental time step, the program evaluates the behavior of each representative drop present in the simulated system, its sedimentation velocity and thus its new vertical position in the dispersion and whether the drop in question coalesces with any other drops it may meet during that time. The duration of this time step is the first intrinsic parameter of ReDrop. Working with a time step means that the program evaluates the drops behavior before and after the time step in question and, consequently, that any interaction between the drops during this time step is evaluated by the ReDrop program. If the time step is too long, systematic deviation is observed from real behavior. On the other hand, if the time step is too short, the resolution will be very fine, and the computation time will be significantly longer. The time step must therefore be chosen carefully.

The ReDrop tool divides the dispersion into height elements. For each height element, from the vertical positions of all drops, the average holdup can be evaluated. The holdup is assumed to be the holdup at the centre of the height element. Then, the holdup at a particular height of

the dispersion is evaluated by linear interpolation using the values evaluated at the centre of each height element. The height of these height elements is thus another intrinsic parameter of ReDrop. If the height elements are too large, the evolution of the hold-up on height will not be smooth but with abrupt changes from one height element to another. This will lead to inconsistencies in the simulations. However, if the height elements are too small, the hold-up will evolve more smoothly, but the calculation time will be longer.

The representative drops accounted for in ReDrop represent a larger set of drops with similar characteristics e.g. in terms of size and height. As the simulation progresses over time, the number of representative drops will tend to decrease due to coalescence, reaching in critical cases an insufficient number of drops to provide a statistically stable picture of the evolution of the dispersion. The program is therefore designed to continuously adjust the number of drops per height element, which corresponds to a variation of the cross-sectional area A_{repr} by duplicating randomly chosen drops to match the defined limits. A minimum and a maximum number of drops per height element defining the range within which the number of drops is maintained with this algorithm, are therefore the last intrinsic parameters of the program to be adjusted in order to guarantee relevant simulations.

In summary, the four parameters essential to the operation of the program are the time step, the number of the height elements, and the minimum and maximum number of drops in each height element. To reduce the number of these parameters, the maximum number of drops per height element has been chosen as 1.5 times the minimum number, since that has proven appropriate in preliminary studies.

A sensitivity study was performed to select the optimal values for these four parameters. To this aim, the ReDrop program was used to fit the simulations to the experiments. The coalescence parameter and the collision parameter were adjusted during the fitting based on the sum of squares (SSQ) evaluated on the evolution of the experimental and simulated hold-up. The SSQ was computed from the relative deviations between simulation and experiment at each point of the sedimentation and coalescence curves, as well as from the relative deviations in holdup between simulation and experiment. The holdup deviations were normalized by the number of measurement points. Weighting factors were then applied to these various deviations: a weight of 1 for deviations in the positioning of the coalescence and

sedimentation curves, and a weight of 20 for deviations in holdup. Finally, the SSQ was evaluated over the entire set of settling experiments. At the end of the fitting, the program converges to the r_s^* and $C_{\text{coll,buoyancy}}$ parameter values that result in the lowest SSQ.

The SSQ, evaluated in this way for the experiment with a hold up of 34.67% and a stirrer speed of 800 min^{-1}, was then evaluated in order to select the optimal values for varying the three intrinsic ReDrop parameters, the time step, the number of the height elements, and the minimum number of drops in each height element. Each parameter was varied incrementally, and for each of its values three independent simulations were performed, with different starting values for the pseudo-random number generation to depict the stochastic nature of ReDrop. For each simulation, the SSQ was computed. The results are presented in Fig. 8-1.

The results show that increasing the simulation resolution, i.e. decreasing the time step, reduces the SSQ. However, this reduction becomes negligible within the stochastic scatter of ReDrop results once the time step is below 0.02 s. For the number of height elements a similar behavior is observed above 150 height elements. At this value the ReDrop results are not yet completely independent of this parameter. Nevertheless, this value has been chosen to keep the simulation times in a reasonable range. The minimum number of drops per height element has little effect, so 150 drops per element were chosen. With these parameter settings, the simulation results become essentially independent of time-step resolution, height element number, and the number of drops at this level of fineness.

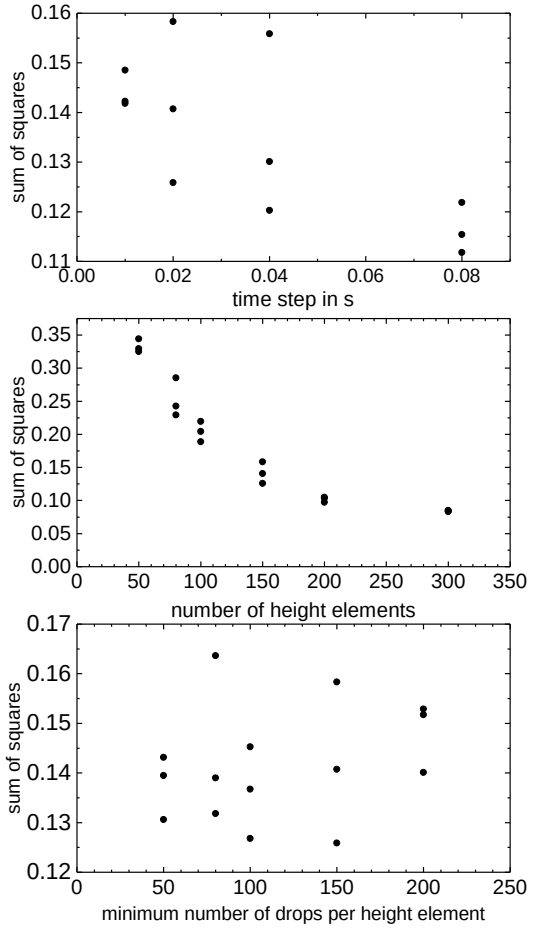

Fig. 8-1: SSQ as a function of the three intrinsic ReDrop parameters: number of height element, minimum number of drops per height element and time step.

8.2 Validation of the Mathematical Models

Now that the inherent parameters of ReDrop have been chosen to ensure robust simulations, the coalescence model can be validated. Several experiments were carried out with the same solvent system but with different hold-ups and different mixing speeds before separation of the dispersion. Since the models fundamentally describe drop-drop interactions, the different system-specific model parameters implemented in ReDrop must be identical for the different experiments with the identical material system. In chapters 3 to 5, various theoretical models relevant to each physical phenomenon were discussed and critically compared; only the models selected through that analysis have been implemented in ReDrop. Accordingly, the validation described here concerns only those chosen models.

From the different models used in ReDrop, only the models characterizing the drop interaction, i.e. collision frequency, and the coalescence time depend on parameters. Three parameters must be adjusted during fitting: the Boublik, Mansoori, Carnahan, Starling and Leland [22] parameter, C_{BMCSL}, the collision frequency parameter, $C_{\text{coll,buoyancy}}$ and coalescence parameter r_s^*.

At first, different simulations were carried out by varying the Boublik and Mansoori, Carnahan, Starling and Leland parameter. The resulting simulations did not give satisfactory results, so that the BMCS model is not included in subsequent simulations. This contribution to collision probability may thus be relevant for the simulation of extraction columns as shown by Kopriwa [27] but is apparently not relevant for settling if that is simulated as in ReDrop.

The remaining parameters to be fitted are thus the coalescence parameter r_s^* and the collision-frequency parameter $C_{\text{coll,buoyancy}}$. These two parameters were fitted for the different settling experiments performed with the iso-optical system using the initial drop-size distribution as measured. The results are shown in the Fig. 8-2 and in the annex 11.11. For each graph, the hold-up evaluated during the simulations is represented by the color scale over time and over the total height of the dispersion. The characteristic coalescence curve is represented by the black color boundary at the top. The sedimentation curve is then represented by the white curve and the black curve bellow the sedimentation curve represents the limit below which no droplets are present, i.e. hold-up equal to 0. The sedimentation curve is evaluated on the basis of a hold-up equal to 10% of its initial value, which corresponds well with the experimentally observed curves as observed in Fig. 8-2. In the vicinity of the sedimentation curve, the hold-up decreases rapidly from its initial value to near zero. The black points represent the corresponding experimental curves. It is important to note that the fitting procedure relies on both the hold-up data and the characteristic curves, incorporating a weighting factor as reported above. Each plot was generated with the same values for both parameters, r_s^* and $C_{\text{coll,buoyancy}}$ equal, respectively, to 4.6944×10^{-03} and 8.0603×10^{2}. It is assumed that the coalescence parameter r_s^* is system specific and to be fitted for each individual material system and is independent of holdup but depends on direction of dispersion, while the $C_{\text{coll,buoyancy}}$ is assumed to be determined for the iso-optical system and then assumed to be general for all material systems. The results are summarized in Tab. 8-1. The data evaluated during the ReDrop simulations include other number of parameters, such as the diameter of the drops,

as shown in Fig. 8-3. The ReDrop simulation provides information on the remaining hold-up once settling is complete, i.e., when the sedimentation and coalescence curves intersect. For example, Fig. 8-2 and Fig. 8-3 show that small droplets remain below the sedimentation curve even at the end of the simulation, despite the hold-up evolution approaching zero.

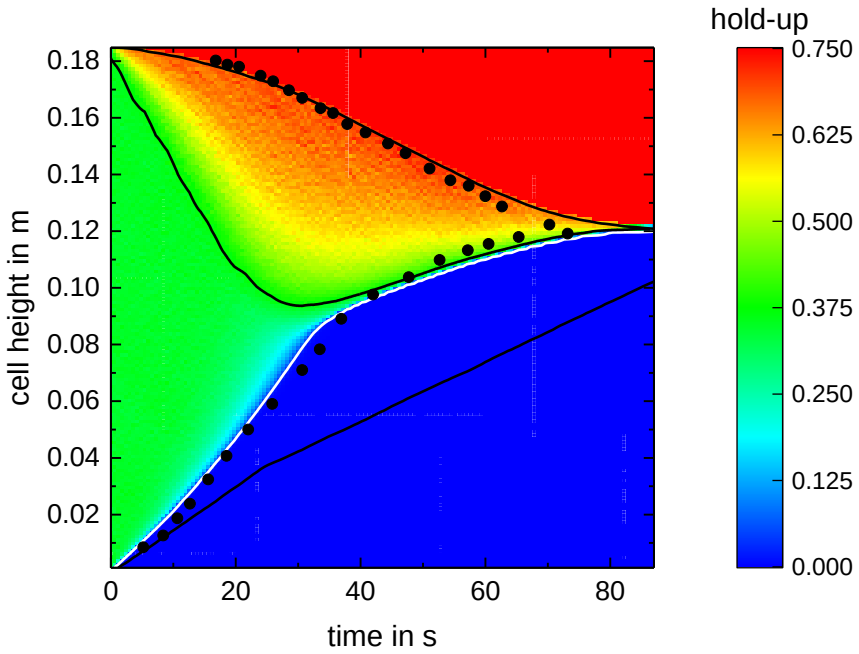

Fig. 8-2: ReDrop simulation of the settling of the iso-optical system for a phase fraction of 34.67% at mixing with 650 min^{-1}.

experiments		SSQ
phase fraction	stirring speed in min^{-1}	
20.52%	650	$2.905x10^{-2}$
	800	$6.507x10^{-2}$
34.67%	650	$5.655x10^{-2}$
	800	$1.278x10^{-1}$
53.02%	650	$2.241x10^{-1}$
	800	$8.451x10^{-2}$

Tab. 8-1: SSQ for ReDrop simulations of iso-optical settling experiments, with the time step set to 0.02 s, number of height element and minimum number of drops per height element equal both to 150

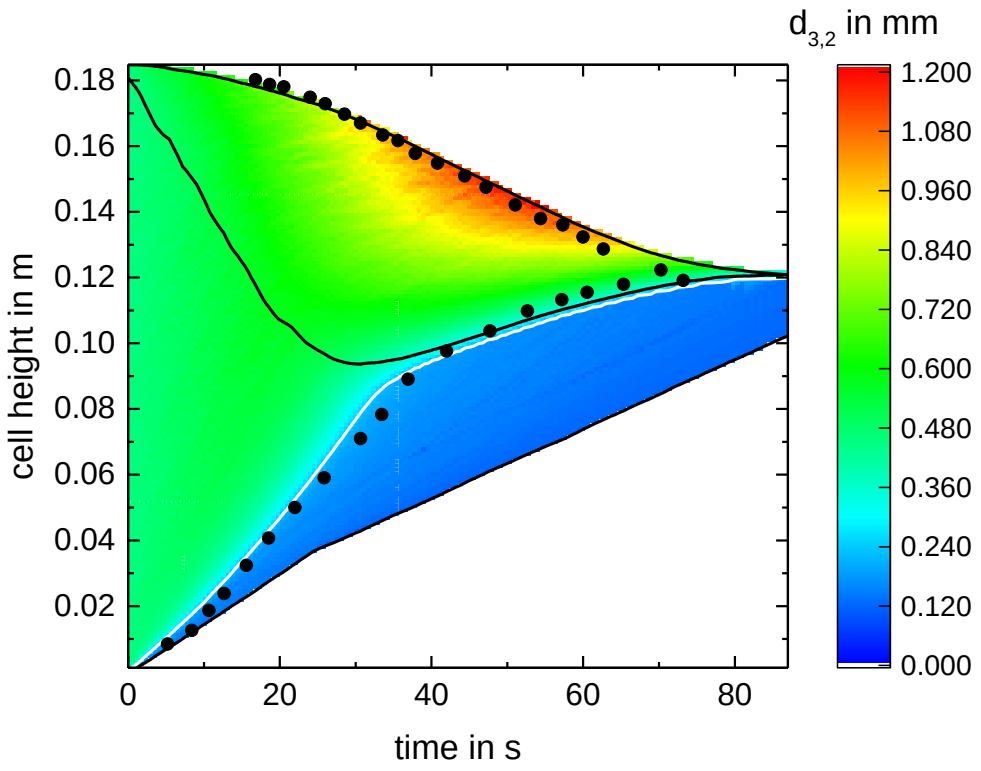

Fig. 8-3: Evolution of the drop size simulated for the settling of the iso-optical system for a phase fraction of 34.67% at mixing with 650 min^{-1}.

The sedimentation and coalescence curves obtained with ReDrop show excellent agreement with experimental measurements, displaying only minor deviations. The simulations are particularly striking for experiments conducted with mixing at 650 rpm, where the predicted profiles align almost with the observed data. These slight deviation may arise from the initial drop-size evaluation. Overall, the very good agreement between simulation and experiment demonstrate the robustness and the reliability of the chosen modeling framework.

ReDrop can now be applied also to elucidate certain phenomena, such as a lag time, which is frequently observed in technical systems. At the start of the settling experiments, with many systems a lag time is observed during which no sedimentation and coalescence is observed. After some time, the sedimentation and coalescence curves start. At the same time typically, a certain drop diameter is evaluated from the slope of the sedimentation curve, which is relatively independent from the intensity of stirring to produce the dispersion. With ReDrop it was possible to simulate the lag time if a system with a very small initial drop-size distribution is used, smaller than those measured in this study as shown in Fig. 8-4. During the lag time, these small drops, whose sedimentation is negligible, gradually coalesce until they reach a certain diameter at which significant sedimentation occurs. Since this diameter depends only on physical parameters like density difference between the phases and viscosity of the continuous phase, the slope of the sedimentation curve and hence the corresponding characteristic drop diameter remains essentially constant for a given material system, irrespective of the initial drop size. Lag time thus corresponds to the time the dispersion needs to form drops of the characteristic size by coalescence, at which size significant sedimentation starts. Variations in dispersing intensity and thus in the initial size distribution affect the duration of the lag time but have little impact on the characteristic diameter itself, which is the important parameter for settler scale-up. This characteristic diameter also corresponds to the drop diameter which would be evaluated by the Henschke model assuming mono-sized drops after shifting the characteristic curves by the lag time [5]. In the ReDrop simulations of the iso-optical settling experiments, the characteristic diameter ranged narrowly between 210 µm and 260 µm. This can be seen in Fig. 8-4, where the drop size during significant sedimentation, indicated by the blue color is quite comparable, around 200 µm in Fig. 8-4.

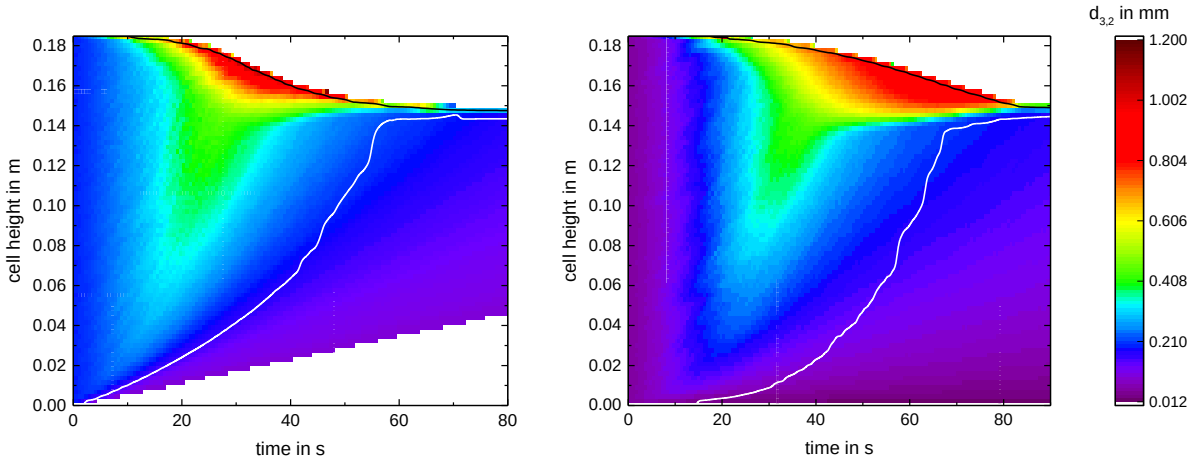

Fig. 8-4: ReDrop simulations with different initial droplet size distributions. The graph on the left shows a mean diameter of 0.18 mm with a variance of 0.03 mm; the graph on the right shows a mean diameter of 0.035 mm with a variance of 0.015 mm. The coalescence and collision parameters are set to 0.0150 and 806.03, respectively.

Another aspect of interpreting settling behavior can be clarified based on the polydisperse drop-based simulation with ReDrop. As discussed in chapter 4.2.2, it is generally assumed that drops after sedimenting relatively freely reach a close-packed zone, in which the drops are in continuous direct contact. However, both experimental observations and ReDrop simulations demonstrate that the close-packed zone occurs only within a very narrow region, as illustrated for the experimental data by the red dotted line in Fig. 8-5, showing that an hold-up above the close packed limit of 0.755 is hardly reached. This mean that drops are hardly in full contact. The experimental data show large region with a rather constant hold-up in the sedimentation zone, which correspond roughly to the initial hold up. Beyond a certain height, a jump in hold-up is observed to a value significantly below the close-packed limit. This point corresponds to the limit of the densely-packed zone. As the droplets settle, they eventually reach the densely-packed zone where their settling velocity is greatly slowed by the flow velocity of the continuous phase between the droplets. The fluid-dynamic equilibrium between the dispersed and continuous phases, as described by Wallis [73] and Pilhofer and Mewes [74], is illustrated in Fig. 8-6. The black curve shows the effective sedimentation velocity from the drop-sedimentation model against the hold-up, while the red horizontal line marks the superficial velocity at equal flow rates of both phases, $-v_c$ and v_d, which due the volume balance leads to be equal for both phases in a settling experiment. In the densely-packed zone, the flow rates of both phases is given by the second stable fluid-dynamic point, where droplet settling precisely balances the

continuous-phase flow. In this densely-packed zone, the drops thus freely sediment and get into contact only eventually corresponding to the local hold-up. The beginning of the densely-packed zone is represented in the graphs in Fig. 8-2 and in the annex 11.11 by a black curve, in-between the coalescence and the sedimentation curves, following a hold-up equal to 105% of its initial value. From this limit, the hold-up increases progressively with height, reaching maximum values of 75% in the simulations beyond which the drops are in continuous contact. This close-packed zone, which in previous description of the settling process has been assumed to develop directly above the sedimentation zone with essentially initial hold-up, was hardly formed during phase separation contrary to the assumptions made e.g. by Henschke [5]. In the literature the densely-packed zone has thus previously been mistakenly attributed to be the close-packed layer [47, 87].

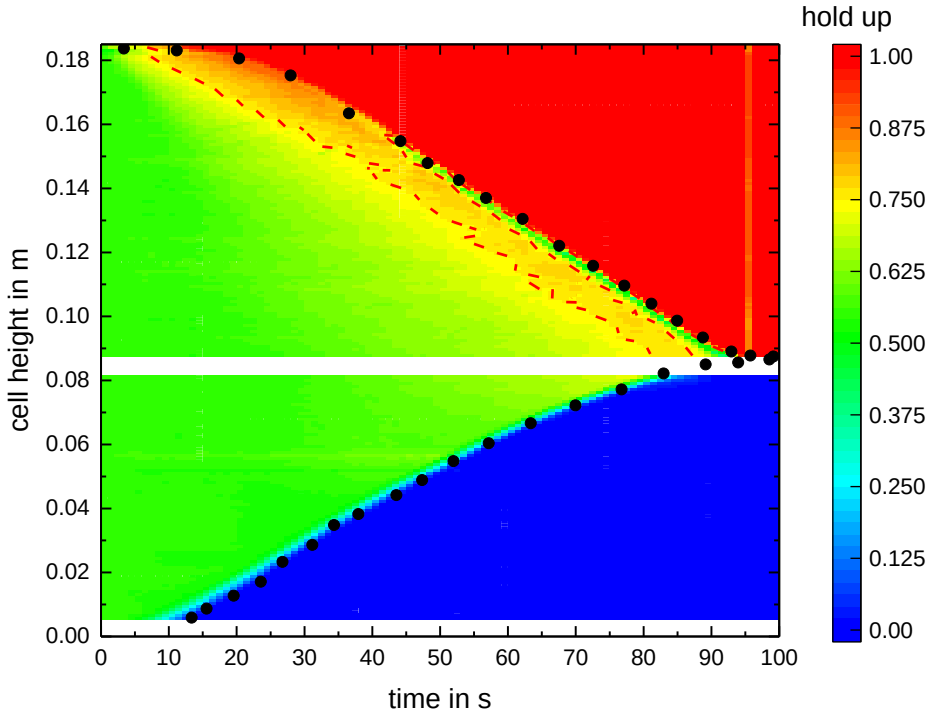

Fig. 8-5: Experimental data of the settling of the iso-optical system for an initial holdup of organic phase of 53.02% at mixing with 800 min^{-1}.

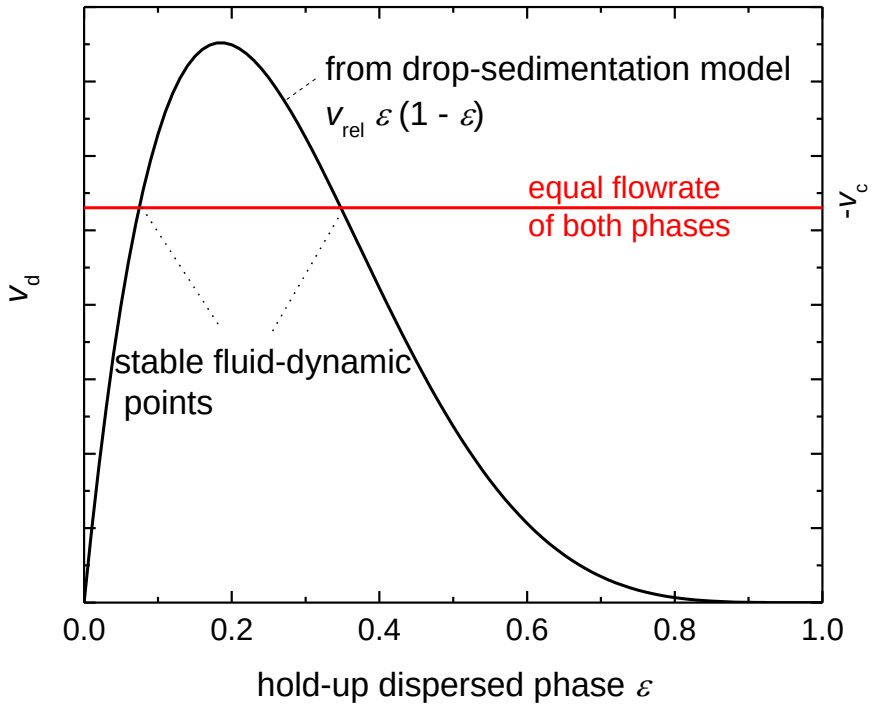

Fig. 8-6: Wallis plot for typical settling of liquid-liquid dispersion

The ReDrop simulations have made it possible to predict the settling of liquid-liquid dispersions quite accurately, while at the same time validating the various models and their hypotheses. This makes it possible to understand, at a fundamental level, the interactions that drops may have with each other during their settling. The polydisperse simulations with ReDrop thus provide fundamental insights into the phenomena observed experimentally for the design of technical settlers. This allows to explain phenomena observed for technical systems, such as the lag time and the observation of a characteristic drop diameter that is essentially independent of the stirring intensity. It also allows to eliminate misconceptions about general aspects of settling such as the introduction of the densely packed zone. This shows that the ReDrop simulations developed here give an accurate and consistent picture of the settling process. Taking these new observations into account, the depiction of liquid–liquid separation shown in Fig. 1-1 is therefore slightly revised, as illustrated in Fig. 8-7.

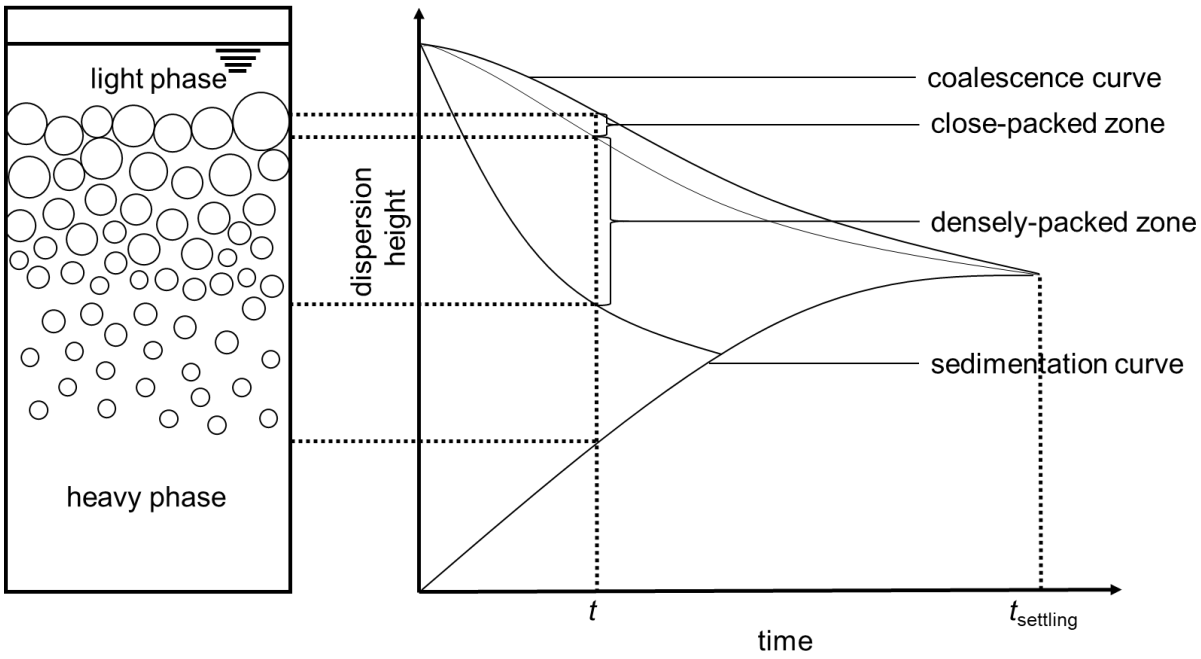

Fig. 8-7: Evolution of the settling of a liquid-liquid dispersion after Henschke in light of new insights [16]

9 Effect of Ions on Drop Coalescence

Trace components such as salts strongly influence droplet interactions and thus their coalescence. The salt effect varies with the ion species and concentration making settling times quite unpredictable and, thus, the design of technical equipment challenging [15, 27, 34, 45]. To overcome this challenge, settling experiments are usually conducted in a so-called settling cell to quantify the effect of the trace components present in any specific system [15]. In more detail, Kopriwa [27] showed that trace components like salts have a strong influence on the coalescence time, because they influence the interaction between the interfaces. Pfennig and Schwerin [34, 44, 45] showed by testing different systems with varied salt concentrations that the salt effect on coalescence time can in principle be linked to the Derjaguin-Landau-Verwey-Overbeek (DLVO) theory [35, 36]. The DLVO theory describes the force resulting from the repulsive electrostatic interaction and the attractive Van-der-Waals force acting between two approaching droplets. The DLVO force, which is determined by the electrostatic potential difference $\Delta\varphi$, depends on the salt concentration and on the different ions present in the system [27]. As shown on the right side of Fig. 9-1, the DLVO force typically shows a repulsive maximum for a given salt concentration. At this value, the repulsive force between two drops is large and, as a consequence, hinders the coalescence, and thus increases the settling time, as shown on the left side of the Fig. 9-1 [34].

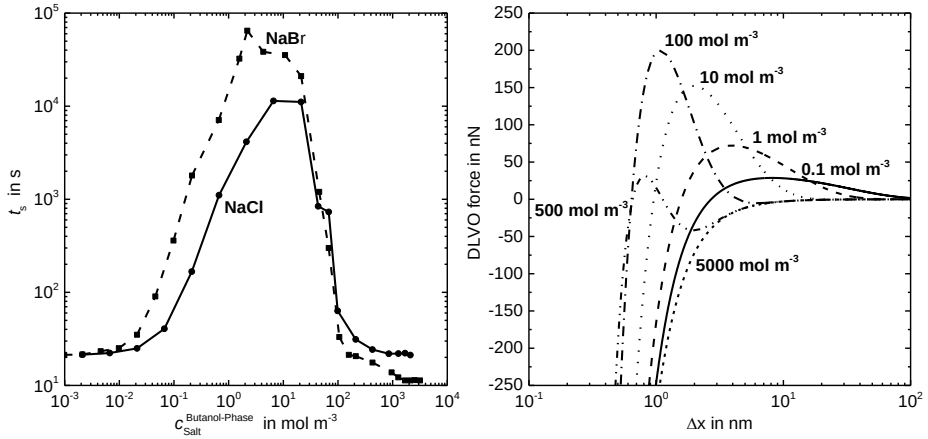

Fig. 9-1: Evolution of the settling time on the left side and of the qualitative DLVO force on the right side with the salt concentration between two drops of 0.1mm with an electrostatic potential difference of 90 mV [34].

The goal of this chapter is to further increase the level of detail in coalescence modelling, developed in chapter 3 by include the DLVO force in the driving-force expression of the coalescence process.

9.1 State of Art

Coalescence models have also been described by a variety of authors in recent, rather detailed reviews of coalescence modelling [2, 27, 47]. Some of these coalescence models explicitly account for electrolyte effects. Tobin and Ramkrishna [48] develop a detailed model for drop coalescence, which similar to the approach of chapter 3, takes the individual steps of coalescence into account. The energy to overcome electrostatic repulsion is included, but in the experimental validation, the relevant parameter is fitted and not linked to an independent quantification of $\Delta\varphi$. Kamp and Kraume [36] propose a model, where the electrostatic effect is accounted for empirically with an additional factor for the coalescence probability, which is described with the model of Coulaloglou and Tavlarides [14]. The electrostatic contribution is formulated empirically as a Boltzmann factor, where the denominator, which would correspond to the available energy in the physical interpretation, is only the van-der-Waals attraction. A physical picture for this assumption is not given. In the experimental validation, zeta-potential measurements have been used, which do not characterize the true potential at the interface but at the shear plane. It should be stated that the ad-hoc model of Coulaloglou and Tavlarides [14] does not take fundamental boundary conditions into account as explained in chapter 3.4. As a consequence, many of the coalescence models proposed in the literature, which are based on that approach, contain an inconsistency. Melis et al. [49] propose a detailed model for interaction of solid particles in solution, where they avoid determination of potential difference by a specific formulation for a Stern layer. The surface charge density has then been fitted to experimental data via the Langmuir adsorption constant of an ionic surfactant. No independent measurements on characterizing $\Delta\varphi$ have been performed.

Also, molecular simulations have been conducted to interpret the effect of electrostatic effect by Marčelja [50], who evaluates with certain simplifying assumptions the spatially resolved potential function.

Finally, measurements with atomic force microscopy should be mentioned, performed in the group of Stevens [51], where also electrostatic repulsion is used to interpret the forces found.

This shows that the repulsive electrostatic force as described e.g. by the DLVO theory is generally considered as an essential variable in characterizing coalescence time. The unknown variable in the DLVO theory is the electrostatic potential difference between the phases, $\Delta\varphi$. Unfortunately, this variable cannot be measured experimentally at the present time [34, 46]. The goal of this chapter is thus as a first step to elucidate the relation between the electrostatic potential difference and the experimental settling behavior.

The first part of this chapter presents the Albertsson model that describes the ion behavior in two-phases systems. Then details on the method used to gain quantitative and unequivocal information on the electrostatic potential difference relative to that of a reference system are presented in chapter 9.2. The setup and experimental procedure for the settling experiments, similar to the setup used by Pfennig and Schwerin [34], are described in chapter 9.3. Finally, in chapter 9.4, settling data are compared to electrostatic-potential measurements.

9.2 Theory: Partition Coefficient and Electrostatic Potential Difference

9.2.1 Albertsson Model

The theory presented here follows previous work [34]. Ions contained in two-phases systems can in principle partition between the phases. The corresponding partition coefficient of the electrolytes, K_i, depends on the affinity of each ion for both phases in conjunction with the electroneutrality condition that holds for each phase. The partition of the charged species induces an electrostatic potential difference between the phases. Albertsson developed the following relation between the potential difference between the phases and the hypothetical partition coefficient of each ionic species, if it were unchanged, K_i^0 [34]:

$$\ln K_i = \ln K_i^0 - \frac{z_i F}{RT}\Delta\varphi \quad . \tag{9-1}$$

where z is the ionic charge of the species *i*, *R* is the universal gas constant, *T* the temperature and *F* is the Faraday constant. Eq. 9-1 is valid for each ionic species present in the system.

In the case of an individual salt in solution, dissociating in aqueous solution into the cation A^{z_A} and the anion B^{z_B}, electroneutrality leads to:

$$\ln K_A = \ln K_B \quad . \tag{9-2}$$

Combining Eq. 9-1 and Eq. 9-2 yields

$$\Delta\varphi = \frac{RT}{(z_B - z_A)F} \ln\left(\frac{K_B^0}{K_A^0}\right) \quad , \tag{9-3}$$

which shows that the electrostatic potential is independent of the concentrations of the ions.

In the case of more ionic species being present in the solution, Eq. 9-2 can be replaced by [34]:

$$0 = \sum_{i=1}^{N_{ion}} \frac{c_i z_i}{1 + \alpha K_i} \quad . \tag{9-4}$$

where c_i is the molar concentration of each ion and α is the volumetric phase ratio of the two phases. The resulting extended Albertsson model is described in detail by Pfennig and Schwerin [34].

To demonstrate the behavior of a real system, which does not only consist of a pure solvent but also an ionic impurity to which a dedicated salt is added, this extended Albertsson model can be applied. The result, together with the values of the various variables used in the example shown are presented in Fig. 9-2. The two different salts jointly determine the electrostatic potential difference. At small salt concentration, the impurity is the major compound present in solution, which thus defines the electrostatic potential difference and thus the partition of all ionic species that have a lower concentration according to Eq. 9-2. Then, from a concentration of approximately 10 to 20 mmol L^{-1} in typical real systems, the added salt is in excess and thus determines the potential difference, i.e. a second plateau is reached. The plateau is characteristic of the dedicated salt added to the system. In the region, where one electrolyte in excess defines the electrostatic potential difference, its ions essentially ensure electroneutrality and the ions of the other electrolyte partition in that potential difference. Above a certain concentration, usually around 50 to 100 mmol L^{-1} depending on the salt stoichiometry, the Albertsson model is not valid anymore, and the curve deviates from the plateau. Indeed, above this concentration, the electrolyte cannot be regarded as infinitely diluted anymore and the K^0 of the ionic species present in solution start to be influenced by the salt. In between where none of

the two electrolytes is in clear excess, a transition region occurs as shown exemplarily in Fig. 9-2.

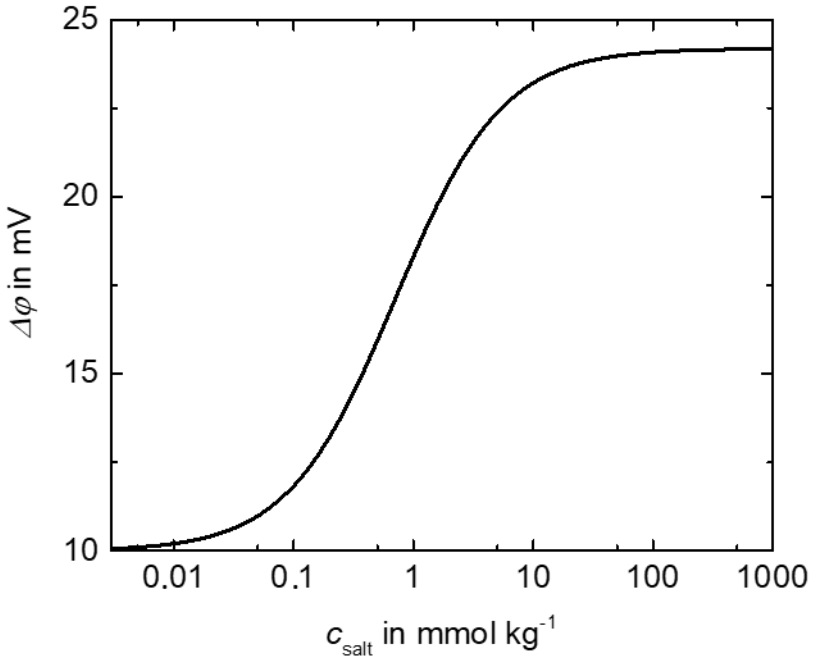

Fig. 9-2: Schematic evolution of the electrostatic potential difference with the salt concentration ($K^0_{cation} = 1.5 \times 10^{-4}$, $K^0_{anion} = 4.5 \times 10^{-5}$, $K^0_{impurities^-} = 6.42 \times 10^5$, $K^0_{impurities^+} = 2.20 \times 10^5$, $c_{impurities} = 4.3 \times 10^{-3}$ mmol L^{-1})

9.2.2 Determining the Relative Electrostatic Potential Differences

The electrostatic potential difference cannot be measured as mentioned above, because a two-phase system constitutes a half cell, for which such measurement is not possible by electrodes in principle. However, an interesting option is to measure the difference of the potential difference i.e. to measure $\Delta\varphi$ of a system relative to that of a reference system by dye partition. This corresponds to measuring the potential of two joined half-cells, where it has been shown previously that this is identical to the potential difference obtained with electrodes in e.g. the bottom phases, if the top phases of two two-phase systems are linked with a salt bridge [34].

Two systems thus have to be compared with different salts added, one of them typically being taken as the reference, e.g. with NaCl. Both systems are produced with the same solvents

coming with their own ionic impurities. The concentration of the added salts is then varied in both systems. A dye is added to the systems, which fully dissociates into ionic species, so that the partition coefficient of the charged dye can be used as indicator for potential differences. The dye is added in so small quantity that it is not affecting the electrostatic potential difference in the system, especially in the range where that is determined by the added dedicated salts. The dedicated salt, which is then in excess compared to the charged dye, thus fixes the electrostatic potential difference between the two phases and thus also the partition coefficient of the dye. Typically, the dye concentration is chosen to be at least 100 times lower than the salt concentration [34]. The measurement of the charged dye partition by spectrophotometry is then directly evaluated with the extended Albertsson model for the two systems containing the different salts, one being the reference system:

$$\ln K_{\mathrm{dye,ref}} = \ln K^{0}_{\mathrm{dye}} - \frac{z_{\mathrm{dye}}F}{RT}\Delta\varphi_{\mathrm{ref}} \quad . \tag{9-5}$$

$$\ln K_{\mathrm{dye,salt}} = \ln K^{0}_{\mathrm{dye}} - \frac{z_{\mathrm{dye}}F}{RT}\Delta\varphi_{\mathrm{salt}} \quad . \tag{9-6}$$

Combining these two partition coefficients, the follow can be obtained:

$$\frac{z_{\mathrm{dye}}F}{RT}\left(\Delta\varphi_{\mathrm{ref}} - \Delta\varphi_{\mathrm{salt}}\right) = \left(\ln K^{0}_{\mathrm{dye}} - \ln K_{\mathrm{dye,ref}}\right) - \left(\ln K^{0}_{\mathrm{dye}} - \ln K_{\mathrm{dye,salt}}\right) \quad . \tag{9-7}$$

At salt concentrations that are sufficiently below the above-mentioned 50 to 100 mmol/L, the K^{0}_{dye} are not influence by the salts, i.e. the K^{0}_{dye} cancel. Eq. 9-7 can then be solved for $\Delta\Delta\varphi_{\mathrm{salt}}$:

$$\Delta\Delta\varphi_{\mathrm{salt}} = \left(\Delta\varphi_{\mathrm{ref}} - \Delta\varphi_{\mathrm{salt}}\right) = -\frac{RT}{z_{\mathrm{dye}}F}\left(\ln K_{\mathrm{dye,ref}} - \ln K_{\mathrm{dye,salt}}\right) \quad . \tag{9-8}$$

The evaluation of electrostatic potential difference with respect to a reference system consists of measuring the partition coefficient of the dye in the two-phase system while varying the concentration of the salt. This method is repeated with different salts, one of which is taken as the reference for the evaluation of the $\Delta\Delta\varphi_{\mathrm{salt}}$, for which here NaCl is chosen.

It should be stressed that the evaluated potential differences are those exactly at the interface, because it is there where the ionic species 'decide' how to partition between the phases. To

determine $\Delta\Delta\varphi_{salt}$, settling experiment with the same systems are performed in order to obtain the settling and coalescence curves characteristic to each individual system.

9.3 Experimental Procedure and Materials

9.3.1 Chemicals

Partition-coefficient experiments and settling tests are realized with a two-phase system prepared from deionized water and cyclohexanone (VWR, lot:19J164001). Four different salts are added individually to the system: sodium chloride (acros, lot: A0381628), ammonium chloride (Roth, lot: 379284741), magnesium sulfate (VWR, lot: 02G080026) and sodium nitrate (UCB, lot: 91063171). These salts have been chosen in this first validating study such that they differ significantly in their behavior e.g. expressed via their position in the Hofmeister series. All the used salts have a purity higher than or equal to 99.5%. The dye used for the partition coefficient experiments is methyl orange. The dye is only added in the partition experiments to characterize the potential differences. Since the dye can in principle act as a surfactant, which could influence coalescence, the dye is not added in the settling experiments.

9.3.2 Experimental Procedure for Partition-Coefficient Evaluation

The systems used for the partition-coefficient evaluation are prepared by weighting 20 ml of each phase into a 50 ml Duran bottle, closed with a screw cap.

The stock solutions of salt-containing water with the dye are prepared by weight in advance. The dye concentration in the initial aqueous phase is of 1.9 mg L^{-1}, which corresponds to 5.80×10^{-6} mol L^{-1}, which is significantly below the impurity concentration. For each salt, different concentrations are used. The prepared two-phase systems are then placed in an agitated thermostatic bath (GFL model 1083) to reach an equilibrium temperature of 25°C. It should be noted that according to Kopriwa [2, 27], the added salts in the concentration range chosen for this study are not measurably affecting the solvent solubility or physical properties of the phases.

After 2 hours, the temperature and concentration equilibrium is reached. Then, roughly 10 ml of each phase is collected with a pipette. To avoid occurrence of a second phase during

analysis, 0.5 g of the pure deionized water and cyclohexanone are added, respectively, to the collected phases. The dye concentrations in each phase are evaluated by UV-Vis spectrophotometry (Hach model DR3900).

Absorbance of solutions of water containing the methyl orange at different known concentrations was quantified with the spectrophotometer to produce a calibration curve. The absorbance is evaluated at the maximum of the absorbance spectrum relative to a baseline value. The locations of the peak and the baseline differ between the phases. They are located at 463 nm and 344 nm for the aqueous phase and at 421 nm and 361 nm for the organic phase, as shown in Fig. 9-3. The shape of the UV-Vis spectrum and the location of the absorbance peak are in good agreement with that of a fully dissociated methyl orange according to a literature study [52]. Also, the pKa of methyl orange is 3.39, which suggests that the dye is fully dissociated in the two-phase systems investigated.

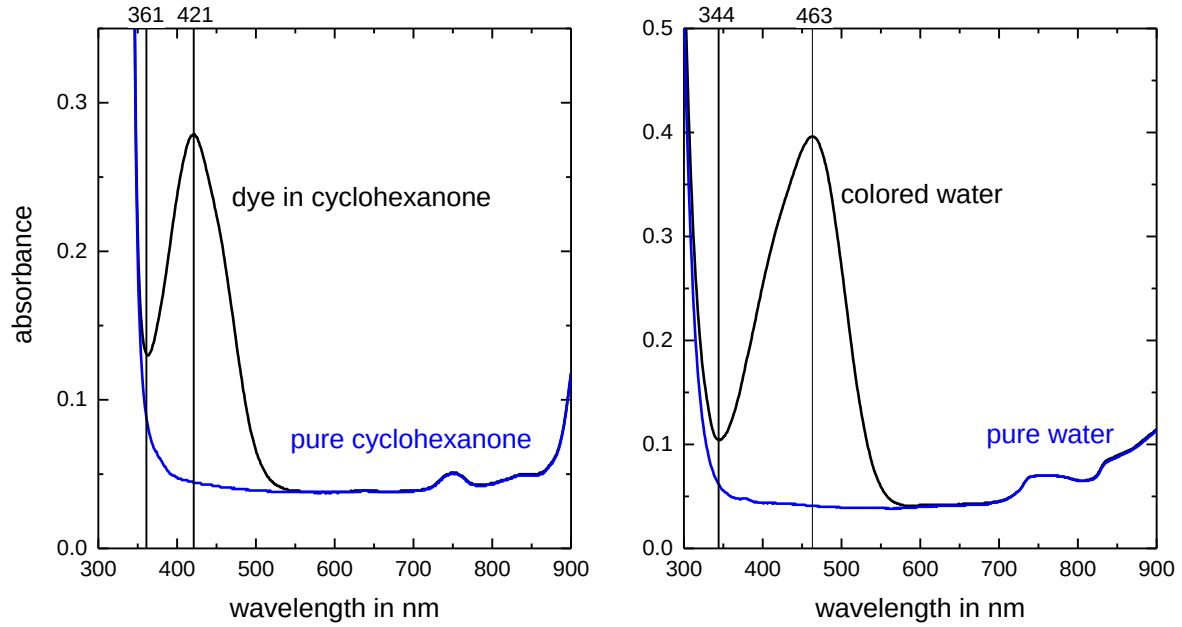

Fig. 9-3: Absorbance spectra of cyclohexanone (left) and water (right) with and without methyl orange

Additional measurement showed that the effect of solvent saturation and of the presence of salts do not affect the measurement of the dye concentration as shown in Fig. 9-4. This was demonstrated by generating each saturated phase individually. To this end, stock solutions of salt-containing water and deionized water were saturated with cyclohexanone and cyclohexanone was saturated with deionized water. A known quantity of dye was added to each

saturated phase. The absorbance of the dye in each different solution was plotted together with the calibration curve, where these data fell on top of the previously determined calibration curves as shown in Fig. 9-4.

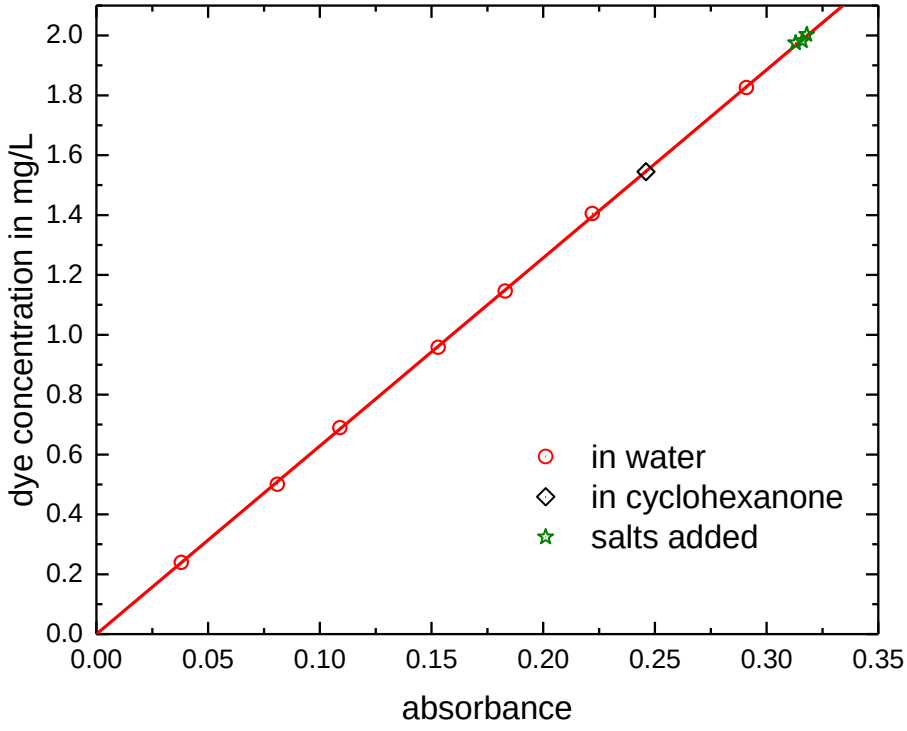

Fig. 9-4: Calibration curve for the dye partition coefficient experiment.

9.3.3 Experimental Set Up of the Settling Tests

Batch settling experiments in a standardized settling cell have been performed to evaluate the effect of the salt on the coalescence behavior. The stirring cell and the experimental procedure are described in chapter 6.1.1

The dispersion is generated by stirring for 30 s at 800 min^{-1}. The settling cell is connected to a thermostatic bath (VWR model AP15R-40-V12V) to ensure a working temperature of 25°C.

For the settling experiments, two volumetric phase ratios organic to aqueous phase are chosen, 1/2 and 2/1, which lead to different direction of dispersion. Each salt for the partition coefficient experiments is used for each phase ratio. The salt concentrations are fixed to 20 mmol L^{-1}. Stock solutions of salt-containing water are prepared beforehand. The cell is filled

with the two phases successively. After 2 hours with intermittent stirring, when the temperature and concentration equilibration is reached, the settling experiments have been performed.

9.4 Results and Discussion

9.4.1 Partition Coefficient Experiments

The results of the partition-coefficient experiments are shown in Fig. 9-5. The partition coefficient of the charged dye, measured for several salt concentrations, is represented in the graph by the individual points. Several experiments are repeated for validation purposes. The Eqs. 9-1 and 9-4 are then used to fit the model parameters of the extended Albertsson model, $\Delta\varphi$, $c_{\text{impurities}}$ and the K_i^{o}, to the experimental data. This model, which is represented by the curves in Fig. 9-5, apparently ensures a good correlation of the experimental data. For small values of the salt concentrations, the curves converge to the same value. At low salt concentrations, the impurities of the underlying two-phase system itself fix the potential difference and thus the behavior of the ions present in the systems. For an increasing salt concentration, the curves diverge to reach their plateau after 10 to 20 mmol kg^{-1}. In that concentration range the added salts determine the potential difference and thus the dye partition. Beyond a concentration of between 50 and 100 mmol kg^{-1} the partition coefficient of the dye starts to diverge. Since it is ionic strength, which is actually relevant for the behavior of the electrolyte-containing system, the onset of divergence is earlier for salts with divalent ions. Since these data are not only influenced by the electrostatic potential difference but also by variation of the underlying two-phase system, the values above 10 mmol kg^{-1} for $MgSO_4$ have been excluded from the fit with the extended Albertsson model. For the other salt, the limit is set to 100 mmol kg^{-1}. The impurities concentration is evaluated to 4.3 10^{-3} mmol kg^{-1}.

The evolution of the electrostatic potential difference relative to that with sodium chloride as obtained from the fit with the extended Albertsson model given by Eq. 9-8 is shown in Fig. 9-6. Tab. 9-1 indicates the values of $\Delta\Delta\varphi_{\text{salt}}$ when the salt concentration reaches the plateau. The evaluated Sodium nitrate and the magnesium sulfate have a similar electrostatic potential difference. However, their ionic charges are 1 and 2, respectively. The difference in electrostatic potential difference between the sodium nitrate and the ammonium sulfate is around 50 mV, which has the same order of magnitude observed by Pfennig and Schwerin for the two-phase system of butanol and water [45].

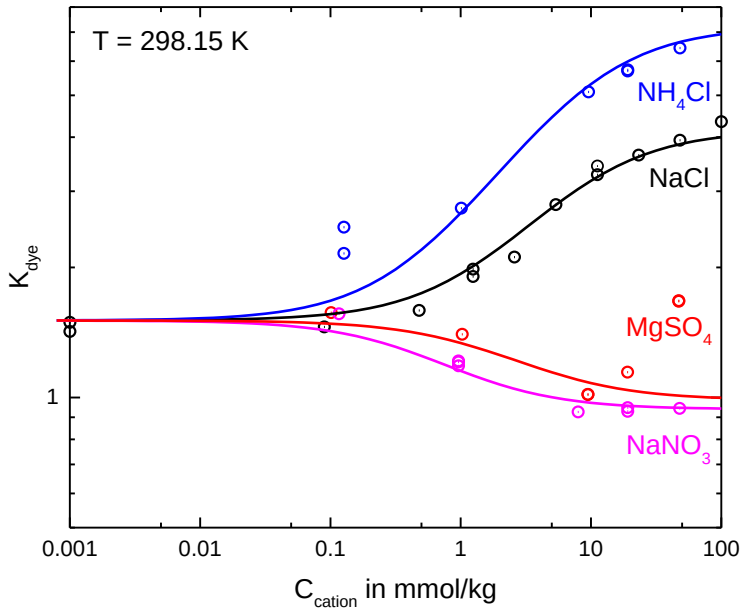

Fig. 9-5: Evolution of the partition coefficient of the dye with the salt concentration. The solid line represents the fitted extended Albertsson model.

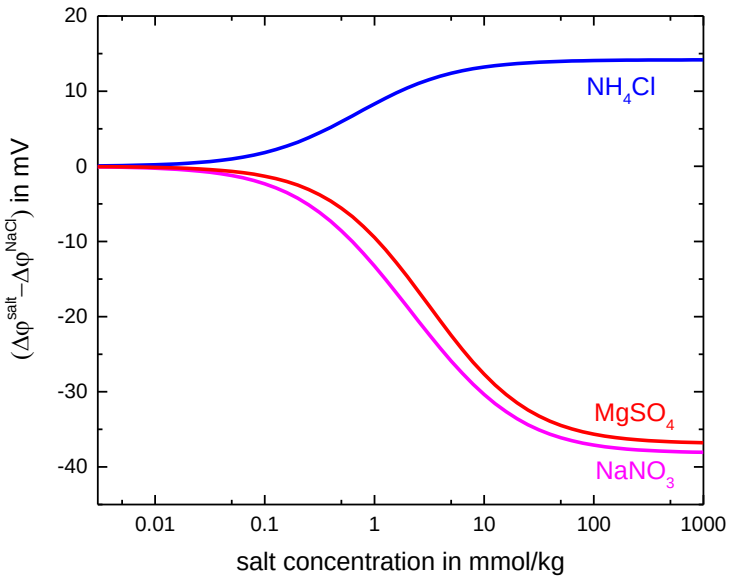

Fig. 9-6: $\Delta\Delta\varphi$ as evaluated from dye partition with the Eq. 9-8 of the extended Albertsson model for different salts using sodium chloride as reference.

salt	$\Delta\Delta\varphi_{salt}$ in mV
$NaNO_3$	-38.60
$MgSO_4$	-37.35
NH_4Cl	13.80

Tab. 9-1: $\Delta\Delta\varphi$ values corresponding to the plateau.

9.4.2 Relation Between the Relative Electrostatic Potential with the Settling Behavior

The results of the settling experiments are shown in Fig. 9-7 and Fig. 9-8 for the organic to aqueous phase ratios 2/1 and 1/2 versus the relative electrostatic potential as obtained above. The initial drop size and the settling time have an opposite tendency, as expected. For a situation, where due to a shift in electrostatic potential difference coalescence is hindered more strongly, it is expected that the initial drop size is smaller and the overall settling takes longer. The initial drop-size distribution of sodium nitrate could not be determined, because its drop size is too small to be measured accurately with the SOPAT probe used during the settling experiment.

The variation in settling time between the monovalent salts NH_4Cl, NaCl, and $NaNO_3$ shows nicely a systematic influence of the salts having identical stoichiometry. At the same time, the systematic and strong variation in settling times also nicely demonstrates the strong influence of the electrostatic potential difference on coalescence.

On the other hand, for both phase ratios the behavior with sodium nitrate and magnesium sulfate significantly differs, even though they have a similar electrostatic potential difference. This can in principle be explained by the differently charged ions. According to the DLVO theory, the charge number has an influence of the electrostatic force acting between the drops. In Fig. 9-9 the maximum of the DLVO force is plotted against the absolute electrostatic potential for cation charge numbers of 1 and 2. Other variables of the DLVO theory are set to typical values. Similarly, the range of the repulsive forces depends on cation charge, because this is actually determined by Debye length, which in turn is defined based on ionic strength. As shown in Fig. 9-9, the maximum DLVO force between drops for 1:1 salts differs systematically from those for divalent salts. This may explain the relative effect of $NaNO_3$ and $MgSO_4$ on settling. This ad hoc explanation needs to be validated by further investigations including more divalent salts.

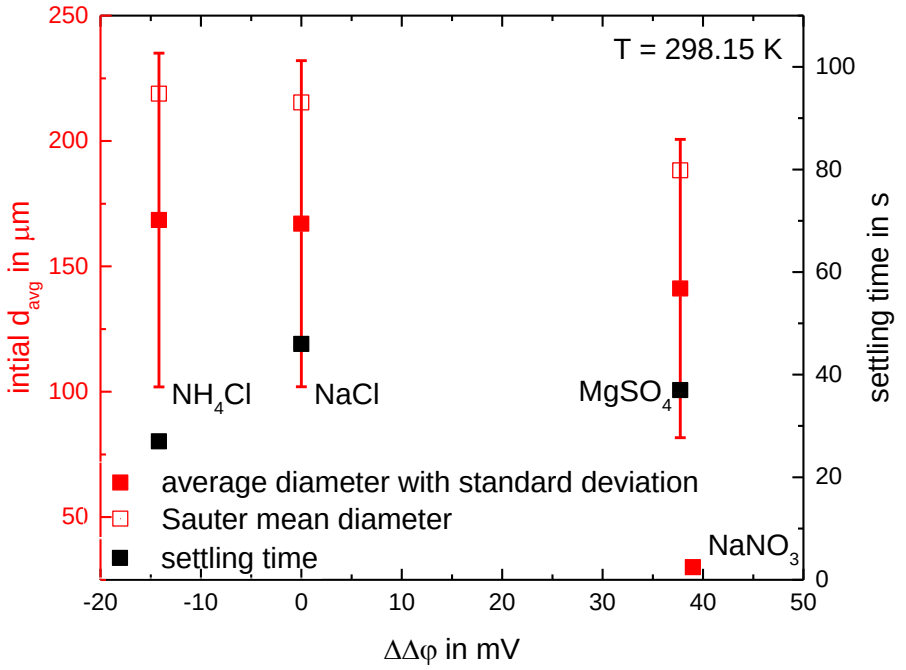

Fig. 9-7: Settling experiments performed at organic to aqueous phase ratio 2/1 with different salts added. Initial drop size (squares) and settling time (triangles) are presented versus $\Delta\Delta\varphi$ as obtained as described above.

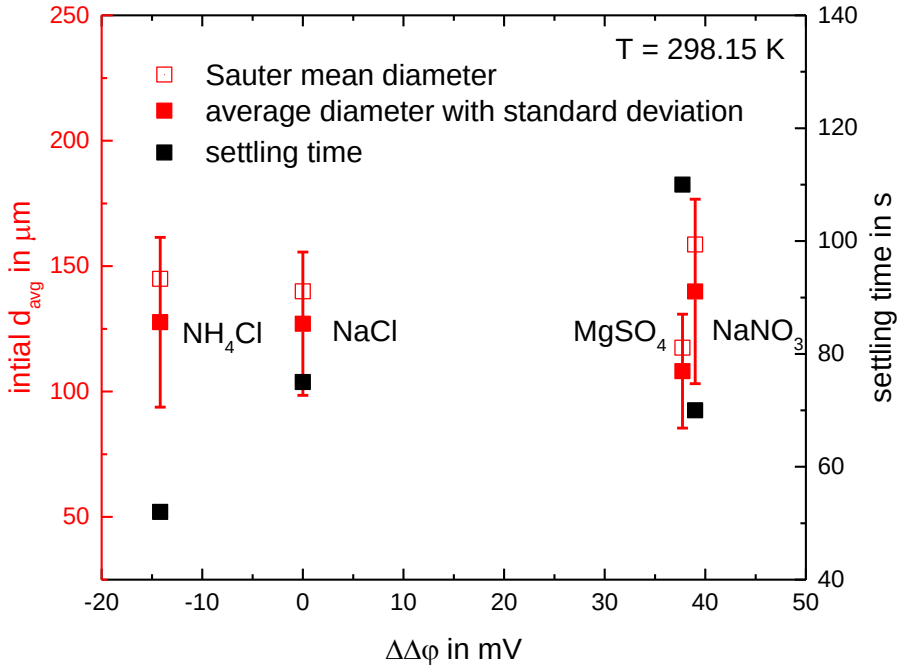

Fig. 9-8: Settling experiments performed at organic to aqueous phase ratio 1/2 with different salts added. Nomenclature is identical to that in Fig. 9-7.

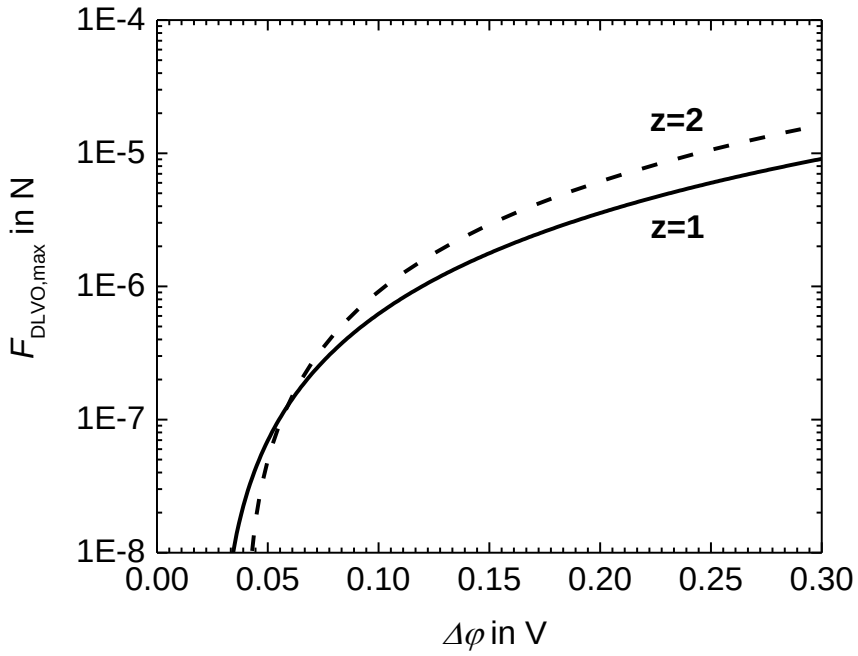

Fig. 9-9: Maximum value of the DLVO force with the absolute electrostatic potential for cation charge numbers of 1 and 2 for 1 mm drops.

9.5 Conclusion

Utilizing a charged dye dissolved in salt-containing two-phases system allows the accurate and unequivocal determination of the relative electrostatic potential differences between the phases.

Based on the first settling experiments done in the present work, the relative electrostatic potential difference and the charge number have a significant influence on coalescence and thus on the settling behavior. The relative electrostatic potential difference should thus be included in the detailed coalescence modelling in order to quantify the effect of the electrostatic force on settling.

Also, these settling experiments are a good first basis to quantify the implications of the DLVO force on coalescence. In future work the detailed analysis of the characteristic curves of the settling experiments will be evaluated with the help of a ReDrop (Representative Drop) simulation tool to elucidate this influence and to derive a corresponding validated model.

10 Conclusion

In this thesis, the coalescence and sedimentation phenomena governing the settling of liquid–liquid dispersions are investigated, with the ultimate goal of predicting the settling of technical systems.

A novel coalescence probability model has been developed, differing from the classic formulation of Coulaloglou and Tavlarides [14]. The empirical exponential function linking contact time to coalescence time was replaced by a physically coherent expression. While the coalescence-time expression is based on Henschke's approach, which assumes the formation of an asymmetric dimple between approaching droplets, it has been further developed here to account for the specific geometric configuration of the droplets. Coalescence time is influenced by two parameters. The first is the coalescence parameter, r_s^*, which is system-specific and must be fitted for each individual material system. It is assumed to be independent of holdup but dependent on the direction of dispersion. The second parameter affecting the coalescence time is the collision parameter, $C_{\text{coll,buoyancy}}$, which is assumed to be generalizable across all material systems. This new formulation of the coalescence time provides more realistic descriptions of coalescence events.

Sedimentation modelling was adapted to accommodate a wide range of droplet concentrations by incorporating a swarm-effect correction similar to that used by Richardson and Zaki, alongside a porous-media permeability framework based on Darcy's law. This model can capture both hindered settling at moderate drop volume fractions and settling at high drop concentrations.

Both the coalescence and sedimentation models were implemented in a simulation tool based on the ReDrop approach, enabling predictions of dispersion separation. To validate the ReDrop program and its underlying mathematical models, a series of settling experiments was conducted. For this purpose, a dedicated experimental apparatus was designed and constructed based on a comparative study of existing equipment. The two-phase system selected for validation was an iso-optical system in which a trace dye was introduced into one phase to enable the concentration profiles of the droplets to be tracked in high resolution over time and along the dispersion height. The experimental equipment also enabled the initial

droplet size distribution to be measured, which is essential for providing relevant ReDrop simulations.

ReDrop simulations accurately predict the settling of liquid-liquid dispersions while validating the underlying models and assumptions. They offer fundamental insights into droplet interactions and help explain large-scale phenomena, such as lag time and the emergence of a characteristic droplet size independent of stirring intensity. The simulations also challenge common misconceptions, like introducing the concept of a densely packed zone, providing a coherent and realistic view of the settling process.

Finally, the influence of ionic strength on droplet coalescence was explored through measurements of electrostatic potentials relative to a reference system. These preliminary results pave the way for incorporating DLVO theory into the coalescence model, moving toward a truly predictive framework in which ion effects are captured mechanistically rather than via empirical fitting parameters.

Ultimately, by delivering a coherent, experimentally validated predictive tool to simulate settling of liquid–liquid dispersion, the initial goal of this thesis is achieved by providing a new consistent picture of the settling process that includes both the lag time mechanism and the formation of a densely-packed zone.

11 Appendix

11.1 Derivation of the Collision Probability Expression

The probability of collision between two representative drops must be evaluated since their horizontal position is not known. As shown in Fig. 11-1, the collision is characterized by an inner cylinder in which the two considered drops can meet. The probability of collision is expressed by:

$$p_{\text{coll}} = \frac{A_{\text{coll}}}{A_{\text{repr}}}, \tag{11-1}$$

where, A_{coll} is the lower surface of the collision cylinder, characterized by the diameter Δx:

$$A_{coll} = \pi\left(\frac{\Delta x}{2}\right)^2 \tag{11-2}$$

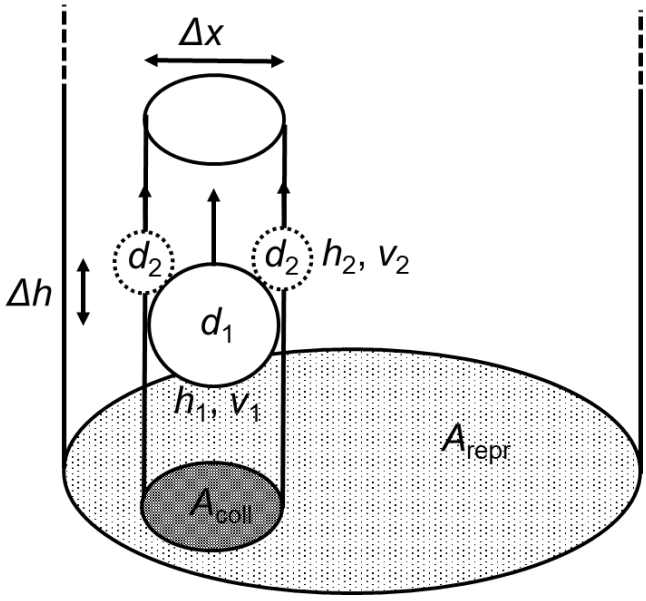

Fig. 11-1: Representation of the collision cylinder in which two drops can meet

This area depends on the height difference between the two drops, Δh, which is known in the simulations, if the height of the drops is included in the simulation.

The diameter of the collision cylinder can be expressed in terms of the diameters and heights of the drops using the Pythagorean theorem as shown in Fig. 11-2:

$$\frac{\Delta x^2}{4} + \Delta h^2 = \frac{(d_1 + d_2)^2}{4} \quad . \tag{11-3}$$

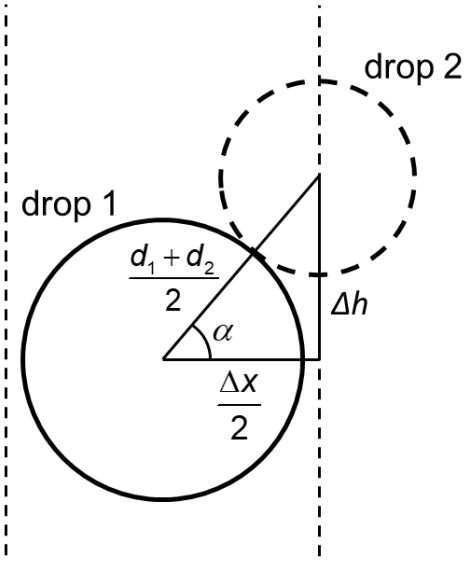

Fig. 11-2: Cross-section of two drops colliding

The collision cylinder therefore has a diameter of:

$$\Delta x = 2\sqrt{\frac{(d_1+d_2)^2}{4} - \Delta h^2} \quad . \tag{11-4}$$

The area of the collision cylinder is then:

$$A_{coll} = \pi\left(\frac{(d_1+d_2)^2}{4} - \Delta h^2\right) \quad . \tag{11-5}$$

The Eqs. 11-1 and 11-5 leads to:

$$p_{coll} = \frac{\pi\left((d_1+d_2)^2 - 4\left(h_1-h_2\right)^2\right)}{4A_{repr}} \quad . \tag{11-6}$$

Depending on the height difference, the collision probability has a minimum value of 0 when the drops are on top of each other and a maximum value of:

$$p_{coll,\max} = \frac{\pi(d_1+d_2)^2}{4A_{repr}} \quad , \tag{11-7}$$

when the drops are at the same height.

The averaging of the collision probability along the height can be realized, total collisions are considered in the simulation. Eq.11-6 is integrated between the boundary positions where the drops are in contact:

$$p_{coll,average} = \frac{\int_{-\frac{d_1+d_2}{2}}^{\frac{d_1+d_2}{2}} d\Delta h \frac{\pi\left((d_1+d_2)^2 - 4\Delta h^2\right)}{4A_{repr}}}{\int_{-\frac{d_1+d_2}{2}}^{\frac{d_1+d_2}{2}} d\Delta h} \quad . \tag{11-8}$$

The integral gives:

$$p_{coll,average} = \frac{\pi(d_1+d_2)^2}{6A_{repr}} \quad . \tag{11-9}$$

11.2 Derivation of the Critical Velocity Defining the Bouncing

A collision between two drops can lead to bouncing if their relative velocity exceeds the critical velocity, $v_{critical}$. Kamp [8] and Lehr and Mewes [12] suggest that the probability of bouncing can be approximated by a step function:

$$p_{bouncing} = \begin{cases} 1 \text{ if } v_{relative} \le v_{critical} \\ 0 \text{ otherwise} \end{cases} \quad . \tag{11-10}$$

In this appendix, the derivation in this appendix determines the critical velocity of the Kamp experiment [8]: the specific case of a moving drop hitting a stationary drop is considered. This provides a basis for further analysis of the impact velocity of two moving drops.

Before the collision, the moving drop has a non-zero velocity, v_0. The inertial force is balanced by the buoyancy and the drag force, creeping flow is assumed. When the drops collide, they are squeezed together and deformed. The velocity of the moving drop decreases: the Young-Laplace force tends to return the drops to a spherical shape. When the velocity reaches zero, the Young-Laplace force is strong enough to push the moving drop in the opposite direction, against the force of buoyancy. The drops become less deformed until they regain their spherical shape. At this point, the drops may remain in contact or they may separate. The critical velocity would be the initial velocity, which implies a velocity of zero when the drops fully recover their spherical shape.

As shown in Fig. 11-3, the balance of forces acting on the drops along the squeezing direction is:

$$F_{inertial} = F_{buoyancy}\cos\alpha + F_{drag} + F_{1,Young\text{-}Laplace} \tag{11-11}$$

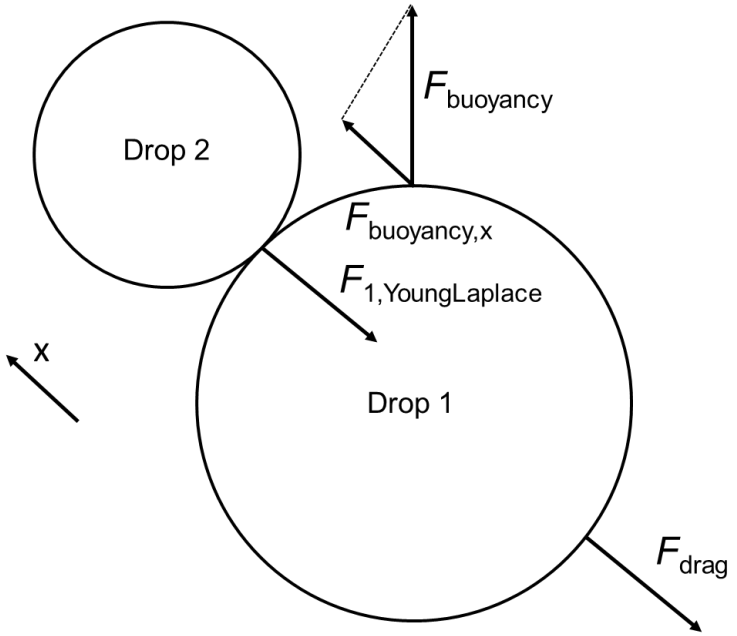

Fig. 11-3: forces acting on the drops during the bouncing process

The buoyancy-gravity force is:

$$F_{\text{buoyancy-gravity}} = \frac{\pi}{6} d_1^3 \Delta\rho g \quad . \tag{11-12}$$

The drag force is equal to:

$$F_{drag} = 3\pi\mu d_1 \dot{x} \quad , \tag{11-13}$$

where, $\dot{x}$ is the velocity of drop 1 along the x-axis. The Young-Laplace force is related to the Young-Laplace pressure, which is the pressure difference between the inside and the outside of the drops. The pressure for the drop 1 is:

$$\Delta P_{1,\text{Young-Laplace}} = \frac{2\sigma}{R_1} \quad . \tag{11-14}$$

This pressure acts on the common contact surface of the drops. The resulting force pushing the drops apart is:

$$F_{1,\text{Young-Laplace}} = \frac{2\sigma\pi R_{F,1}^2}{R_1} \quad , \tag{11-15}$$

where, $R_{F,1}$ is directly related to Δx_1, which characterizes the squeezing of drop 1, by geometric derivation of a spherical cap using the Pythagorean theorem, as shown in Fig. 11-4:

$$R_{F,1}^2 + (R_1 - \Delta x_1)^2 = R_1^2 \quad . \tag{11-16}$$

The radius of the contact area is then given by:

$$R_{F,1}^2 = 2R_1\Delta x_1 - \Delta x_1^2 \quad . \tag{11-17}$$

The displacement is assumed to be negligible compared to the drop radii, so Eq. 11-17 can be approximated by:

$$R_{F,1}^2 \approx 2R_1\Delta x_1 \quad , \tag{11-18}$$

the Eq. 11-15 becomes:

$$F_{1,\text{Young-Laplace}} \approx 4\sigma\pi\Delta x_1 \quad . \tag{11-19}$$

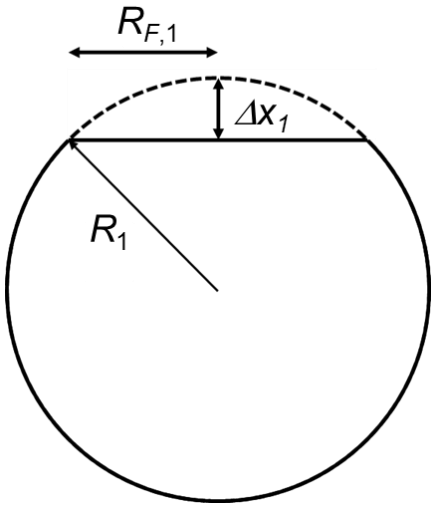

Fig. 11-4: cross-section geometry of a deformed drop

Δx_1 represent only the squeezing of the drop 1. However, the total displacement, x, must also take into account the squeezing of the drop 2, Δx_2. As the drops in the Kamp experiment are similar, the squeezing of both drops is assumed identical, i.e.:

$$F_{1,\text{Young-Laplace}} \approx 2\sigma\pi x \quad . \tag{11-20}$$

The Eq. 11-11 can be developed:

$$m\ddot{x} = mg\cos\alpha + 3\pi\mu d\dot{x} + 2\pi\sigma x \quad . \tag{11-21}$$

Eq. 11-21 is solved numerically using Matlab© to obtain the critical velocity of the system under consideration. The critical velocity is averaged along the relative horizontal position of the drops before impact.

The parameters of the Eq. 11-21 are varied separately to obtain an empirical expression for the critical velocity similar to the numerical solution of Eq. 11-21:

$$v_{\text{critical,simulation}} \approx 0.055\left(\frac{\Delta\rho g d^6 \mu^3}{\sigma^4}\right)^{0.2} \quad , \tag{11-22}$$

To fit with the experimental data of Kamp, the proportionality factor in front of Eq. 3-17 has to be adjusted to yield:

$$v_{\text{critical,experiment}} \approx 0.014\left(\frac{\Delta\rho g d^6 \mu^3}{\sigma^4}\right)^{0.2} \quad , \tag{11-23}$$

The Eq. 11-23 is a first step to evaluate the critical velocity between two moving drops, but it needs to be validated with more experimental data.

11.3 Validation of the Contact Time Model

After a non-bouncing collision, drops may eventually coalesce. The coalescence event depends on the time that the drops remain in contact, t_{contact}.

$$t_{\text{contact}} = \sqrt{2}\,\frac{d_1 + d_2}{v_{\text{relative}}} \tag{11-24}$$

can, in principle, be used to describe the contact time between 2 drops. To validate the Eq.11-24, the relative motion of two contacting drops is solved numerically.

Before the collision, the two considered drops move vertically according to their single-drop velocity, $v_{i,\infty}$. The swarm effect is not taken into account as it scales the single-drop velocity proportionally and thus the contact time according to Eq.11-24.

An elastic collision between the drops is then assumed, i.e. conservation of the total momentum:

$$m_1 v_{1,\infty} + m_2 v_{2,\infty} = (m_1 + m_2) v_0 \quad , \tag{11-25}$$

This results in an identical velocity for both drops after the impact, v_0:

$$v_0 = \frac{m_1 v_{1,\infty} + m_2 v_{2,\infty}}{m_1 + m_2} \quad . \tag{11-26}$$

After the initial contact, due to their different diameters, their individual velocities will shift relative to their collision velocities and the drops will rotate around their centre of mass, as shown on the right-hand side of Fig. 11-5.

The position of the centre of mass is given by the torque balance between the sum of the individual torques and the torque of the system consisting of the two drops. Thus, at the centre of drop 1, the balance of moments is equal to:

$$x_{1,\text{center}}\left(m_1 + m_2\right) = \frac{\left(d_1 + d_2\right)}{2} m_2 + 0 m_1 \quad , \tag{11-27}$$

$x_{1,\text{center}}$ is the distance between the center of drop 1 and the center of mass of both drops, its final expression is:

$$x_{1,\text{center}} = \frac{m_2\left(d_1 + d_2\right)}{2\left(m_1 + m_2\right)} \quad . \tag{11-28}$$

The location of the center of mass from the center of drop 2, $x_{2,\text{center}}$, is evaluated similarly:

$$x_{2,\text{center}} = \frac{m_1\left(d_1 + d_2\right)}{2\left(m_1 + m_2\right)} \quad . \tag{11-29}$$

To evaluate the contact time between two drops, the relative angular motion about the centre of mass is evaluated from the balance of forces acting on the drops. Different forces are considered: the drag force, the buoyancy force and the inertial force, as shown on the left side of Fig. 11-5. The buoyancy-gravity force is:

$$F_{i,\text{buoyancy-gravity}} = \frac{\pi}{6} d_i^3 \Delta\rho g \quad . \tag{11-30}$$

The drag force is decoupled into two contributions: a vertical and an angular force. The vertical contribution related to the motion at velocity, v_0:

$$F_{drag,v0} = 3\pi\mu d_i v_0 \quad . \tag{11-31}$$

The angular force is:

$$F_{i,\text{drag,angular}} = 3\pi\mu d_i x_{i,\text{center}}\dot{\alpha} \quad , \tag{11-32}$$

where $\dot{\alpha}$ is the angular velocity of the drops around their center of mass. These 3 forces are balanced by the inertial force, F_{angular}:

$$F_{i,\text{buoyancy}} = \frac{\pi}{6} d_i^3 \Delta\rho x_{i,\text{center}}\ddot{\alpha} \quad , \tag{11-33}$$

where $\ddot{\alpha}$ is the angular acceleration of the drops around their center of mass. Since both drops are in contact, the equilibrium of forces at the point of contact along the angular direction, is given by:

$$\begin{aligned} &F_{1,\text{angular}} + F_{2,\text{angular}} = F_{1,\text{buoyancy}} \sin\alpha - F_{2,\text{buoyancy}} \sin\alpha \times \\ &\times - F_{1,drag,angular} - F_{2,drag,angular} - F_{1,vertical,angular} \sin\alpha + F_{2,vertical,angular} \sin\alpha \end{aligned} \quad . \tag{11-34}$$

The balance of forces describing the relative angular motion of the drops about their centre of mass is given by:

$$\begin{aligned} &\left(m_1 R_{g1} + m_2 R_{g2}\right)\ddot{\alpha} = m_1 g \sin\alpha - m_2 g \sin\alpha \times \\ &\times - 3\pi\mu d_1 R_{g1}\dot{\alpha} - 3\pi\mu d_2 R_{g2}\dot{\alpha} - 3\pi\mu d_1 v_0 \sin\alpha + 3\pi\mu d_2 v_0 \sin\alpha \end{aligned} \quad . \tag{11-35}$$

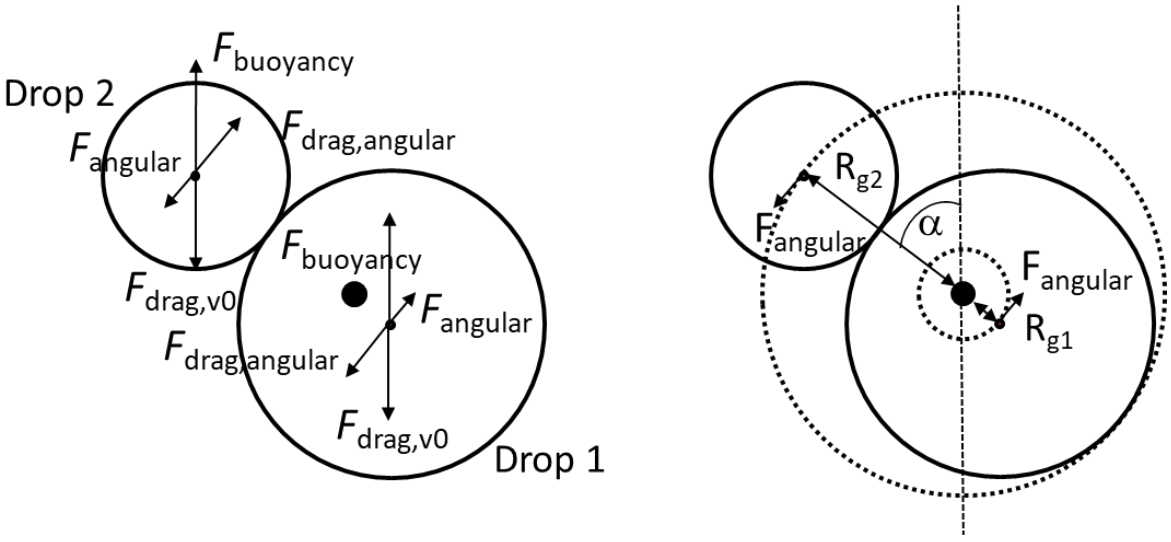

Fig. 11-5: Representation of the drops motion considered to validate Eq. 3-26

Eq. 11-35 is solved numerically using Matlab©. Several conditions are considered for the numerical resolution. Firstly, the initial angular velocity is zero. Secondly, it is assumed that the drops enter into the collision at a certain relative angle, $\alpha_{\text{collision}}$, which varies between 0 and $\pi/2$. The separation of the drops is characterized by the angle of separation, $\alpha_{\text{detachment}}$:

$$\alpha_{\text{detachment}} = \pi - \alpha_{\text{collision}} \quad , \tag{11-36}$$

The contact time is therefore the time taken for the drops to move from the angle of collision to the angle of separation. The contact time is evaluated for different drop diameters. For each drop diameter, the contact time is averaged along the relative horizontal position of the drops, which varies between 0 and $(d_1 + d_2)/2$.

The resulting ratio between the contact time obtained from the simulation and Eq. 3-26 is shown in Fig. 11-6. The physicochemical properties, density difference and viscosity of the continuous phase are varied to see their effect on the simulation. The results are shown in Tab. 11-1. A change in the density difference and viscosity by a factor of three results in a change in the proportionality factor of 3%. According to the results, the proportionality factor, equal to $\sqrt{2}$ [8, 14] in Eq. 11-24, should be adjusted to 1.52 to yield:

$$t_{\text{contact}} = 1.52 \frac{d_1 + d_2}{v_{\text{relative}}} \quad . \tag{11-37}$$

The Eq. 11-37 is evaluated using the single-drop velocity model. Contact-time modelling could be enhanced by adopting the swarm-velocity model to yield a more realistic expression for the contact time. Nevertheless, this adjustment is not required in the present thesis: ReDrop evaluates the coalescence probability at each time step for as long as droplets maintain a non-zero probability of contact, rather than relying on a total contact time as defined in Eq. 11-37.

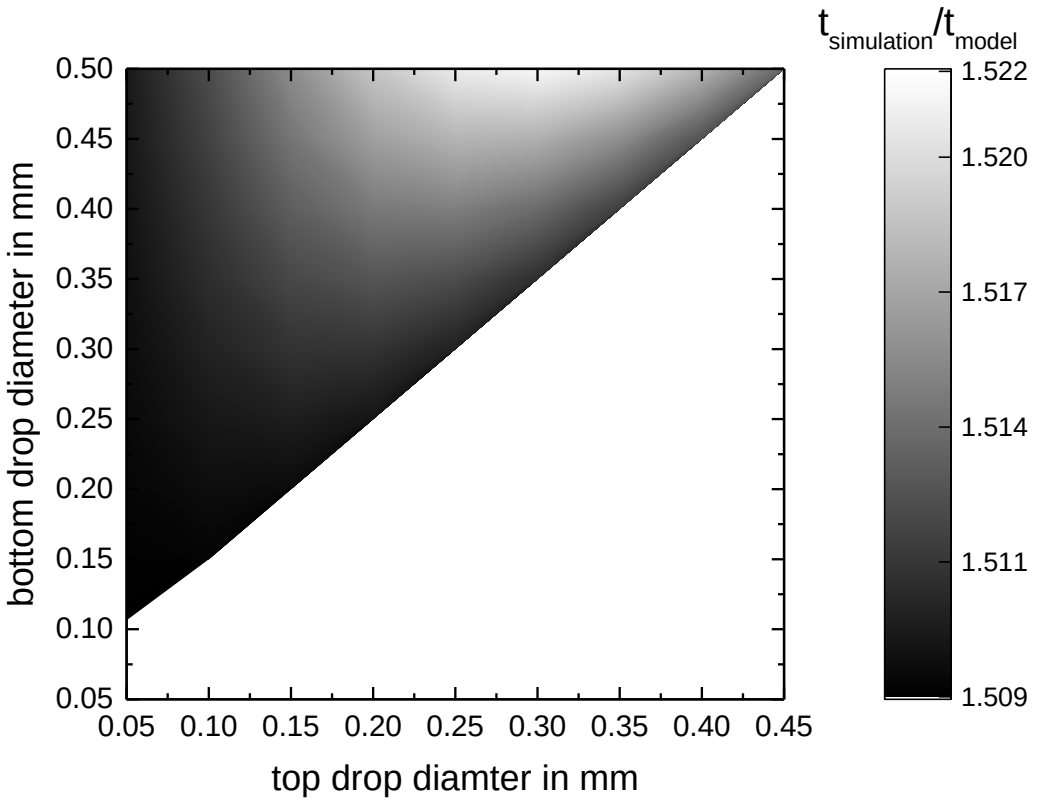

Fig. 11-6: Contact time of two drops with diameters varying between 0 and 0.5 mm for continuous phase viscosity of 3 mPas and a density difference of 393 kg/m². Comparison between the model, described in chapter 3.4.1, and the simulation

		Density difference in kg/m³	
		131	393
Viscosity of continuous phase in mPas	1	1.512	1.545
	3	1.509	1.513

Tab. 11-1: proportionality factor for the contact time averaged along the drop diameters evaluated for different physico-chemical properties.

11.4 Derivation of the Generalized Expression of the Coalescence Time

Two contacting droplets in a dispersion are subject to a driving force that pushes them together. As a consequence, the film thickness between the two drops decreases with time until

it reaches a critical value at which the drops coalesce. The time taken for this process, $t_{coalescence}$, influences the probability of coalescence between the two drops. The model for the coalescence time is derived in this chapter following general concept introduced by Henschke [5].

As shown inFig. 11-7, the formation of a dimple is assumed at the contact surface between the drops. A dimple is characterized by a maximum thickness along the central axis between the drops and has a thinner edge with radius R_F. Based on experimental data, an asymmetry has been considered, meaning that the driving force, $F_{driving}$, is not applied at the centre of the dimple [5], but assymetrically by introducing a shift by R_v from the center. The asymmetric dimple is also shown differently inFig. 11-7, which is a different representation used for modelling purposes. As illustrated, the figure displays the dimple in linear form, with the perimeter of the dimple being defined by the two lengths L .

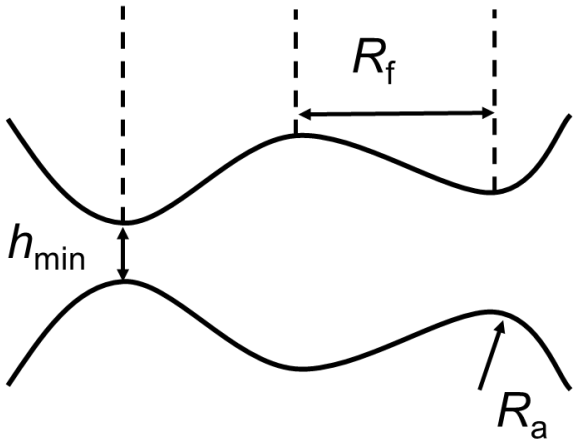

Fig. 11-7: Cross-sectional view of an asymmetric dimple

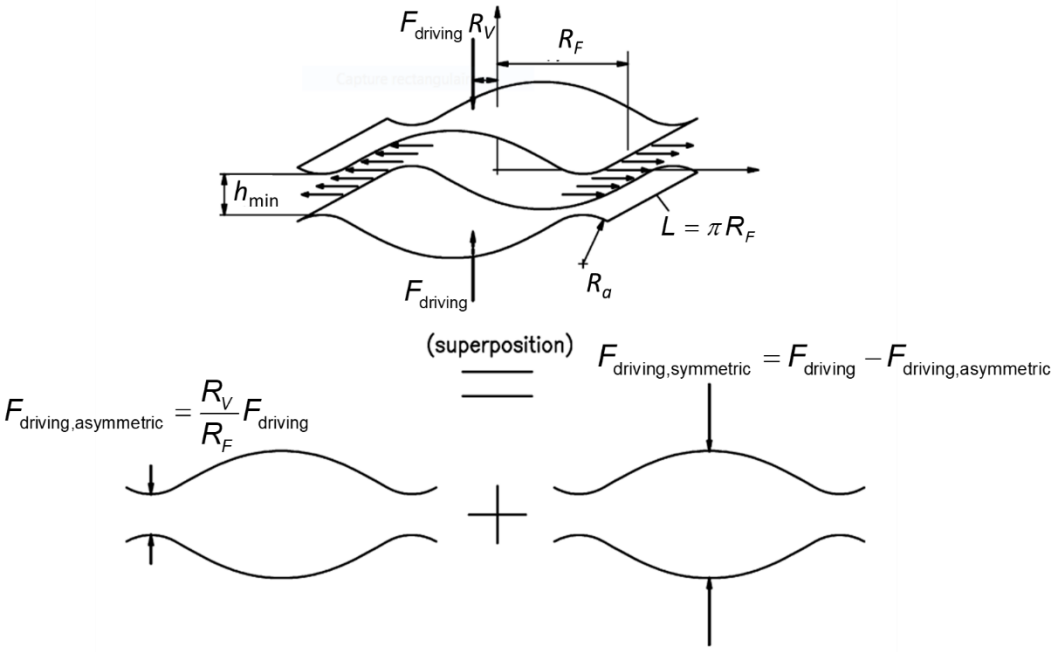

Fig. 11-8: Asymmetry in the dimple formation between two contacting drops [5]

According to Henschke, the driving force can then be divided into two contributions according to the superposition principle: one in the centre of the dimple, $F_{driving,symmetric}$, and one at the edge of of the dimple, $F_{driving,asymmetric}$, where the thickness is minimum. These two contributions are superimposed in order to evaluate the film drainage:

$$F_{driving,asymmetric} = \frac{R_v F_{driving}}{R_F} \tag{11-38}$$

$$F_{driving,symmetric} = F_{driving} - F_{driving,asymmetric} \tag{11-39}$$

Henschke showed that the asymmetric contribution contributes to faster coalescence. The asymmetry leads to an opening of the dimple on one side and an faster approach of the drop interface on the opposite side during film drainage [15]. The symmetric driving force contribution results in a coalescence time much longer than the asymmetric contribution. Therefore, the symmetric driving force is not considered as time-determining contribution in the coalescence time modelling.

Eq. 11-38 shows the ratio R_V/R_F, which defines the asymmetry. This ratio replaced in the following by the dimensionless parameter r_s^*,

$$r_s^* = \frac{R_v}{R_F} \tag{11-40}$$

Eq. 11-38 then becomes:

$$F_{\text{driving,asymmetric}} = r_s^* F_{\text{driving}} . \tag{11-41}$$

The kinetics of the dimple drainage must be modelled in order to estimate the time taken for the drops to coalesce. Due to the geometry of the dimple, the flow is limited where the dimple thickness is minimum. The film drainage at that point can be considered as a film drainage between two cylinders characterized by a radius R_a, which is the curvature at the edge of the dimple, and by a length, L, which is the contour of the dimple:

$$L = \pi R_F \quad . \tag{11-42}$$

The two cylinders are pushed together by the driving force, $F_{\text{driving,asymmetric}}$. The liquid flow between the two cylinders then induces a fluid-dynamic force. These two forces are balanced:

$$\left|F_{\text{fluid-dynamic}}\right| = F_{\text{driving,asymmetric}} = r_s^* F_{\text{driving}} \quad . \tag{11-43}$$

To model the flow between two approaching cylinders, Henschke's uses the model of MacAvoy and Kintner [33], who modelled the flow between two approaching spheres.

Immobile interfaces are assumed, due to the impurities typically present. The film drainage at the edge of the dimple can be simplified by a two-dimensional representation of the flow between two approaching disks.

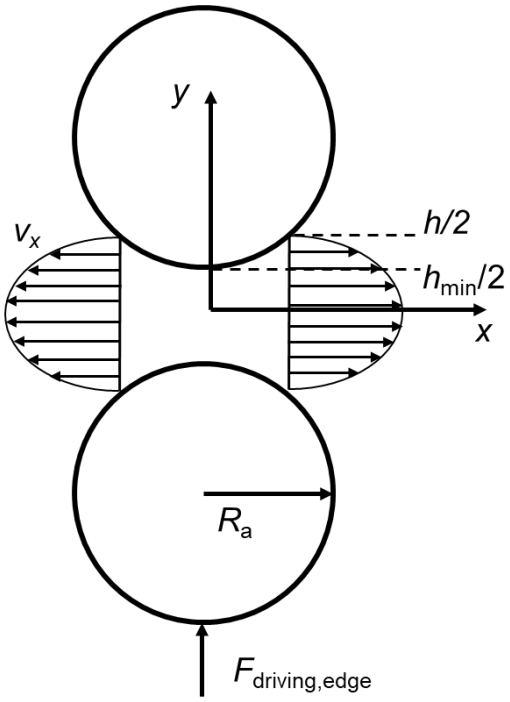

Fig. 11-9: velocity profile between two approaching cylinders [5]

Due to the small dimension, laminar flow can be assumed, so that, the velocity profile is parabolic, maximum at the centre of the distance between the cylinders and zero velocity at the cylinder surface. The flow velocity thus becomes:

$$v_x(x,y) = \left(\frac{h^2}{4} - y^2\right) f(x) \quad . \tag{11-44}$$

The first term in Eq. 11-44, $\left(h^2/4 - y^2\right)$, represents the parabolic profile of the flow. The second term, $f(x)$, independent of *y*, is necessary to satisfy the mass balance along the x-axis. The horizontal volume flow rate, for any value of x, is given by the integrating the flow velocity along the y-axis:

$$\dot{V}_x = L \int_{-\frac{h}{2}}^{\frac{h}{2}} \left(\frac{h^2}{4} - y^2\right) f(x) dy \quad , \tag{11-45}$$

which yields the horizontal flow rate:

$$\dot{V}_x = L f(x) \left[\frac{h^2 y}{4} - \frac{y^3}{3}\right]_{-\frac{h}{2}}^{\frac{h}{2}} \quad , \tag{11-46}$$

and

$$\dot{V}_x = L\frac{h^3}{6}f(x) \quad , \tag{11-47}$$

the volume flow rate can also be expressed in terms of the approach velocity of the two cylinders, $dh_{\min}/dt$:

$$\dot{V}_x = Lx\frac{dh_{\min}}{dt} \quad . \tag{11-48}$$

$f(x)$ can now be determined by combining Eqs. 11-47 and 11-48 :

$$f(x) = \frac{6x}{h^3}\frac{dh_{\min}}{dt} \quad . \tag{11-49}$$

The flow velocity is then:

$$v_x(x,y) = -\left(\frac{h^2}{4} - y^2\right)\frac{6x}{h^3}\frac{dh_{\min}}{dt} \quad . \tag{11-50}$$

Assuming Newtonian behavior for the continuous phase, the differential pressure along the flow is given by:

$$\frac{dp}{dx} = \mu\frac{d^2v_x}{dy^2} \quad . \tag{11-51}$$

With the derivative of Eq. 11-50:

$$\frac{dp}{dx} = \mu\frac{12x}{h^3}\frac{dh_{\min}}{dt} \quad . \tag{11-52}$$

As shown in Fig. 11-10, x and h are geometrically linked by the Pythagorean theorem:

$$R_a^2 = x^2 + \left(R_a - \frac{h - h_{\min}}{2}\right)^2 \quad , \tag{11-53}$$

where, x is a function of h:

$$x = \sqrt{R_a^2 - \left(\frac{h_{\min} - h + 2R_a}{2}\right)^2} \quad . \tag{11-54}$$

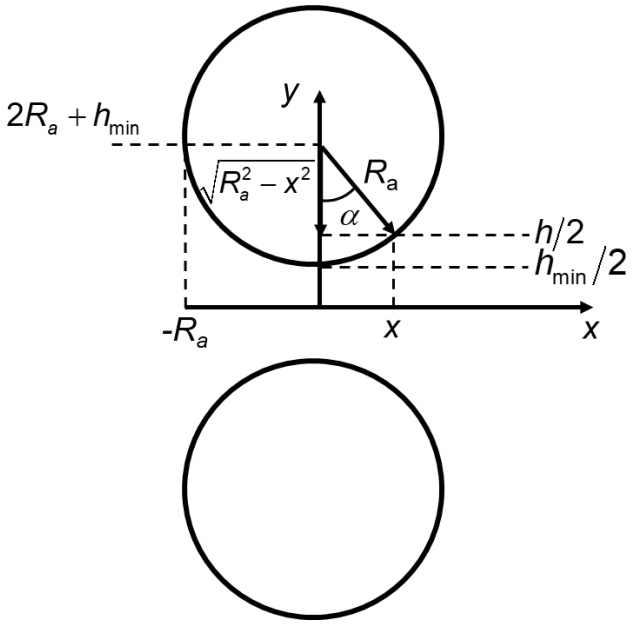

Fig. 11-10: Pythagorean theorem to relate *x* to *h*

Integrating the pressure, Eq. 11-51, along the x-axis gives the pressure along the flow occurring in between the two cylinders:

$$\int_0^p dp' = 12\mu \frac{dh_{\min}}{dt} \int_{-R_a}^{x} \frac{x'}{h^3} dx' \tag{11-55}$$

The right-hand side of the Eq. 11-55 can be expressed as an integral along *h*. This change in the variable gives with Eq.11-54:

$$dx' = -\frac{h' - h_{\min} - 2R_a}{2\sqrt{R_a^2 - \left(\frac{h_{\min} - h' + 2R_a}{2}\right)^2}} dh' \quad . \tag{11-56}$$

The boundaries of the integral must also to be substituted in terms of h using Eq. 11-54. As shown in Fig. 11-10, the lower bound $x = -R_a$ is replaced by $h = 2R_a + h_{\min}$. *x* is replaced by *h* for the upper bound.

This can be substituted into Eq. 11-55 to give:

$$\int_0^p dp' = 12\mu \frac{dh_{\min}}{dt} \int_{2R_a + h_{\min}}^{h} \frac{\sqrt{R_a^2 - \left(\frac{h_{\min} - h' + 2R_a}{2}\right)^2}}{h'^3} \frac{h_{\min} + 2R_a - h'}{2\sqrt{R_a^2 - \left(\frac{h_{\min} - h' + 2R_a}{2}\right)^2}} dh' \quad , \tag{11-57}$$

$$\int_0^p dp' = 6\mu \frac{dh_{\min}}{dt} \int_{h_{\min}}^{h} \frac{h_{\min} + 2R_a - h'}{h'^3} dh' \quad . \tag{11-58}$$

Solving the integral gives:

$$p = 6\mu \frac{dh_{\min}}{dt} \left(\frac{1}{h} - \frac{h_{\min} + 2R_a}{2h^2} \right) - \left(\frac{1}{h_{\min} + 2R_a} - \frac{h_{\min} + 2R_a}{2\left(h_{\min} + 2R_a\right)^2} \right) \quad , \tag{11-59}$$

$$p = 6\mu \frac{dh_{\min}}{dt} \left(\frac{1}{h} - \frac{h_{\min} + 2R_a}{2h^2} \right) - \left(\frac{1}{2\left(h_{\min} + 2R_a\right)} \right) \quad . \tag{11-60}$$

Eq. 11-60 describes the pressure difference across the width of the cylinders at the position *x*. Integrating the pressure across the width and length of the cylinders gives the force acting on the entire cylinder surface, $F_{\text{fluid-dynamic}}$, and against the driving force:

$$\left| F_{\text{fluid-dynamic}} \right| = 2L \int_0^{Ra} p(h(x))dx \tag{11-61}$$

Before solving the Eq. 11-61, Eq. 11-60 needs to be slightly modified mathematically using Eq. 11-54:

$$p = 6\mu \frac{dh_{\min}}{dt} \left(\frac{1}{2h} + \frac{\sqrt{R_a^2 - x^2}}{h^2} - \frac{1}{2\left(h_{\min} + 2R_a\right)} \right) \quad . \tag{11-62}$$

To make it easier to solve the equation, *x* and *h* in Eq. 11-62 are expressed in polar coordinates. Based on Fig. 11-10, the cosine and sine functions of the angle, α are:

$$\begin{cases} \sin\alpha = \dfrac{x}{R_a} \\ \cos\alpha = \dfrac{\sqrt{R_a^2 - x^2}}{R_a} \end{cases} \quad . \tag{11-63}$$

Eq. 11-54 can then be inverted to give an expression for h as function of x:

$$h = h_{\min} + 2\left(R_a - \sqrt{R_a^2 - x^2}\right) \quad , \tag{11-64}$$

and expressed as function of the polar angle:

$$h = 2R_a\left(\frac{h_{\min}}{2R_a} + 1 - \cos\alpha\right) \quad . \tag{11-65}$$

The change of variables for the integration of the Eq. 11-61 implies with Eq. 11-63:

$$dx = -R_a \cos\alpha d\alpha \quad . \tag{11-66}$$

Eq. 11-62 then leads to:

$$p = 6\mu\frac{dh_{\min}}{dt}\times$$
$$\times\left(\frac{1}{4R_a\left(\frac{h_{\min}}{2R_a} + 1 - \cos\alpha\right)} + \frac{R_a\cos\alpha}{4R_a^2\left(\frac{h_{\min}}{2R_a} + 1 - \cos\alpha\right)^2} - \frac{1}{2\left(h_{\min} + 2R_a\right)}\right) \quad , \tag{11-67}$$

Thus, Eq. 11-61 results in:

$$F_{\text{fluid-dynamic}} = -12L\mu\frac{dh_{\min}}{dt}\times$$
$$\times\int_0^{\frac{\pi}{2}}\left(\frac{\cos\alpha\left(\frac{h_{\min}}{2R_a} + 1 - \cos\alpha\right) + \cos^2\alpha}{4\left(\frac{h_{\min}}{2R_a} + 1 - \cos\alpha\right)^2} - \frac{R_a\cos\alpha}{2\left(h_{\min} + 2R_a\right)}\right)d\alpha \quad , \tag{11-68}$$

$$F_{\text{fluid-dynamic}} = -3L\mu\frac{dh_{\min}}{dt}\int_0^{\frac{\pi}{2}}\cos\alpha\left(\frac{\left(\frac{h_{\min}}{2R_a} + 1\right)}{\left(\frac{h_{\min}}{2R_a} + 1 - \cos\alpha\right)^2} - \frac{1}{\left(\frac{h_{\min}}{2R_a} + 1\right)}\right)d\alpha \quad . \tag{11-69}$$

Integration with Mathematica© of Eq. 11-69 and taking into account that $R_a/h_{\min} >> 1$, the fluid-dynamic force is finally obtained:

$$F_{\text{fluid-dynamic}} \approx -3\pi^2 R_F\mu\frac{dh_{\min}}{dt}\left(\frac{R_a}{h_{\min}}\right)^{3/2} \quad . \tag{11-70}$$

Substituting into Eq. 11-43, the driving force that pushes the drop together, e.g. buoyancy, must satisfy the following relationship:

$$F_{\text{driving}} \approx -\frac{3\pi^2 \mu R_F}{r_s^*}\left(\frac{R_a}{h_{\min}}\right)^{3/2}\frac{\mathrm{d}h_{\min}}{\mathrm{d}t} \quad . \tag{11-71}$$

This describes the evolution of the film thickness, $h_{\min}$, with the time. The process starts at an arbitrary drop distance, h_0, and ends when the drops merge, i.e. at the thickness where the attractive Van der Waals forces are strong enough for the interfaces of the two drops to attract each other and induce coalescence, h_{critical}. The time taken to reach h_{critical} is the coalescence time, $t_{\text{coalescence}}$, which can be evaluated by integrating Eq.11-71:

$$\int_{h_0}^{h_{critical}} \frac{\mathrm{d}h_{\min}}{h_{\min}^{3/2}} = -\int_{0}^{t_{\text{coalescence}}} \frac{F_{\text{driving}} r_s^*}{3\pi^2 \mu R_F R_a^{3/2}}\mathrm{d}t \quad . \tag{11-72}$$

After integration, coalescence time can be determined:

$$\frac{F_{\text{driving}} r_s^*}{3\pi^2 \mu R_F R_a^{3/2}}\left(t_{\text{coalescence}} - 0\right) = -2\left(\frac{1}{\sqrt{h_0}} - \frac{1}{\sqrt{h_{critical}}}\right) \quad , \tag{11-73}$$

$$t_{\text{coalescence}} = -\frac{6\pi^2 \mu R_F R_a^{3/2}}{F_{\text{driving}} r_s^*}\left(\frac{1}{\sqrt{h_0}} - \frac{1}{\sqrt{h_{critical}}}\right) \tag{11-74}$$

As the h_{critical} can be considered to be very small compared to h_0, this leads to:

$$t_{\text{coalescence}} \approx \frac{6\pi^2 \mu R_F R_a^{3/2}}{F_{\text{driving}} r_s^* \sqrt{h_{critical}}} \quad . \tag{11-75}$$

Eq. 11-75 is then the basis for evaluating the coalescence time for different situations as explained in the chapter 3.4.2.

11.5 Optimized Cell Assembly

The scheme of the optimized stirring cell is shown in Fig. 11-11. The equipment is divided into three parts: the glass cylinder is sandwiched between 2 stainless steel parts. The lower part, shown in Fig. 11-12, consists of the sealing block and the flushing ball valve. The upper part, shown in Fig. 11-13, consists of the gearbox, the sealing block and the shafts.

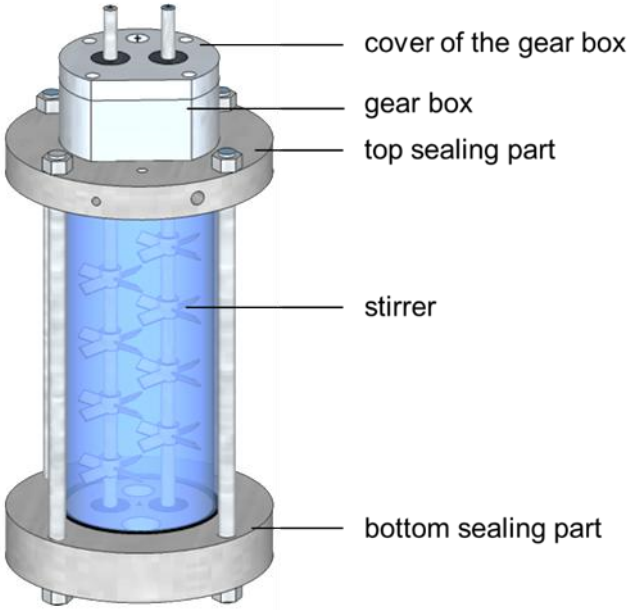

Fig. 11-11: 3D representation of the settling cell.

To assemble the stirring cell, a frame is required to support the cell, motor, and LED panel. The frame is made of strut profiles (Bosch Rexroth AG, 30mm*30mm). The motor (Heidolph RZR 2021, Heidolph, Germany) is fixed to the back of the frame with 2 nuts (M6). The motor can reach a mixing speed up to 1500 rpm in a few seconds.

The first step to assemble the stirring cell is to fix the bottom part to the frame with 3 nuts (M6), 90° apart. The nuts are screwed into the stainless steel block and fixed to the frame with bolts. As shown in Fig. 11-12, there are two ball bearings in this part. They guide the shafts and have an outer diameter of 22 mm and an inner diameter of 8 mm. A teflon seal is in the contact area between the glass cylinder and the stainless steel block. The size is adapted to the diameter and thickness of the glass cylinder. The vertical thickness of the seal ring is 3 mm. The contact surface with the glass must be flat to allow a high contact area and thus a good seal.

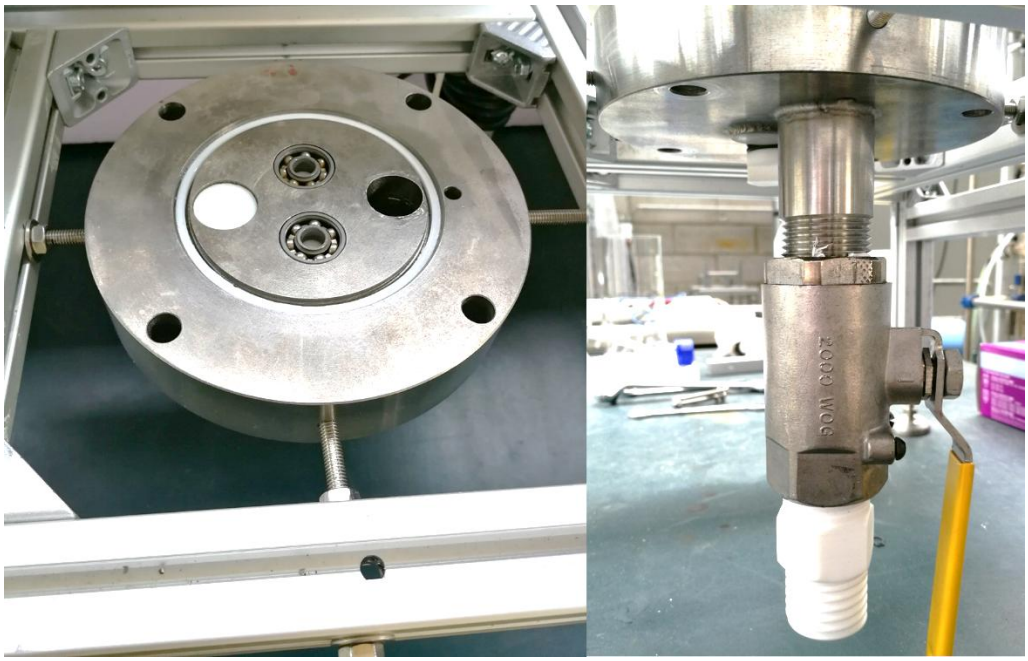

Fig. 11-12: Bottom part of the cell

Next, the top of the cell is assembled. The gearbox is placed on the stainless steel block. The shafts are then inserted through the gearbox. The gears are screwed onto the shafts inside the gear box. The gears have 40 teeth, the pitch diameter is 32 mm, the hub diameter is 19 mm and the bore diameter is 8 mm.

The gear box can then be closed: 4 M4 bolts are screwed through the gearbox to the top seal. Bolts are placed on the top of the gearbox cover to hold these parts together. Ball bearings, identical to those used in the lower part of the cell, are fixed in the gearbox cover and the shafts are held by circlips. The circlips have an outer diameter of 8 mm and an inner diameter of 7.6 mm.

The Teflon seal ring is placed in its slot in the upper sealing part. A 12 mm high Teflon cup is then inserted through the shafts to prevent the formation of air bubbles when the cell is fully filled with solvent. The stirrers can then be mounted on the shafts with the correct spacing between the modules as shown in Fig. 11-13. The drawings of the different parts of the top section are shown in Appendix 11.6.

The three parts, the top and bottom parts and the glass tube, are finally assembled together.

The glass cylinder, the assembled upper part and the lower part are finally fixed together. The fixation is done with 4 M10 bolts that are screwed with studs. These studs are used to seal the cell and prevent leakage. There are springs to prevent the glass from breaking. The glass tube, made of borosilicate glass, comes from Aachener Quarz-Glas Technologie Heinrich GmbH & Co. KG. The outer diameter is 90 mm with a thickness of 3.5 mm. The height is 200 mm. A minimum inner diameter of 80 mm is required to avoid wall effects on the sedimentation and a sufficient height is necessary for a good evaluation of the sedimentation and the coalescence curve [5].

The motor, placed next to the cell, is then connected to one of the shafts of the stirring cell by a drive belt (80 teeth, length 400 mm and width 15 mm). The belt is guided by pulleys (15 teeth, 15 mm wide and 5 mm pitch) as shown in Fig. 6-8.

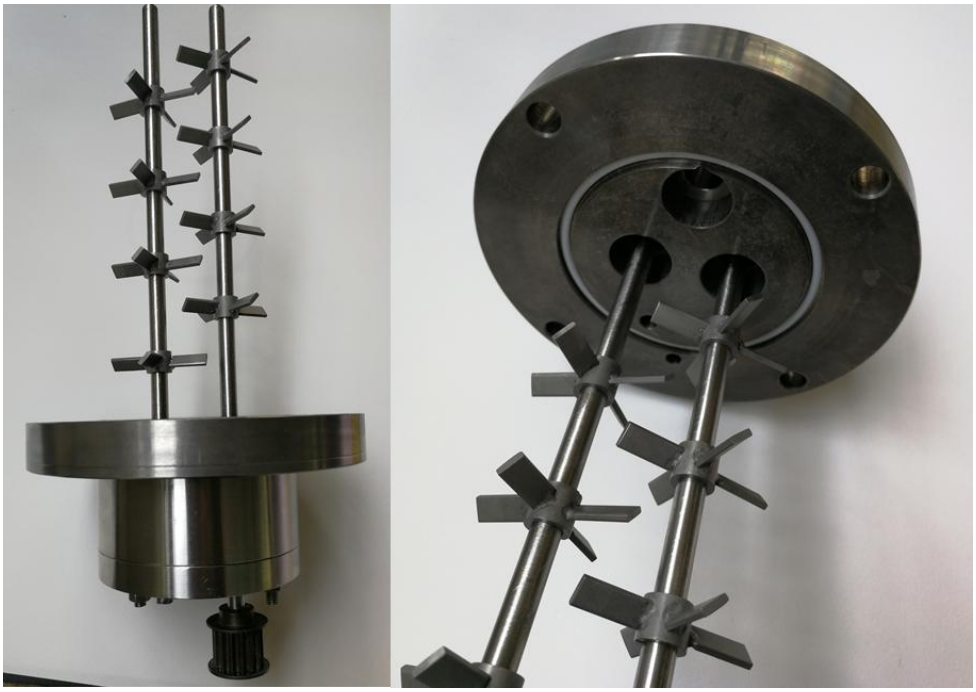

Fig. 11-13: Upper part of the settling cell

11.6 Settling Cell drawings

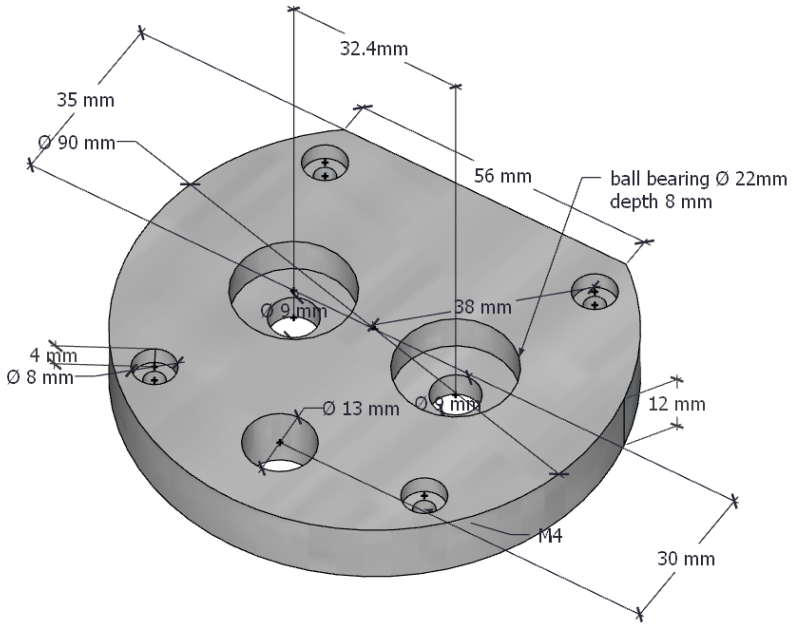

Fig. 11-14: Cover of the gear box

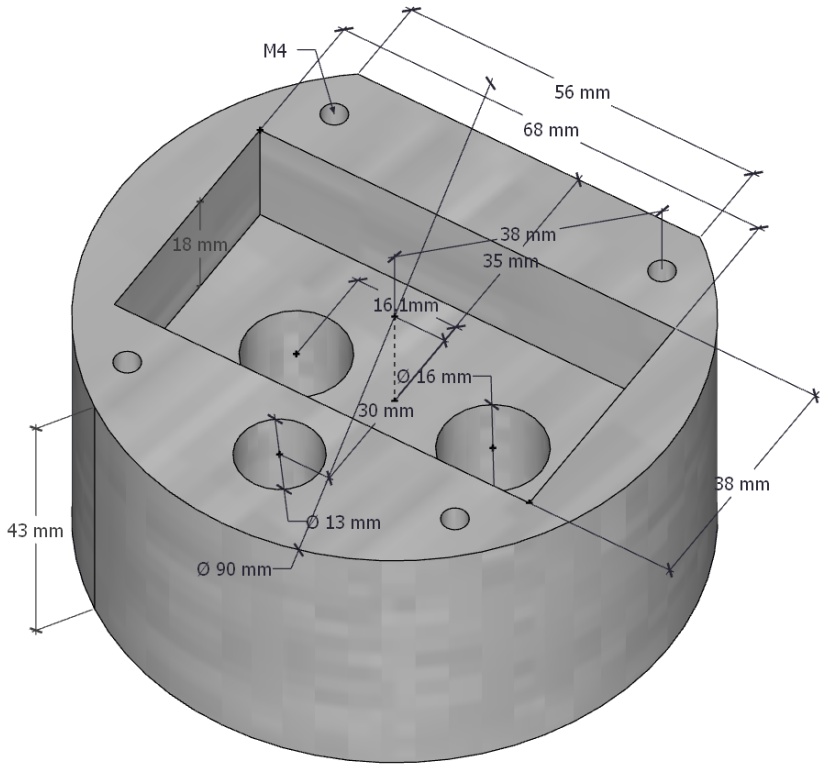

Fig. 11-15: The gear box

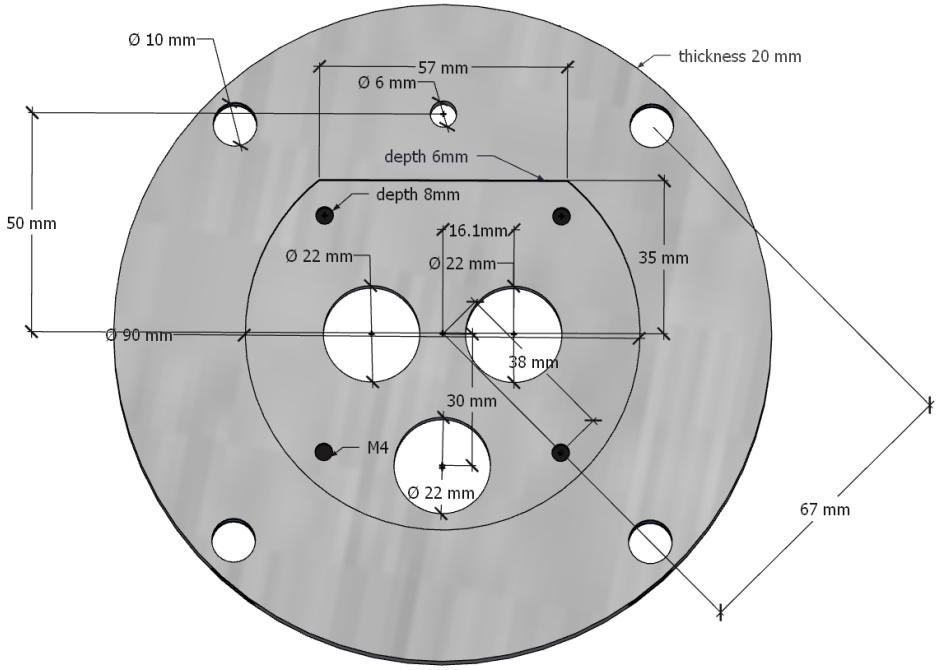

Fig. 11-16: Top view of the stainless steel block placed over the glass tube

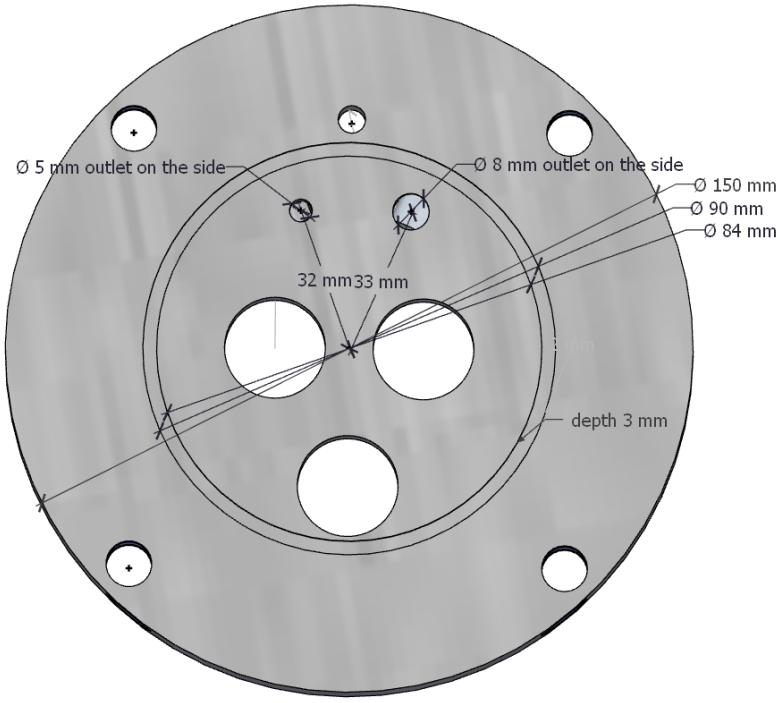

Fig. 11-17: Bottom view of the stainless steel block placed over the glass tube

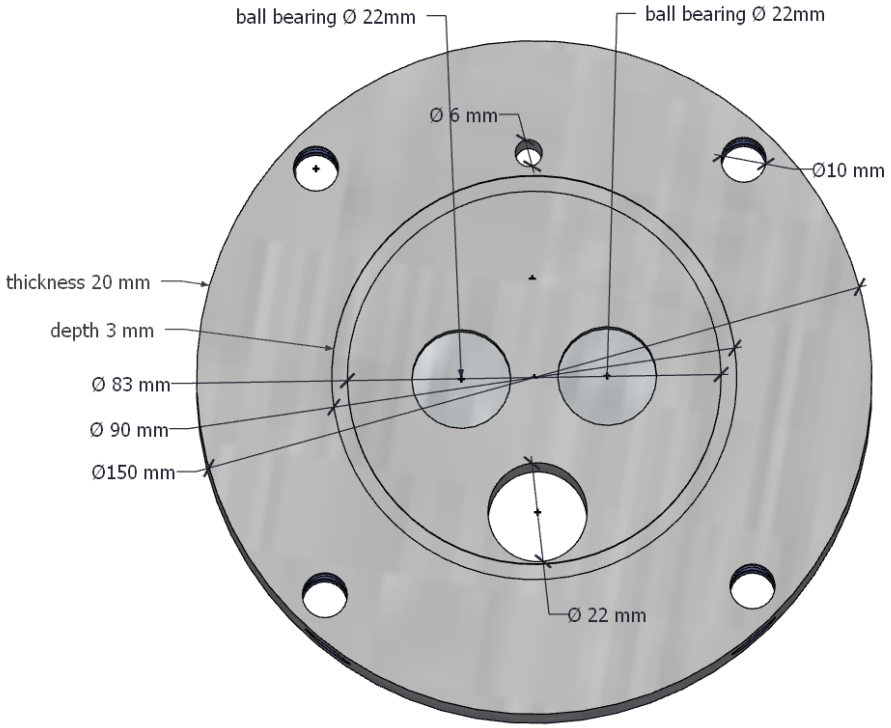

Fig. 11-18: Top view of the stainless steel block placed under the glass tube

11.7 Properties of the Chemicals Used for the Comparison of the Stirring and the Shaking Cells

The chemicals used in the experiments are paraffin oil, water and salt. The paraffin oil was provided by Fauth + Co.KG and has the reference FC2006 (batch number: 64200048). The water used was deionized water produced directly from a deionization cartridge. The salt used was sodium chloride supplied by VWR (batch number: 12K220010).

Both equilibrium phases were analyzed for density and viscosity using the DSA 5000M instrument in combination with Lovis 2000ME from Anton Paar, Graz, Austria. The results are presented in Tab. 11-2. Settling experiments were carried out with a phase ratio (a/o) of 2/5.

		20°C	25°C
paraffin oil	density (kg/m³)	822.913	819.597
	viscosity (mPas)	10.06	8.48
deionized water + 50 mmol/L NaCl	density (kg/m³)	1000.237	999.041
	viscosity (mPas)	1.030	0.924

Tab. 11-2: density and viscosity of the saturated phases

11.8 Matlab Code for the Numerical Evaluation of the Settling Time

```
%% numerical evaluation of the settling time, written for the shaking cell
clc
clear all
close all

%% this block is related to the opening of the movie file
readfile = 'exp2.mp4'; % name of the movie
savefile = 'Test.mat'; % name of the file .mat which has to be saved

vidObj = VideoReader(readfile);
vidHeight = vidObj.Height; % height of each frame
vidWidth = vidObj.Width; % width of each frame
numFrames = vidObj.NumberOfFrames; % number of frame in the movie
nbrsec = uint16(numFrames / 29);
step = 2;
nbravfin = 2;
% Creation of a cell array, each cell is a matrix (height, width, 3).
% it corresponds to the light intensity for each pixel at a specific
% time in red, green and blue
Data = cell((uint16((nbrsec - nbravfin) / step)),1);
Datafinal = cell((uint16((nbrsec - nbravfin) / step)),1);
% Construction of the cell array in grey level
```

```
for i = 1:(uint16((nbrsec - nbravfin) / step))
    Data{i} = rgb2gray(read(vidObj,((i - 1) * 29 *step) + 1));
end

save(savefile,'Data','-v7.3'); %% cell array saved

%% masks creation for each bottle

figure(1); imshow(Data{((nbrsec - nbravfin) / step)});
% definition of the interface for the first bottle
[X Y] = ginput(1);
interface1 = Y;
% definition of the area of interest for the first bottle
h1 = imrect;
pos1 = getPosition(h1);
BW1 = createMask(h1);
close(figure(1));
%cropping of the area of interest for the first bottle at different time
for i = 1:(uint16((nbrsec - nbravfin) / step))
   Datacut1{i,1} = abs (uint8(BW1(:,:)).*Data{i});
end
% definition of the interface for the second bottle
figure(1); imshow(Data{((nbrsec - nbravfin) / step)});
[X Y] = ginput(1);
interface2 = Y;
% definition of the area of interest for the second bottle
h2 = imrect;
pos2 = getPosition(h2);
BW2 = createMask(h2);
close(figure(1));
% cropping of the area of interest for the second bottle at different time
for i = 1:(uint16((nbrsec - nbravfin) / step))
   Datacut2{i,1} = abs (uint8(BW2(:,:)).*Data{i});
end
```

```
%% evaluation of the average grey lavel for each pixel line
begix1 = uint16(pos1(2)) + 1;
begiy1 = uint16(pos1(1)) + 1;
endx1 = uint16(pos1(2) + pos1(4));
endy1 = uint16(pos1(1) + pos1(3));
% definition of the matrix named
% average1(height of the area of interest,time) for the first bottle
for o = 1:(uint16((nbrsec - nbravfin) / step))
    for i = 1:endx1 - begix1
        average1(i,o) = mean(Datacut1{o,1}(begix1 + i,begiy1:endy1));
    end
end
begix2 = uint16(pos2(2)) + 1;
begiy2 = uint16(pos2(1)) + 1;
endx2 = uint16(pos2(2) + pos2(4));
endy2 = uint16(pos2(1) + pos2(3));
% definition of the matrix named
% average2(height of the area of interest,time) for the second bottle
for o = 1:(uint16((nbrsec - nbravfin) / step))
    for i = 1:endx2 - begix2
        average2(i,o) = mean(Datacut2{o,1}(begix2 + i,begiy2:endy2));
    end
end
%% definition of the settling time
orgaThreshold = 9;
aquThreshold = 3;
% first bottle
for i= 1:(uint16((nbrsec - nbravfin) / step)) - 1
    organic1(i) = 0;
    aqueous1(i) = 0;
    interfacen1 = interface1 - begix1;
% evaluation of the relative grey level compare to the last picture where 2
% clear phases are observed.
```

```
    for j = 1:endx1 - begix1
       newaverage1(j,i) = 100 * double(abs(((double(average1(j,i)) - ...
           double(average1(j,(uint16((nbrsec - nbravfin) / step)))))))./...
           double(average1(j,i)));
    end
% evaluation of the relative average grey level above and bellow the
% interface, when the thersholds are reached for both phases, the settling
% time is reached
    organic1(i) = mean(newaverage1(1:interfacen1,i));
    aqueous1(i) = mean(newaverage1(round(interfacen1):...
        round(endx1 - begix1),i)) ;
    if(organic1(i) < orgaThreshold)
        if (aqueous1(i) < aquThreshold)
            break
        end
    end
end
settling_time_first_bottle = (i - 1) * step
% second bottle
for i= 1:(uint16((nbrsec - nbravfin) / step)) - 1
    organic2(i) = 0;
    aqueous2(i) = 0;
    interfacen2=interface2 - begix2;
% evaluation of the relative grey level compare to the last picture where 2
% clear phases are observed.
    for j=1:endx2 - begix2
       newaverage2(j,i) = 100 * double(abs(((double(average2(j,i)) - ...
           double(average2(j,(uint16((nbrsec - nbravfin) / step)))))))./...
           double(average2(j,i)));
    end
% evaluation of the relative average grey level above and bellow the
% interface, when the thersholds are reached for both phases, the settling
% time is reached
```

```
    organic2(i) = mean(newaverage2(1:interfacen2,i));
    aqueous2(i) = mean(newaverage2(round(interfacen2):...
        round(endx2 - begix2),i)) ;
    if(organic2(i) < orgaThreshold)
        if (aqueous2(i) < aquThreshold)
            break
        end
    end
end
settling_time_second_bottle = (i - 1) * step
```

11.9 Matlab Code for Evaluating the Iso-Optical Experiments

On the following appendix, the Matlab code used to measure the evolution of the local hold-up from the movie of settling experiment performed with iso-optical system

```
%% blank light intensity evaluation
clc
clear all
close all
expname2 = 'settling.mov';
% Characteristic of the video
vidObjs = VideoReader(expname2);
numFrames = vidObjs.NumberOfFrames;
DataMask = read(vidObjs,numFrames);
%% boundaries of the area of interest: selection of a window located
%% in between the shafts
position = [uint16(size(DataMask, 2) / 20), 10];
Datatestb = insertText(DataMask, position,'Please, Indicate the place of',
...
    'FontSize', 30, 'BoxColor', 'black', 'TextColor', 'w');
position = [uint16(size(DataMask, 2) / 20), 50];
Datatestb = insertText(Datatestb, position, 'the more representating
slice', ...
```

```
    'FontSize', 30, 'BoxColor', 'black', 'TextColor', 'w');
imshow(Datatestb);
slice = imrect;
pause()
poss = getPosition(slice);
position = [uint16(size(DataMask, 2) / 20), 10];
Datatestb = insertText(DataMask,position,'Please, Indicate the bottom and',
...
    'FontSize', 30, 'BoxColor', 'black', 'TextColor', 'w');
position = [uint16(size(DataMask, 2) / 20), 50];
Datatestb = insertText(Datatestb,position,'the top of the settling cell',
...
    'FontSize', 30, 'BoxColor', 'black', 'TextColor', 'w');
imshow(Datatestb);
[A, B] = ginput (2);
close(figure(1));
bottoms = round(max(A(2), A(1)));
if bottoms > size(Datatestb, 2)
    bottoms = size(Datatestb, 2)
end
ups = round(min(A(2), A(1)));
%% creation of the mask of the blank (BlankMask)
% take the last frame of the experiment movie
Test = read(vidObjs,((11 * 60) + 30) * 25);
DataMask = double(imadjust((Test(round(poss(2)):round(poss(2)) + ...
    round(poss(4)), ups:bottoms, 3))));
DataMask = imsharpen(uint8(DataMask));
level = graythresh(DataMask);
BlankMaskB = im2bw(DataMask, 1.7 * level);
SE = strel('rectangle', [4 4]);
BlankMaskC = imdilate(BlankMaskB, SE);
SE = strel('rectangle', [10 9]);
Mask = imerode(BlankMaskC, SE);
% superposition the last frame with the mask, the purpose is to know
```

```
% if the mask is recovering the shafts and the stirrers, if not this
% step needs to be done again by varying the level in the function
% im2bw(DataMask, 1.7*level)
test(:, :) = double(uint8(Mask(:, :)) .* DataMask(:, :));
test(test == 0) = 255;
imshow(uint8(test))
save('Mask.mat', 'Mask');
%% take the last 6 frames of the experiment movie in order to average
%% the color intensity at the end of the experiment. Tha mask is applied
%% on these 6 frames to remove the effect of the dark regions
Data = read(vidObjs,(((13 * 60) - 5) * 25) - 5);
Vect = uint8(Data(round(poss(2)):round(poss(2)) + round(poss(4)),...
    ups:bottoms,2));
Blank(:, :) = (double(Vect .* uint8(Mask)));
for i = (((13 * 60) - 5) * 25) - 4 :1: (((13 * 60) - 5) * 25)
    Data = read(vidObjs,i);
    Vect = uint8(Data(round(poss(2)):round(poss(2)) + round(poss(4)),...
        ups:bottoms,2));
    Blank(:,:) = (double(Vect .* uint8(Mask))) + Blank(:,:);
end
If = Blank ./ 6;
%% take the 5 first frames of the experiment movie in order to average
%% the color intensity at the beginning of the experiment. Tha mask is
%% applied on these 5 frames to remove the effect of the dark regions
%beginning
Data = read(vidObjs, (((11 * 60) + 30) * 25));
Vect = uint8(Data(round(poss(2)):round(poss(2)) + round(poss(4)), ...
    ups:bottoms, 2));
Begi(:, :) = (double(Vect .* uint8(Mask)));
for i = (((11 * 60) + 30) * 25) + 1 :1: (((11* 60) + 30) * 25) + 4
    Data = read(vidObjs, i);
    Vect = uint8(Data(round(poss(2)):round(poss(2))+round(poss(4)), ...
        ups:bottoms, 2));
```

```
    Begi(:, :) = (double(Vect .* uint8(Mask))) + Begi(:, :);
end
Begi = Begi ./ 5;
interface = 0.372 * (bottoms - ups);
%% B and I0 of the Beer-Lamnbert law are evaluated. the region above and
%% below the interface are taken separatly since after separation, the
%% concentration is zero above and maximum below the interface
for i=1 :1 : floor(interface)
    for j=1 :1 :size(Begi,1)
      Const(j, i) = (log10(Begi(j, i) / If(j, i))) / (1 - 0.372);
      I0(j, i) = If(j, i);
    end
end
for i =floor(interface) + 1 :1: size(Begi, 2)
    for j=1 :1: size(Begi,1)
      Const(j, i) = -log10(Begi(j, i) / If(j, i)) / 0.372;
      I0(j, i) = 10^(log10(Begi(j, i)) - (Const(j, i) * (1 - 0.372)));
    end
end
%% evaluation of the settling. The mask is applied on each frame of the
%% movie. To avoid dealing with a really large final
%% picture, 5 succesive frames are taken together and their light intensity
%% is averaged. for 5 succesive frames, the averaged frame is taken for the
%% next step where the Beer-Lambert is then applied based on the value of B
%% and I0 obtained in the previous step. The corresponding hold-up is
%% averaged on each pixel line along the height of the cell.

finexp = ((13 * 60)) * 25;
beginexp = ((11 * 60) + 30) * 25;
step = 5;
j = 1;
for i = beginexp :5: finexp-5
% average of 5 succesive frames
```

```
    Data = read(vidObjs,i);
        Iinter(:,:) =  double((uint8(Data(round(poss(2)):round(poss(2)) +
...
            round(poss(4)), ups:bottoms, 2))) .* uint8(Mask));
        for n=1:1:4
            Data = read(vidObjs,i+n);
            Vect(:, :) = uint8(Data(round(poss(2)):round(poss(2)) + ...
                round(poss(4)), ups:bottoms, 2));
            Iinter(:, :) = (double(Vect(:, :) .* uint8(Mask))) + ...
                Iinter(:, :);
        end
        Iinter = Iinter ./ 5;
% application of the Beer-Lambert law
        Conciter = 1-(log10(Iinter ./ I0) ./ Const);
% compiling of all the processing frames to get the complete picture of the
% experiment
        Conc(:, j:j, 1) = mean(Conciter, 1, 'omitnan');
        Iinter(Iinter==0) = NaN;
        FinalM(:, j:j,1 )= mean(Iinter, 1, 'omitnan');
        j = j + 1
end
save('Conc.mat','Conc');
save('FinalM.mat','FinalM');
%%
FinalM = Conc;
%% manual definition of the settling and coalescence curves
imshow(uint8(Picture))
%coalescence curve
[Xcoa Ycoa] = ginput (15);
%settling curve
[Xset Yset] = ginput (15);
close();
%%
coa(:, 1) = Xcoa(:) * step / 25;
```

```
coa(:, 2) = 0.185 - (Ycoa(:) * 0.185 / size(Picture, 1));
set(:, 1) = Xset(:) * step / 25;
set(:, 2) = 0.185 - (Yset(:) * 0.185 / size(Picture, 1));
save('coa.txt', 'coa', '-ascii', '-double', '-tabs')
save('set.txt', 'set', '-ascii', '-double', '-tabs')
%% definition of the limit of the close-packed zone (75%). the matrix cpz
%% has 3 columns, one for the time, one for the height and one for the
%% corresponding limiting hold-up. this corresponds to the first loop. The
%% second loop is for the definition of the sedimentation zone (20%)
m = 0;
for i = 100 :40: size(FinalM,2)
    m = m + 1;
    for j=round(size(FinalM,1)) :-1: 1
        if(FinalM(j, i) > 0.75)
            cpz(m, 1) = FinalM(1, i);
            cpz(m, 2) = FinalM(j, 1);
            cpz(m, 3) = FinalM(j, i);
            break
        end
    end
end
m=0;
for i=60 :60: size(FinalM, 2)
    m = m + 1;
    for j = round(0.8 * size(FinalM, 1)) :-1: 1
        if(FinalM(j, i )< 0.2)
            HP(m, 1) = FinalM(1, i);
            HP(m, 2) = FinalM(j, 1);
            HP(m, 3) = FinalM(j, i);
            break
        end
    end
end
```

```
save('cpz.txt', 'cpz', '-ascii', '-double', '-tabs')
save('HP.txt', 'HP', '-ascii', '-double', '-tabs')
```

11.10 Iso-optical Experiments: Experimental Data

The data specific to the settling experiments carried out with the iso-optical system are included in this appendix, i.e. the data on the physico-chemical properties, the drop-size distribution measurements and the graphs showing the evolution of the hold-up with time.

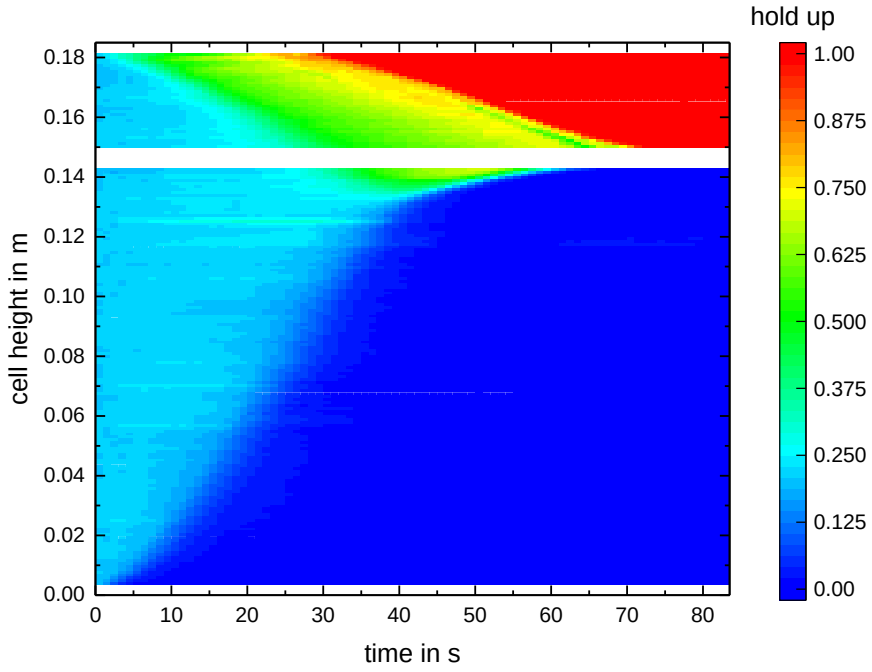

Fig. 11-19: Settling of the iso-optical system for an initial holdup of organic phase of 20.52% at mixing with 800 min^{-1}.

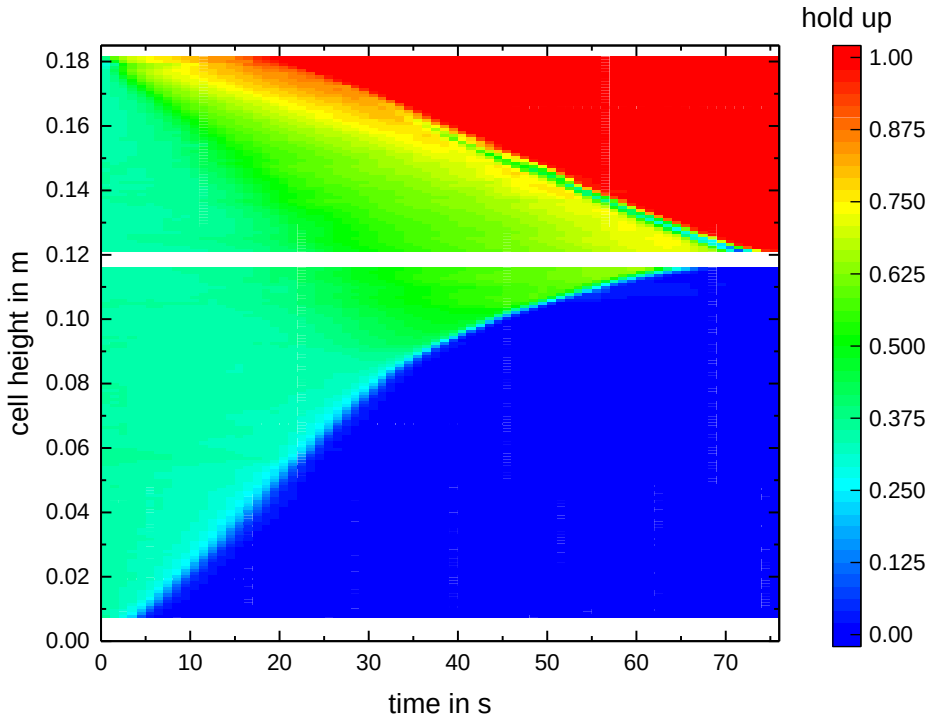

Fig. 11-20: Settling of the iso-optical system for an initial holdup of organic phase of 34.67% at mixing with 650 min^{-1}.

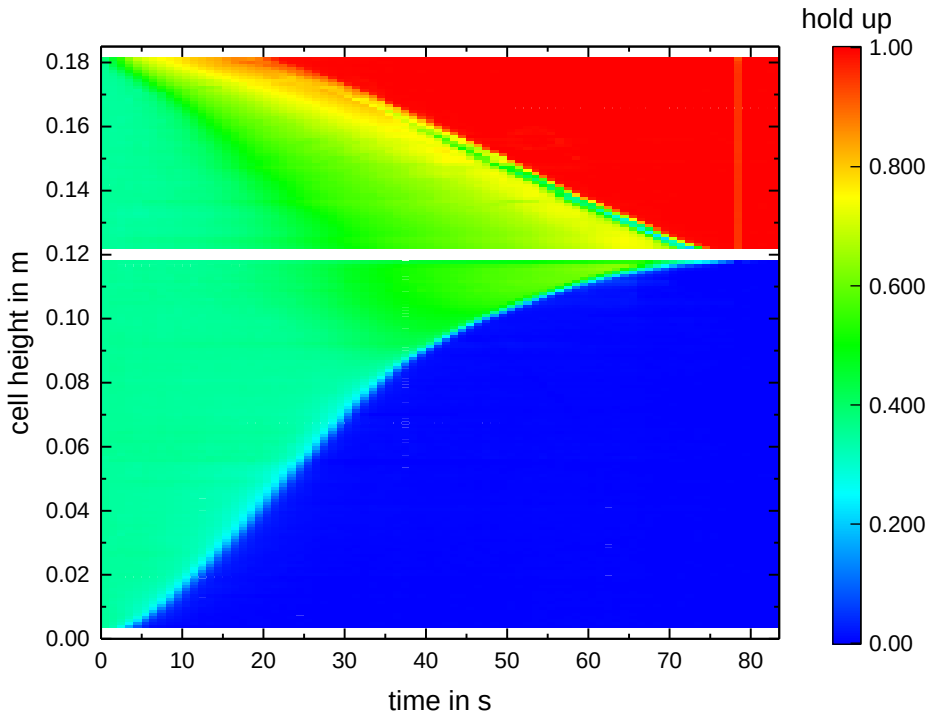

Fig. 11-21: Settling of the iso-optical system for an initial holdup of organic phase of 34.67% at mixing with 800 min^{-1}.

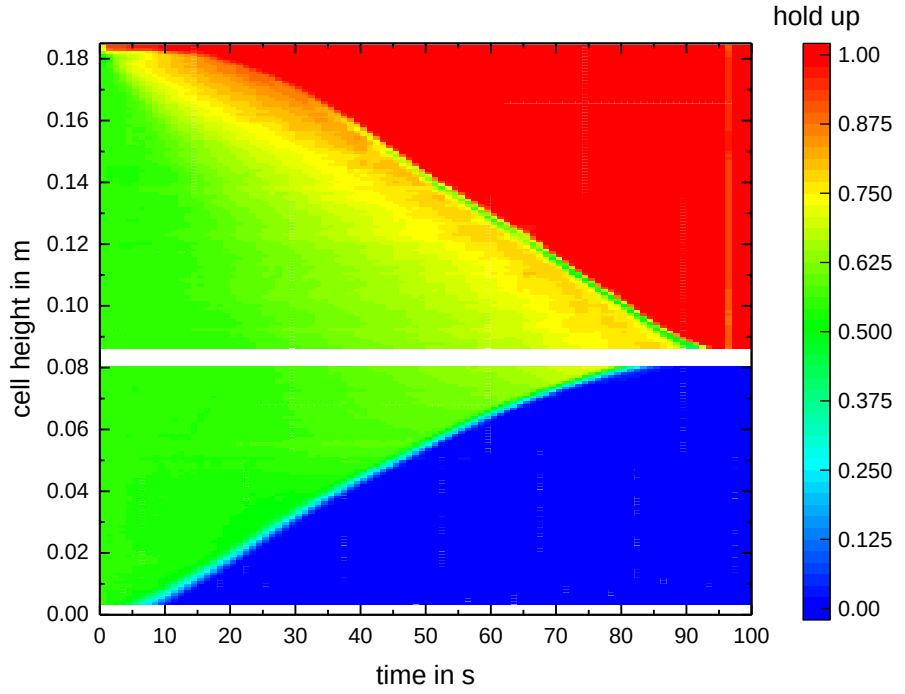

Fig. 11-22: Settling of the iso-optical system for an initial holdup of organic phase of 53.02% at mixing with 650 min^{-1}.

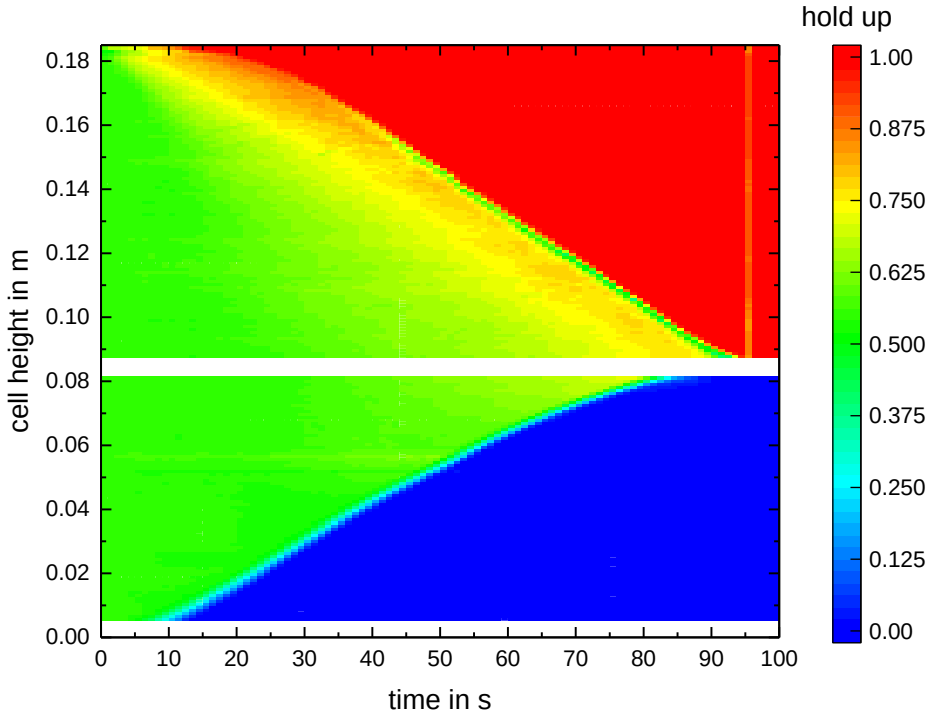

Fig. 11-23: Settling of the iso-optical system for an initial holdup of organic phase of 53.02% at mixing with 800 min^{-1}.

phase fraction	mixing speed in min^{-1}	settling time in s
20.52%	650	68
	800	72
34.67%	650	73
	800	71
53.02%	650	98
	800	98

Tab. 11-3: settling time measured for the different iso-optical settling experiments

phase ratio (O/A)	phase	density in kg/m^3	viscosity in mPas	interfacial tension in mNm
20.52%	organic phase	662.10	1054.97	22.2
	aqueous phase	0.371	3.036	
34.67%	organic phase	659.91	1055.44	21.8
	aqueous phase	0.329	3.064	
53.02%	organic phase	659.90	0.336	22.0
	aqueous phase	1055.19	3.292	

Tab. 11-4: physico-chemical properties measured for the different iso-optical settling experiments

phase ratio (O/A)	mixing speed	number average diameter in µm	variance in µm
20.52%	650 min^{-1}	351	89
	800 min^{-1}	287	64
34.67%	650 min^{-1}	391	109
	800 min^{-1}	302	85
53.02%	650 min^{-1}	328	145
	800 min^{-1}	265	112

Tab. 11-5: Drop-size parameters measured for different mixing speeds for the different iso-optical settling experiment

In the Fig. 11-24 to Fig. 11-29, measured drop-size distributions are shown as histograms. The blue curves represent the lognormal distributions evaluated on the basis of the mean and the variance, which fit the experimental data well.

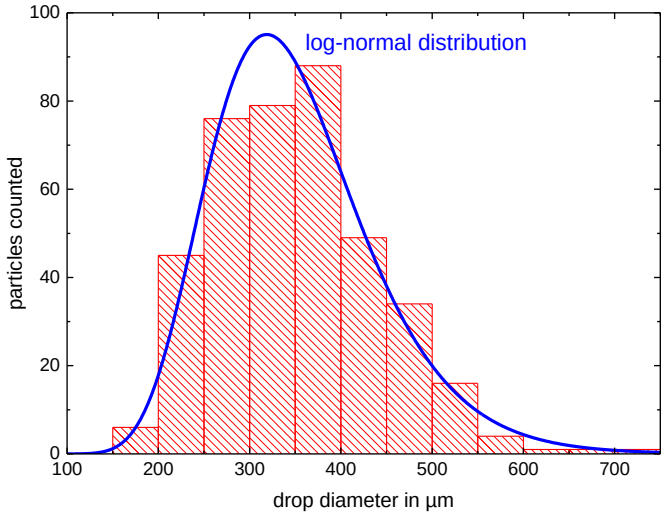

Fig. 11-24: Drop-size distribution measured for the iso-optical system for a phase ratio (O/A) of 20.52%. Mixing speed to produce the dispersion set to 650 min^{-1}. Blue curve represents the corresponding log-normal distribution from the measured mean and variance.

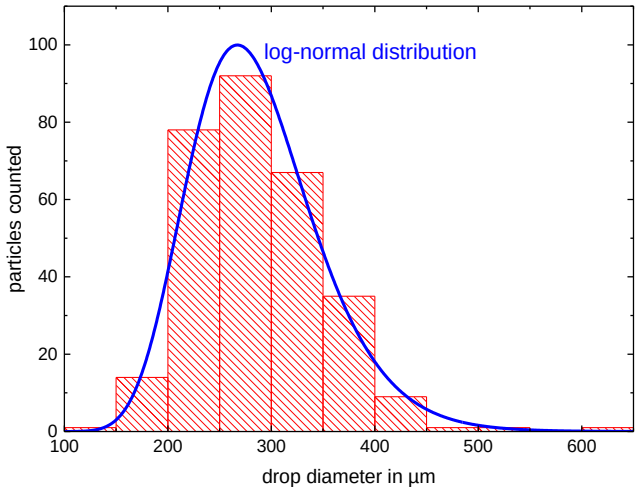

Fig. 11-25: Drop-size distribution measured for the iso-optical system for a phase ratio (O/A) of 20.52%. Mixing speed to produce the dispersion set to 800 min^{-1}. Blue curve represents the corresponding log-normal distribution from the measured mean and variance.

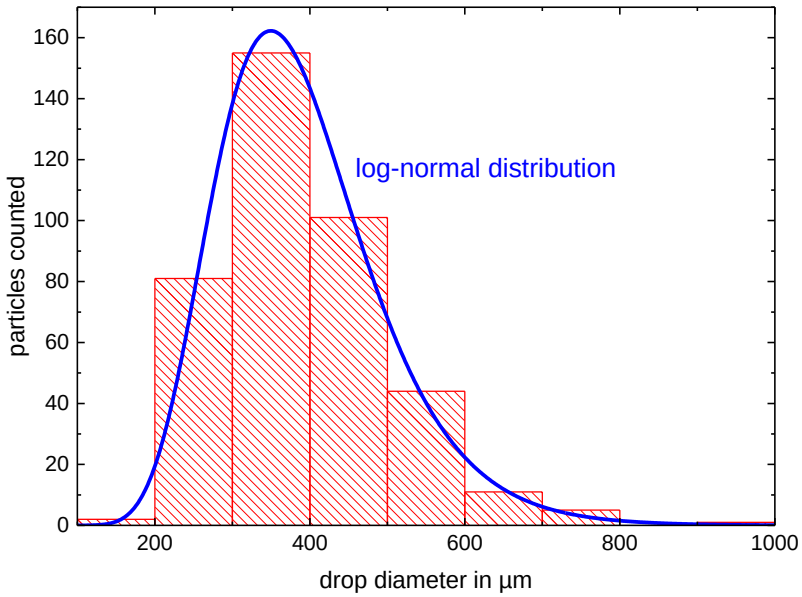

Fig. 11-26: Drop-size distribution measured for the iso-optical system for a phase ratio (O/A) of 34.67%. Mixing speed to produce the dispersion set to 650 min^{-1}. Blue curve represents the corresponding log-normal distribution from the measured mean and variance.

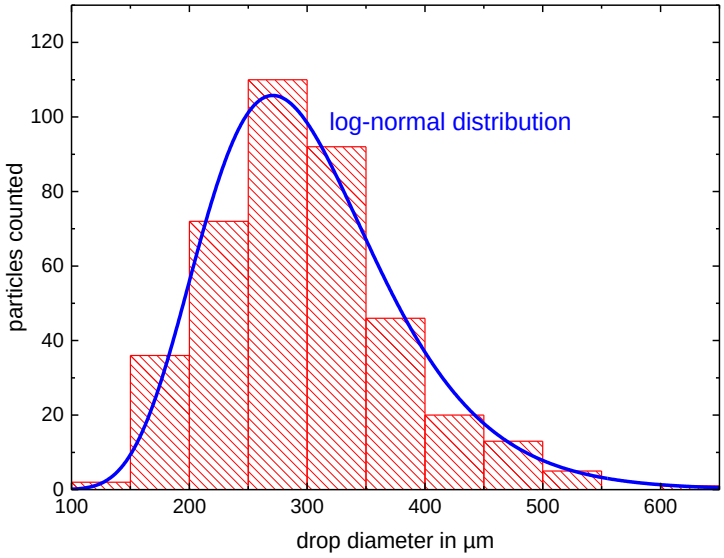

Fig. 11-27: Drop-size distribution measured for the iso-optical system for a phase ratio (O/A) of 34.67%. Mixing speed to produce the dispersion set to 800 min^{-1}. Blue curve represents the corresponding log-normal distribution from the measured mean and variance.

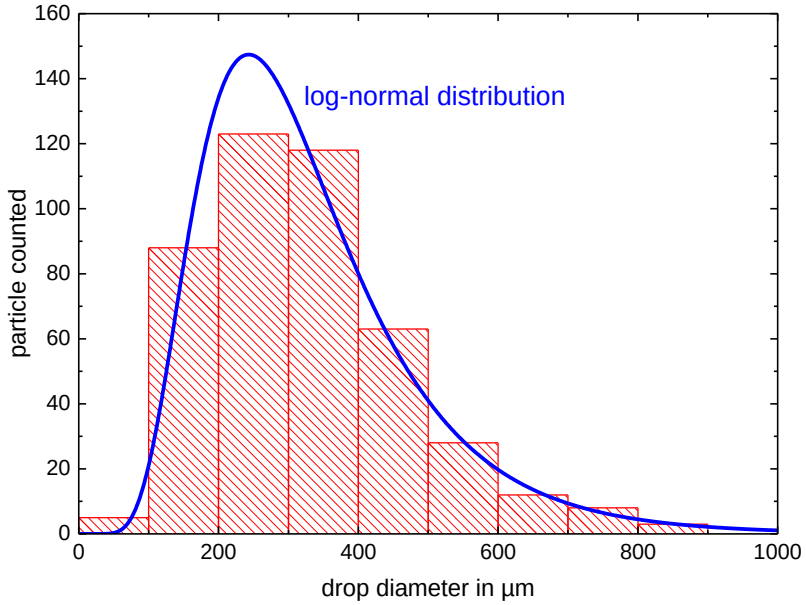

Fig. 11-28: Drop-size distribution measured for the iso-optical system for a phase ratio (O/A) of 53.02%. Mixing speed to produce the dispersion set to 650 min^{-1}. Blue curve represents the corresponding log-normal distribution from the measured mean and variance.

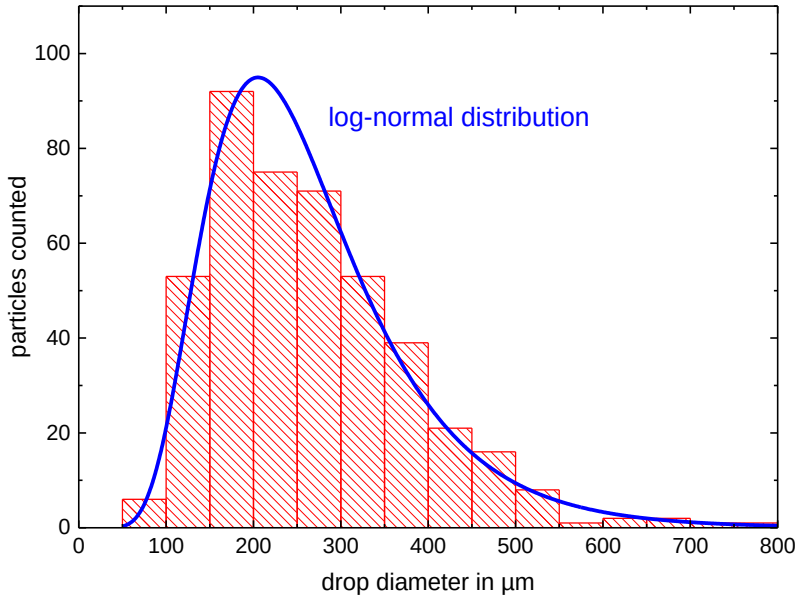

Fig. 11-29: Drop-size distribution measured for the iso-optical system for a phase ratio (O/A) of 53.02%. Mixing speed to produce the dispersion set to 800 min^{-1}. Blue curve represents the corresponding log-normal distribution from the measured mean and variance.

11.11 Iso-optical Settling Experiments Simulated with ReDrop

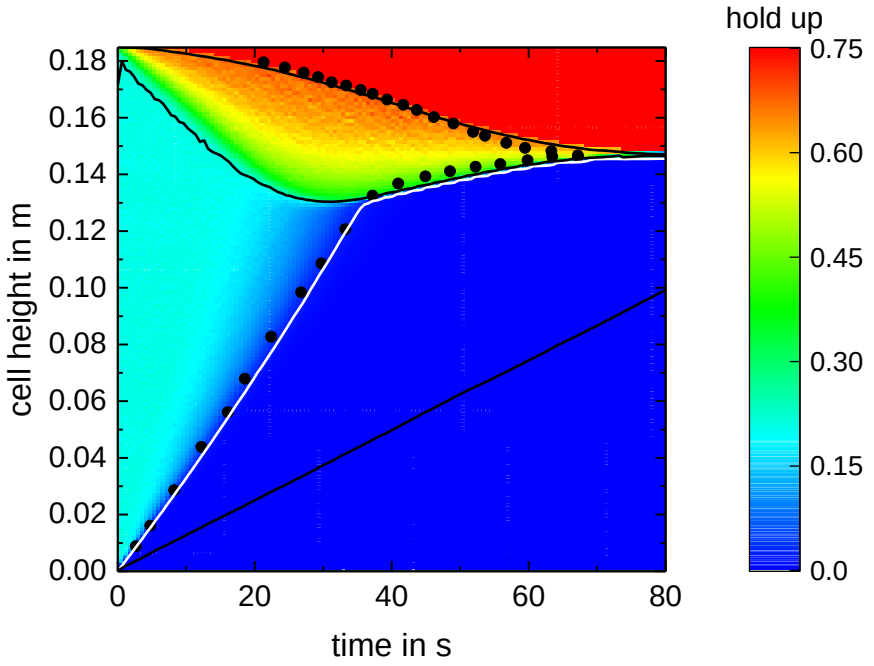

Fig. 11-30: ReDrop simulation of the settling of the iso-optical system for a phase fraction of 20.52% at mixing with 650 min^{-1}.

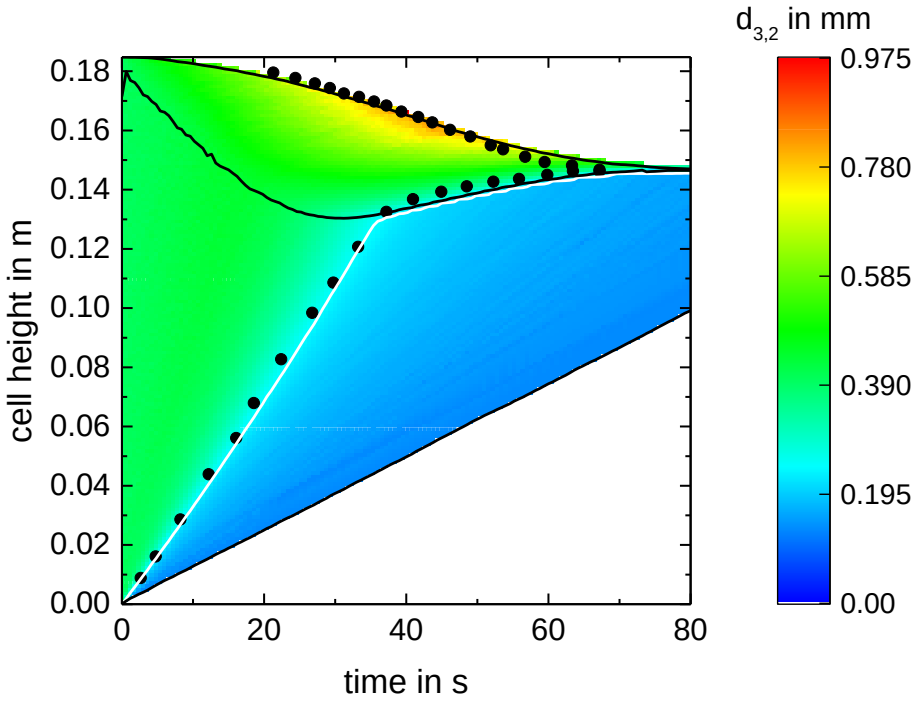

Fig. 11-31: Evolution of the drop size simulated for the settling of the iso-optical system for a phase fraction of 20.52% at mixing with 650 min^{-1}.

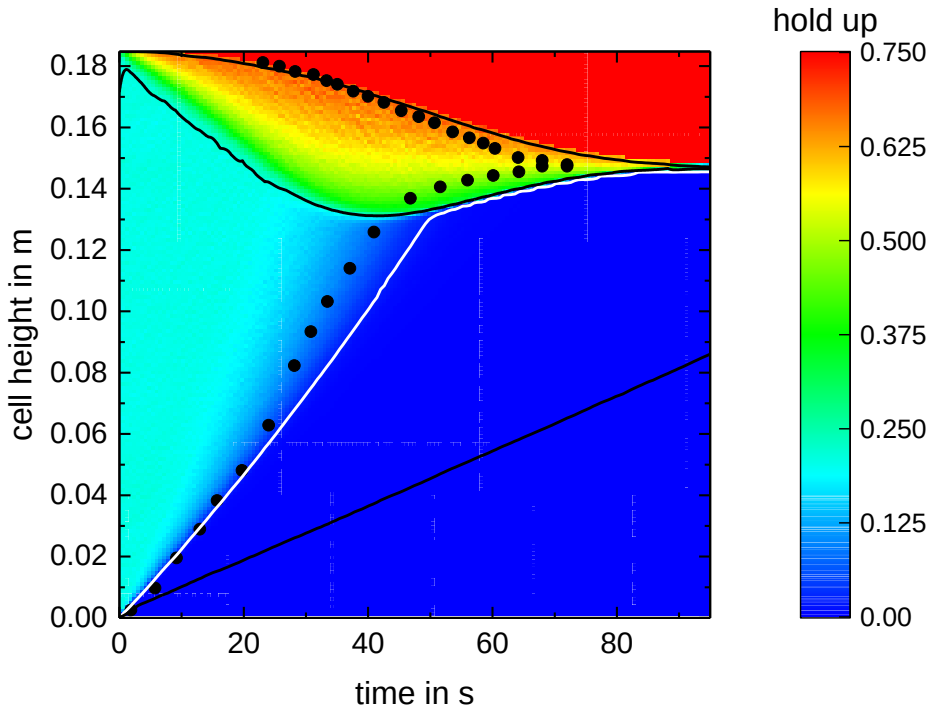

Fig. 11-32: ReDrop simulation of the settling of the iso-optical system for a phase fraction of 20,52% at mixing with 800 min^{-1}.

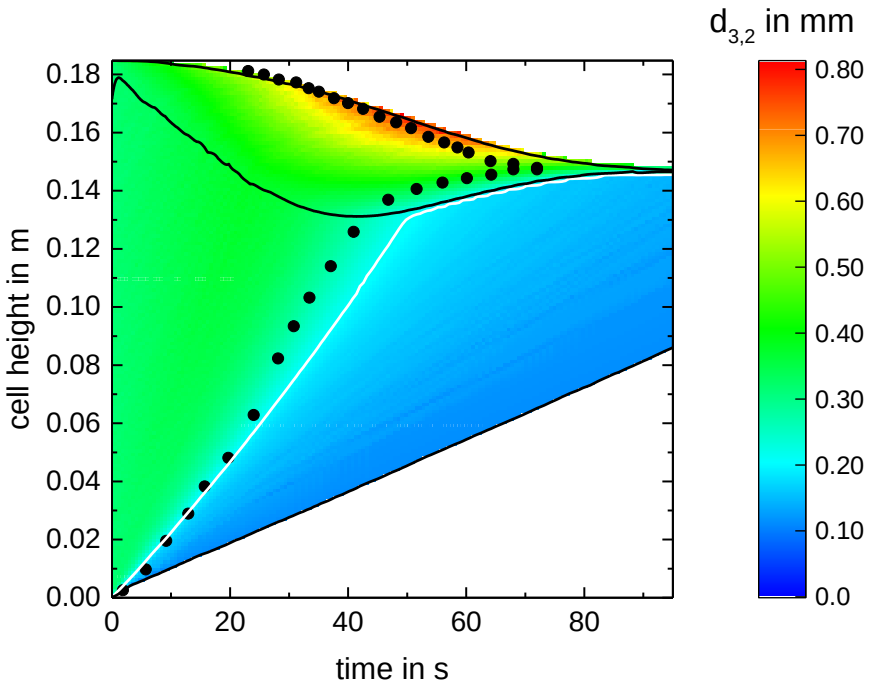

Fig. 11-33: Evolution of the drop size simulated for the settling of the iso-optical system for a phase fraction of 20,52% at mixing with 800 min^{-1}.

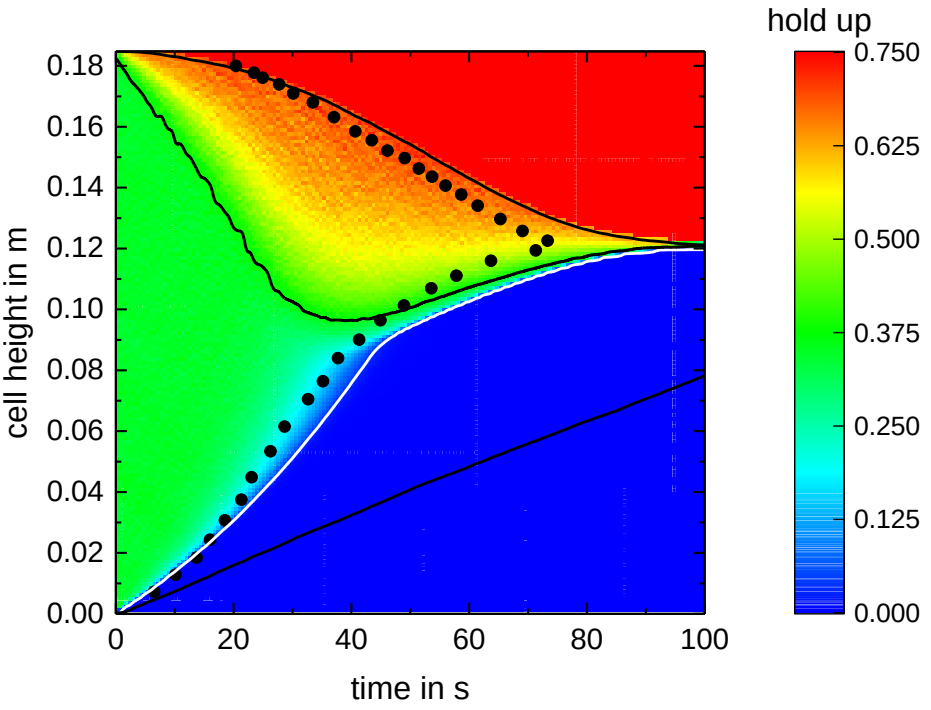

Fig. 11-34: ReDrop simulation of the settling of the iso-optical system for a phase fraction of 34.67% at mixing with 800 min^{-1}.

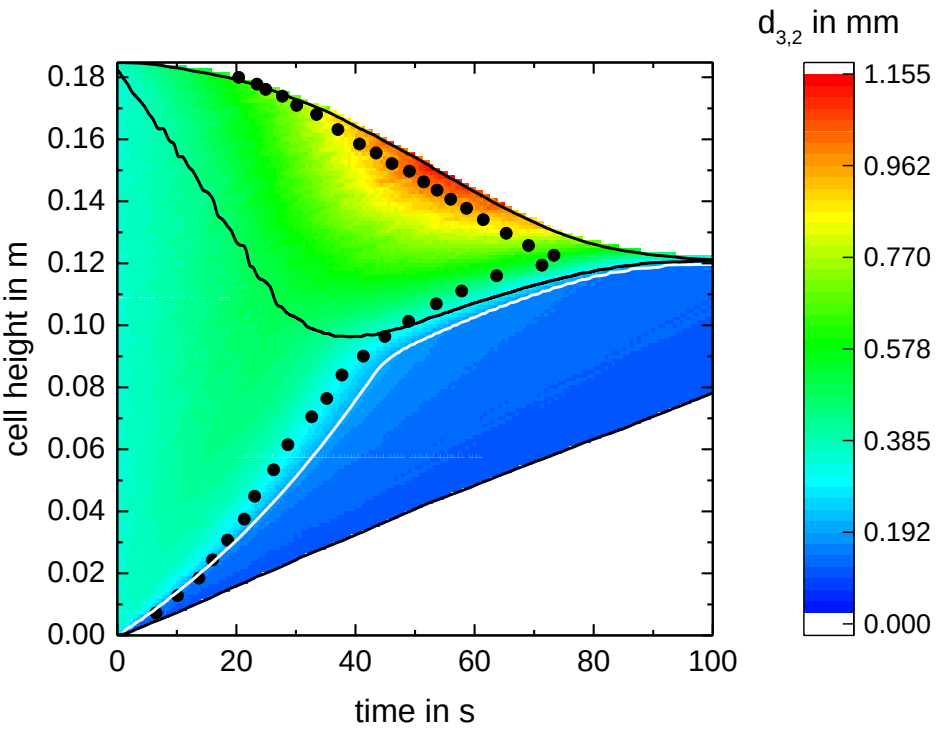

Fig. 11-35: Evolution of the drop size simulated for the settling of the iso-optical system for a phase fraction of 34.67% at mixing with 800 min^{-1}.

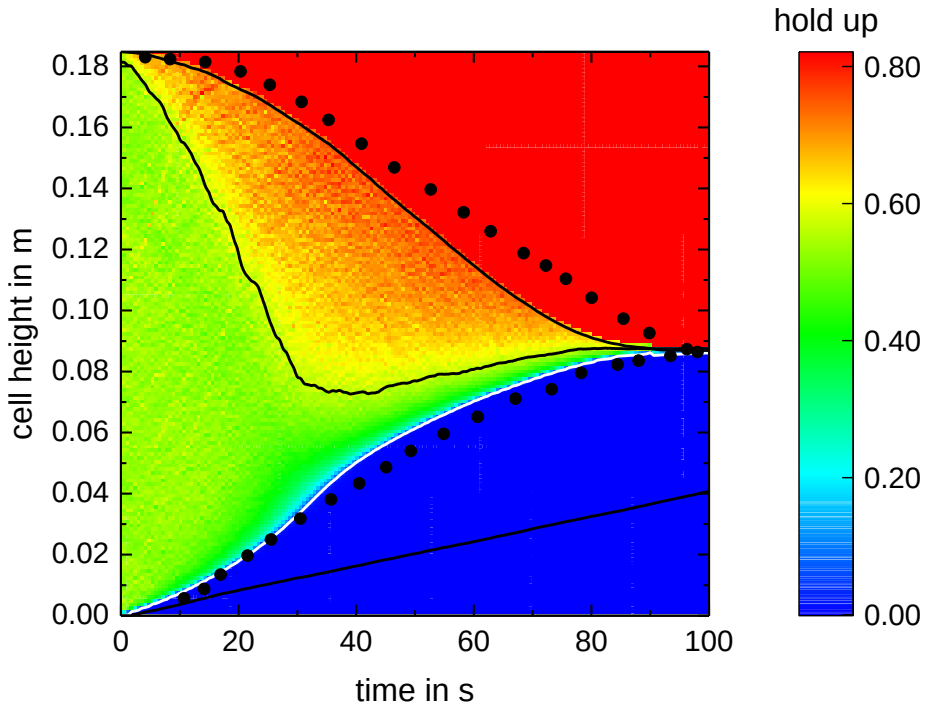

Fig. 11-36: ReDrop simulation of the settling of the iso-optical system for a phase fraction of 53.02% at mixing with 650 min^{-1}.

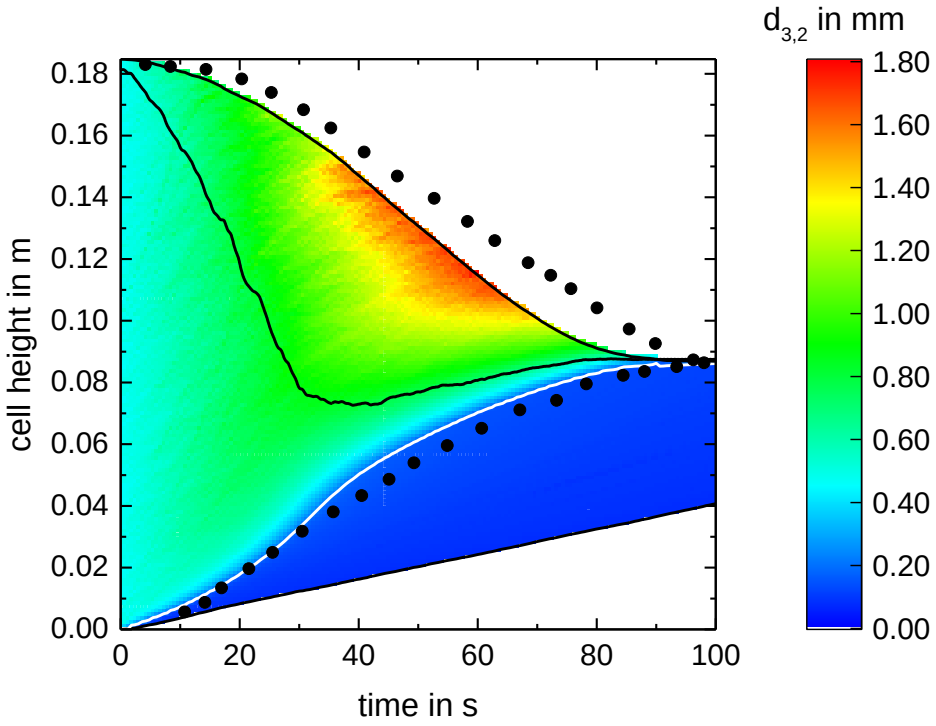

Fig. 11-37: Evolution of the drop size simulated for the settling of the iso-optical system for a phase fraction of 53.02% at mixing with 650 min^{-1}.

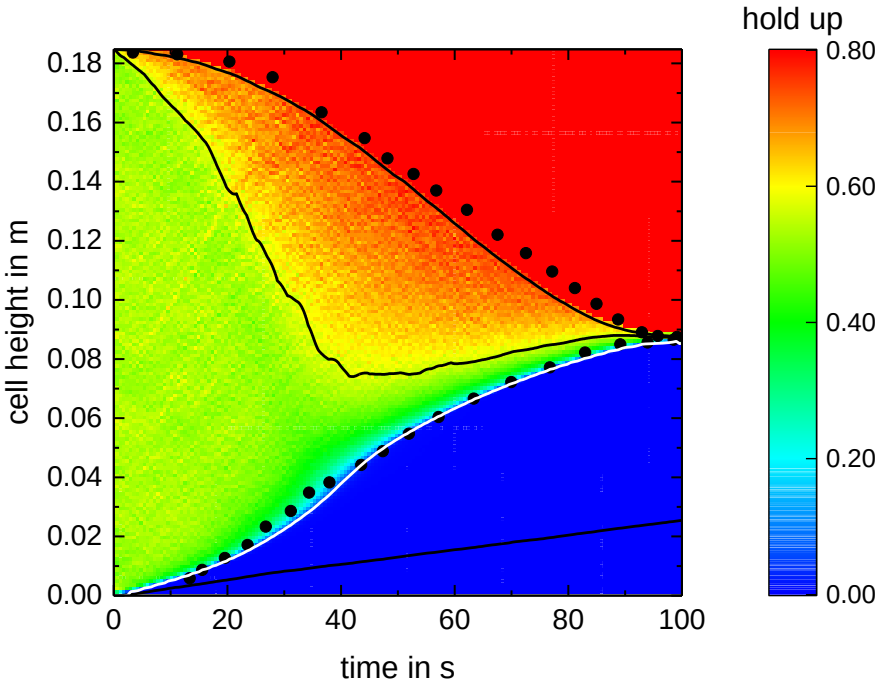

Fig. 11-38: ReDrop simulation of the settling of the iso-optical system for a phase fraction of 53.02% at mixing with 800 min^{-1}.

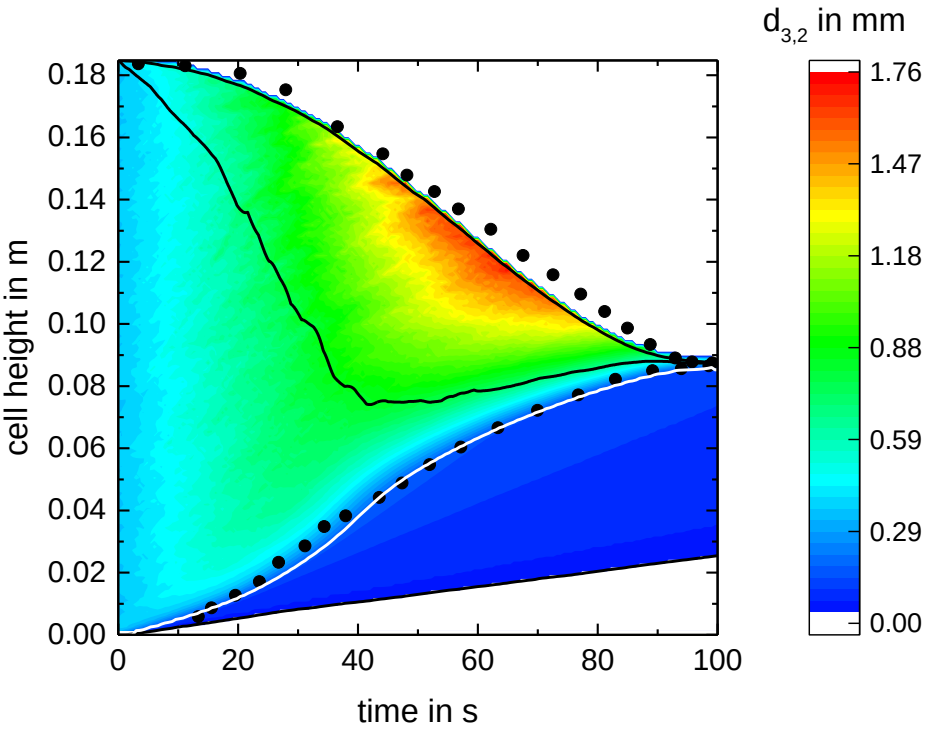

Fig. 11-39: Evolution of the drop size simulated for the settling of the iso-optical system for a phase fraction of 53.02% at mixing with 800 min^{-1}.

11.12 Effect of Ions Present in the Dispersion: Experimental Data

The experimental data specific to the experiments carried out to study the effect of the presence of salt in the two-phase system are included in this appendix, i.e. the data on the settling experiments and the data on the evolution of the partition coefficient of the dye with salt concentration.

NaCl		NH_4Cl		$NaNO_3$		$MgSO_4$	
Conc in mmol L^{-1}	K_{dye}	Conc in mmol L^{-1}	K_{dye}	Conc in mmol L^{-1}	K_{dye}	Conc in mmol L^{-1}	K_{dye}
0.001	1.42063	0.12726	2.15363	0.11648	1.56134	0.10154	1.57062
0.001	1.49194	1.01099	2.74121	0.9641	1.1835	1.02889	1.39945
0.08996	1.45600	9.59098	5.0894	0.9641	1.21491	9.4868	1.01606
0.48017	1.58974	19.14735	5.7259	0.9641	1.20816	9.4868	1.01558
1.24538	1.98058	19.14735	5.69085	7.96711	0.92612	19.09191	1.14435
1.24538	1.90385	48.27243	2.47774	19.17594	0.94731	47.22554	1.66950
2.59202	2.11224			19.17594	0.9286	47.22554	1.67424
5.37968	2.79268			47.99396	0.94342		
11.21363	3.43056						
11.21363	3.27397						
23.26262	3.63636						
48.21945	3.93651						
100.25694	4.34483						

Tab. 11-6: Data on the partition coefficient of the dye with the salt concentration for the different salts.

phase fraction	added salt	$d_{3,2}$ in µm	$d_{average}$ in µm	σ in µm	$t_{settling}$ in s
1/2	NaCl	139.95	127.04	28.55	75
	NH4Cl	144.91	127.63	33.86	52
	MgSO4	117.47	108.14	22.72	100
	NaNO3	158.60	139.91	36.80	70
2/1	NaCl	215.38	167.01	65.02	46
	NH4Cl	218.86	168.46	66.56	27
	MgSO4	188.28	141.17	59.48	37
	NaNO3	--	30	--	46800

Tab. 11-7: Data on the settling experiments performed with the different salts

11.13 Symbols

symbol	unit	description
a	m	edge length of a regular dodecahedron
A	m^2	area
B	-	Beer-Lamber law constant
C	-	parameter for drop deformation or for drop collision
d	m	diameter
E	J	energy
f	s^{-1}	frequency
F	N	force
F	c/mol	Faraday constant
g	m s^{-2}	gravitational acceleration
h	m	height
I	-	light intensity
K	-	real number of edges of a modified dodecahedron
K	-	partition coefficient
K'	-	parameter that considers characteristic parameter of the pores
L	m	perimeter of the dimple
N	-	number of particles
p	-	probability
P	Pa	pressure
R	m	radius
R	J mol^{-1} K^{-1}	gas constant
r_s^*	-	coalescence parameter
T	K	temperature
t	s	time
v	m s^{-1}	velocity
V	m^3	volume
x	m	distance
z	c	charge

Greek symbols

α	rad	angle
α	-	volumetric phase ratio
γ	-	factor taking into account the free volume reduction of the drops
Δ	-	step
ε	-	local hold-up
μ	Pa s	dynamic viscosity of the continuous phase
ξ	m^{-1}	Boublik Mansoori parameter
ρ	kg m^{-3}	density
σ	N m	surface tension
γ	V	electrical potential
ψ	m^2s^{-3}	energy dissipation
ϕ	-	Gold number

Subscripts

a	related to curvature of the dimple
BMCSL	related to Boublik Mansoori- Carnahan- Starling-Leland
c	related to the continuous phase
d	related to the drag coefficient
dd	dispersion-disintegration
F	contact area of the dimple
i	drop number i
j	drop number j
K	kinetic
v	related to asymmetry of the dimple
r	related to the relative velocity
s	related to the swarm velocity
0	blank measurement

Abbreviations

repr	representative
coll	collision
eq	equivalent
cpz	close-packed zone
hstat	hydrostatic
hydro	hydrodynamic
dode	dodecahedron
in	inscribed
penta	pentagon
cross-pore	cross-sectional area of a pore
disp	dispersion

12 References

[1] Kopriwa, N., Buchbender, F., Ayesterán, J., Kalem, M., Pfennig, A.: A Critical Review of the Application of Drop-Population Balances for the Design of Solvent Extraction Columns – I. Concept of Solving Drop-Population Balances and Modeling Breakage and Coalescence Solvent Extr. Ion Exch. 30 (7) (2012) 683-723.

[2] Kopriwa, N., Pfennig, A.: Characterization of Coalescence in Extraction Equipment Based on Lab-Scale Experiments. Solvent Extr. Ion Exch. 34 (7) (2016) 622-642.

[3] Ayesteràn, J., Kopriwa, N., Buchbender, F., Kalem, M., Pfennig, A.: ReDrop – A Simulation Tool for the Design of Extraction Columns Based on Single-Drop Experiments. Chem Ing. Tech. 38 (2015) 1894-1900.

[4] Richardson, J. F., Harker, J. H., Backhurst, J.R.: Particle Technology and Separation Processes, 5th ed., Coulson and Richardson's Chemical Engineering, Vol. 2, Butterworth Heinemann, Oxford, 2002.

[5] Henschke, M., 1995: Dimensionierung liegender Flüssig-flüssig-Abscheider anhand diskontinuierlicher Absetzversuche, Dissertation, RWTH Aachen University

[6] Corwin, E., Clusel, M., Siemens, A., Brujic, J. : A 'granocentric' model for random packing of jammed emulsions. Nature 460 (2009) 611-615.

[7] Liao, Y., Lucas, D.: A literature review on mechanisms and models for the coalescence process of fluid particles. Chem. Eng. Sci. 65 (10) (2010) 2851-2864.

[8] Kamp, J., Kraume, M.: From single drop coalescence to droplet swarms – Scale-up considering the influence of collision velocity and drop size on coalescence probability. Chem. Eng. Sci. 156 (2016) 162-177

[9] Chesters, A.K.: The modelling of coalescence processes in fluid-liquid dispersions : a review of current understanding. Chem. Eng. Res. Des. 69 (A4) (1991) 259-270.

[10] Sovová, H.: Breakage and coalescence of drops in a batch stirred vessel—II comparison of model and experiments. Chem. Eng. Sci. 36 (9) (1981) 1567-1573.

[11] Howarth, W.J.: Coalescence of drops in a turbulent flow field. Chem. Eng. Sci. 19 (1) (1964) 33-38.

[12] Lehr, F., Mewes, D.: A transport equation fort he interfacial area density applied to bubble column. Chem. Eng. Sci. 56 (3) (2001) 1159-1166.

[13] Prince, M.J., Blanch, H.W.: Bubble coalescence and break-up in air-sparged bubble columns. AIChE J. 36 (10) (1990) 1485-1499.

[14] Coulaloglou, C.A., Tavlarides, L.L.: Description of interaction processes in agitated liquid-liquid dispersions. Chem. Eng. Sci. 32 (11) (1977) 1289-1297.

[15] Henschke, M., Schlieper, L.H., Pfennig, A.: Determination of a coalescence parameter from batch-settling experiments. Chem. Eng. J. 85 (2-3) (2002) 369-378.

[16] Henschke, M., 2003: Auslegung pulsierter Siebboden-Extraktionskolonnen, Habilitation, RWTH Aachen University.

[17] Carnahan, N.F., Starling, K.E.: Equation of State for Nonattracting Rigid Spheres. J. Chem. Phys. 1969, 51 (2) (1969) 635-636.

[18] Hartland, S., Vohra, D.K.: Koaleszenz in vertikalen dichtgepackten Dispersionen. Chem. Ing. Tech. 50 (9) (1978) 673-682.

[19] Speth, H, 2004: Ein neues Modell zur Auslegung von Faserbett-Koaleszenzabscheidern, Dissertation, RWTH Aachen University

[20] Sajjadi, S., Zerfa, N., Brooks, B.W.: Dynamic behaviour of drops in oil/water/oil dispersions. Chem. Eng. Sci. 57 (2001) 663-675.

[21] Boublík, T.: Hard-Sphere Equation of State. J. Chem. Phys. 53 (1970) 471-472.

[22] Mansoori, G.A., Carnahan, N.H., Starling, K.E., Leland, T.W.Jr.: Equilibrium Thermodynamic Properties of the Mixture of Hard Spheres. J. Chem. Phys. 54 (4) (1971) 1523-1525.

[23] Buchbender, F., 2003: Single-Drop-Based Modelling of Drop Residence Times in Kuhni Columns, Dissertation, RWTH Aachen University

[24] Cockbain, E., McRoberts, T.: The stability of elementary emulsion drops and emulsions. J. Colloid Sci. 8 (4) (1953) 440-451.

[25] Gillespie, T., Rideal, E.K.: The coalescence of drops at an oil-water interface. Trans. Faraday Soc. 52 (1956) 173-183.

[26] Yu G.Z., Mao, Z.S.: Sedimentation and Coalescence Profiles in Liquid-Liquid Batch Settling Experiments. Chem. Eng. Technol. 27 (4) (2004) 407-413.

[27] Kopriwa, N., 2013: Quantitative Beschreibung von Koaleszenzvorgängen in Extraktionskolonnen, Dissertation, RWTH Aachen University

[28] Chan, D.Y.C., Klaseboer, E., Manica, R.: Film drainage and coalescence between deformable drops and bubbles. Soft Matter. 7 (2011) 2235-2264.

[29] Willvock, J., Gebauer, F., Kamp, J., Bart, H.-J., Kraume, M.: Systematic Analysis of single Droplet Coalescence. Chem. Eng. Technol. 37 (7) (2014) 1-10.

[30] Wassen, S., 2009: Experimentelle Untersuchung des Koaleszenzverhaltens von Flüssig-Flüssig-Dispersionen in einer Absetzmesszelle, dissertation, RWTH Aachen University

[31] Smith, D.V., Davies, G.A.: Coalescence in Droplet Dispersions. Can. J. Chem. Eng., 48 (1970) 628-637

[32] Buevich, Y.A., Lipkina, E.K.: Disruption of thin liquid films. Colloid. J. USSR (Engl. Trans.) 40 (2) (1978) 167-171.

[33] MacAvoy, R.M., Kintner, R.C.: approach oft wo identical rigid spheres in liquid filed. J. Colloid Sci. 20 (2) (1965) 188-190.

[34] Pfennig, A. Schwerin, A.: Influence of Electrolytes on Liquid−Liquid Extraction. Ind. Eng. Chem. Res. 37 (8) (1998) 3180-3188.

[35] Webber, G.B., Scott, A.E., Stevens, G.W., Greiser, F., Dagastine, R.R., Chan, D.Y.C. Measurements of dynamic forces between drops with the AFM: novel considerations in comparisons between experiment and theory. Soft matter 4 (2008) 1270-1278.

[36] Kamp, J., Kraume, M.: Coalescence efficiency model including electrostatic interactions in liquid/liquid dispersions. Chem. Eng. Sci. 126 (2015) 132-142.

[37] MacKay, G.D.M., Mason, S.G.: The gravity approach and coalescence of fluid drops at liquid interfaces Can. J. Chem. Eng. 41 (5) (1963) 203-212.

[38] Hartland, S.: The effect of circulation patterns on the drainage of the film between a liquid drop and a deformable liquid—liquid interface. Chem. Eng. Sci. 24 (3) (1969) 611–613.

[39] Kim, J.W., Lee, W.K.: coalescence behavior of two bubbles in stagnant liquids. J. Chem. Eng. Jpn. 20 (5) (1987) 448-453.

[40] Richardson, J.F., Zaki, W.N.: The sedimentation of a suspension of uniform spheres under conditions of viscous flow. Trans. Inst. Chem. Eng., 8 (1954) 65-73.

[41] Cheng, N.-S.: Comparison of formulas for drag coefficient and settling velocity of spherical particles. Powder Technol. 189 (2009) 395-398.

[42] Princen, H. M.: shape of a fluid drop at a liquid-liquid interface. J. Colloid Sci., 18 (1963) 178-195.

[43] Garthe, D., 2006: Fluiddynamics and Mass Transfer of Single Particles and Swarms of Particles in Extraction Columns, dissertation, Technische Universität München

[44] Pfennig, A., Schwerin, A.: Analysis of the Electrostatic Potential Difference in Aqueous Polymer Two-Phase Systems. fluid phase equilibr., 108 (1995) 305-315.

[45] Pfennig, A., Schwerin, A., Gaube, J.: Consistent view of electrolytes in aqueous two-phase systems. J. Chromatogr. B, 711 (1998) 45-52.

[46] Guggenheim, E.A.: The Conceptions of Electrical Potential Difference between Two Phases and the Individual Activities of Ions. J. Phys. Chem., 33 (1929) 842-849.

[47] Kamp, J., Villwock, J., Kraume, M.: Drop coalescence in technical liquid/liquid applications: a review on experimental techniques and modeling approaches. Rev. Chem. Eng.,33 (1) (2016) 1-47.

[48] Tobin, T., Ramkrishna, D.: Modeling the effect of drop charge on coalescence in turbulent liquid—liquid dispersions. Can J. Chem. Eng., 77 (1999) 1090-1104.

[49] Melis, S., Kemmere, M., Meuldijk, J., Storti, G., Morbidelli, M.: A model for the coagulation of polyvinyl acetate particles in emulsion. Chem. Eng. Sci., 55 (2000) 3101-3111.

[50] Marčelja, S.: Selective Coalescence of Bubbles in Simple Electrolytes. J. Phys. Chem. B, 110 (2006) 13062-13067

[51] Dagastine, R.R., Manica, R., Carnie, S.L., Chan, D.Y.C., Stevens, G.W., Grieser, F.: Dynamic Forces Between Two Deformable Oil Droplets in Water. Science, 313 (5784) (2006) 210-213.

[52] Del Nero, J.: Theoretical and experimental investigation of the second hyperpolarizabilities of methyl orange. J. Chem. Phys., 122 (2005) 104506.

[53] Rouyer, F., Pitois, O., Lorenceau, E., Louvet, N.: Permeability of a bubble assembly: From the very dry to the wet limit. Phys. Fluids, 22 (2010) 043302.

[54] Mirza, S., Richardson, J. F.: Sedimentation of suspension of particles of two or more sizes. Chem. Eng. Sci., 34 (1979) 447-454.

[55] Yiantsios, S. G., David, R. H.: On the buoyancy-driven motion of a drop towards a rigid surface or a deformable interface. J. Fluid Mech., 217 (1990) 547-573.

[56] Burrill, K.A., Woods, D.R.: Film shapes for deformable drops at liquid–liquid interfaces. III. Drop rest-times, J. Colloid Interf. Sci. 42 (1) (1973) 35–51.

[57] Hartland, S.:The coalescence of a liquid drop at a liquid–liquid interface. Part II: Film thickness, Trans. Instn. Chem. Engrs. 45 (1967) 102–108.

[58] Kalem, M., Altunok, M.Y., Pfennig, A.: Sedimentation Behavior of Droplets for the Reactive Extraction of Zinc with D2EHPA. AIChE J. 56(1) (2010) 160-167.

[59] Adekojo Waheed, M., Henschke, M., Pfennig, A.: Simulating sedimentation of liquid drops. Int. J. Numer. Meth. Engng 59 (2004) 1821-1837.

[60] Soika, M., Pfennig, A.: Extraktion – Eine Frage des Wassers? Chem. Ing. Tech. 77(7) (2005) 905-911.

[61] Noïk, C., Palermo, T., Dalmazzone, C.: Modeling of Liquid-Liquid phase separation: Application to petroleum Emulsions. J DISPER SCI TECHNOL. 34 (8) (2013), 1029-1042.

[62] Bol et al.: The kinetics of phase separation in liquid-liquid extraction: modeling of droplet swarm coalescence. Chem. Ing. Tech. 93(10) (2021), 1502-1508.

[63] Stokes, G. G.: On the effect of the internal friction of fluids on the motion of pendulums. Trans. Cam. Phil. Soc. 9 (1851), 8

[64] Goldstein, S.: The steady flow of viscous fluid past a fixed spherical obstacle at small Reynolds numbers. Proc. Roy. Soc. A. 123 (1929), 225

[65] Oseen, C. W.: Uber den G¨ultigkeitsbereich der Stokesschen Widerstandsformel. Ark. Mat. Astr. Fys. 9(16) (1913), 1-15

[66] Wadell, H.: The coefficient of resistance as a function of Reynolds' number for solids of various shapes. J. Franklin. Inst. 217 (1934), 459

[67] Khan, A. R., Richardson, J. F.: The resistance to motion of a solid sphere in a fluid. Chem. Eng. Comm. 62 (1987), 135.

[68] Khan, A. R., Richardson, J. F.: Fluid-particle interactions and f low characteristics of fluidized beds and settling suspensions of spherical particles. Chem. Eng. Comm. 78 (1989), 111.

[69] Richardson, J. F., Zaki, W. N.: Sedimentation and fluidisation: Part I. Trans. Inst. Chem. Eng. 32 (1954), 35

[70] Garside, J., Al-Dibouni, M. R.: Velocity–voidage relationships for fluidization and sedimentation in solid–liquid systems. Ind. Eng. Chem. Proc. Des. Dev. 16 (1977), 206

[71] Rowe, P. N.: A convenient empirical equation for estimation of the Richardson-Zaki exponent. Chem. Eng. Sci. 42 (1987), 2795.

[72] Clusel, M., Corwin, E., Siemens, A. O. N., Brujic, J.: A'granocentric' model for random packing of jammed emulsions. Nature. 460 (2009), 611-615.

[73] Wallis, G. B.: One-dimensional Two-phase Flow. McGraw-Hill, 1969.

[74] Pilhofer, T., Mewes., D.: Siebboden-Extraktionskolonnen. Vorausberechnung unpulsierter Kolonnen. Verlag Chemie. (1979), 136.

[75] Bart, H.-J.: Reactive Extraction. Springer, 2001.

[76] Pornprapa, B., 2014: Investigation of drop dispersions in batch settling processes, Dissertation, TU Graz

[77] Pornprapa, B., Rudelstorfer, G., Grafschafter, A., Siebenhofer, M.: The kinetics of droplet sedimentation in liquid-liquid extraction. Chem. Ing. Tech. 93 (2021), 260-272.

[78] Pornprapa, B., Rudelstorfer, G., Grafschafter, A., Siebenhofer, M.: The kinetics of phase separation in liquid-liquid extraction: Modeling of droplet swarm coalescence. Chem. Ing. Tech. 93 (2021), 1502-1508.

[79] Bernarz, A., Schmidt, M., Eggert, A., Bannwarth, S., Wessling, M., Jupke, A.: Erfassung des Koaleszenz- und Sedimentationsverhaltens von trüben Systemen in einer standardisierten Absetzzelle. Chem. Ing. Tech. 88-9 (2016), 1289.

[80] Jeelani, S. A. K., Hartland, S.: Prediction of steady state dispersion height from batch settling data. AIChE Journal 31(5) (1985), 711–720.

[81] Dimitrijević, D., Bösenhofer, M., & Harasek, M.: Liquid–Liquid Phase Separation of Two Non-Dissolving Liquids—A Mini Review. Processes 11(4) (2023), 1145

[82] Hossain, K. T., Sarkar, S., Mumford, C. J., & Phillips, C. R.: Hydrodynamics of mixer-settlers. Industrial & Engineering Chemistry Process Design and Development 22(4) (1983), 553–563.

[83] Reissinger, K.-H., Schröter, J., & Bäcker, W.: Possibilities and problems in the design of extractors. Chemie Ingenieur Technik 53 (8) (1981), 607–614

[84] Thaker, A. H., & Buwa, V.: Separation of Liquid-Liquid Dispersion in a Batch Settler: CFD-PBM Simulations Incorporating Interfacial Coalescence. AIChE Journal. 66 (11) (2020).

[85] Steinhoff, J., Charlafti, E., Leleu, D., Reinecke, L., Franken, H., Becker, K., Kalem, M., Sixt, M., Braß, M., Borchardt, D., Bäcker, W., Wegener, M., Maaß, S., Weber, M., Acher, T., Matten, C., Pfennig, A., Kraume, M., Hans-Jörf, B.: Energie- und Ressourceneinsparung durch Innovative und CFD-basierte Auslegung von Flüssig/Flüssig-Schwerkraftabscheidern. Chem. Ing. Tech. 93 (7) (2021), 1152-1165.

[86] Jeelani; S. A. K., Hosig, R., Windhab, E. J.: Kinetics of low Reynolds number creaming and coalescence in droplet dispersions. 51(1) (2005), 149–161.

[87] Allak, A., Jeffreys, G.V.: Studies of coalescence and phase separation in thick dispersion bands. AIChE J. 20 (1974), 564–570.

[88] Misra, A., Bonamy, C., M. De Souza, L., Hohl, L., Illner, M., Kraume, M., Repke, J.-U., Thévenin, D.: Simulating separation of a multiphase liquid-liquid system in a horizontal settler by CFD. Chem. Eng. Sci. 167 (10) (2017), 242-250.

[89] Hao, Z., Yang, L., Xiao, S., Liu, X., Zhao, W.: CFD-PBE Simulation of Flow Dynamics and Mass Transfer in Two-Stage Countercurrent Mixer-Settler. Ind. Eng. Chem. Res. 62 (26) (2023), 10237-10251.

[90] Shabani, M., Mazahery, A.: Computational Fluid Dynamics (CFD) Simulation of Liquid-Liquid Mixing in Mixer Settler. Archives of Metallurgy and Materials, 57(1) (2012), 173-178

[91] Eberz, J., Sibirtsev, S., Jupke, A.: Mini-batch settling cell for investigation of liquid-liquid phase separation. Chem. Eng. Sci. 301(5) (2025), 173-178

[92] Barnea, E., Mizrahi, J.: separation mechanism of liquid-liquid dispersions in a deep-layer gravity settler: part iv-continuous settler characteristics. trans. instn chem. engrs, Vol. 53 (1975), 83-92

[93] Ryon, A.D., Daley, F.L., Lowrie, R.S.: scale-up of mixer-settlers. Chemical engineering progress, 55 (10) (1959), 71-75